Hydrodynamic loading, performance and design of tidal stream turbine rotors



Huw Aidan Edwards

Worcester College

A thesis submitted for the degree of
Doctor of Philosophy

Supervised by
Professor R. H. J. Willden and Dr C. R. Vogel

Department of Engineering Science
University of Oxford

Hilary Term, 2026

Declaration

I declare that this thesis is entirely my own work and, except where stated, describes my own research.

Huw Aidan Edwards
Worcester College

Acknowledgements

Firstly, I would like to thank my supervisors, Prof. Richard Willden and Dr Christopher Vogel, for sharing their passion for turbines, and for guiding my development of the skills and diligence needed to research them. I would also like to express my gratitude for the opportunities they afforded me through their research projects, namely the Supergen ORE Unsteady Tidal Turbine Benchmarking Project and the CoTide Project, which greatly enriched my journey as a DPhil student.

I would also like to acknowledge the EPSRC for funding this work through the Wind and Marine Energy Systems Centre for Doctoral Training (EP/S023801/1). I'm grateful for the technical and professional training, and for the supportive community which the CDT provides, so thank you to all the staff and students.

It has been a pleasure to work alongside the talented members of the Tidal and Wind Energy Research group. Thank you to all the students and academics for sharing fascinating insights into your research, and for the technical feedback which has been integral to this work. In particular, I'd like to thank Dr Xiaosheng Chen for his advice on all things CFD, for passing down the group's rotor design experience, and for generously sharing reference data used in this thesis.

I'd also like to acknowledge the Oxford University Yacht Club and all the friends I made through our shared experiences on the water. To Rory, JJ and Annika, thank you for our many sporting adventures, and for your tips for navigating what lay ahead.

Finally, I'd like to thank all my family and friends from North Wales, Durham and beyond. Thank you to my parents, Henry and Merrion, for inspiring me to pursue this degree, and for your unconditional support and encouragement once the challenge became a reality. To Rowan and Elodie, whose unspoken backing and constant achievements continue to motivate me. To Neil and Anya, for Sunday roasts and rounds of golf when a mental distraction was most welcome. Last but not least, I must thank Siân, without whose seemingly endless patience and belief I may not have overcome the challenges of this degree. I will forever be grateful for everything you contributed to this team effort.

Abstract

For the tidal stream energy sector to develop towards commercial scale deployment, greater understanding of turbine performance and hydrodynamic loading is needed to reduce uncertainty in blade structural requirements and expected turbine energy yield. Increasing rotor diameter has great potential to reduce the levelised cost of energy, and operating turbines close to the water surface, where the flow speeds are highest and they can be accessed more easily for maintenance, is an attractive prospect. As a result, tidal stream turbine designs increasingly occupy a larger proportion of the water column, and are designed to operate closer to the free surface relative to their diameter.

Operating near a fluid boundary introduces anisotropy to the flow through and around the rotor, leading to time-varying blade loads which necessitate more robust structural design. As boundary proximity effects become more prominent, it is increasingly important to evaluate the magnitude of these load variations, and understand the underlying hydrodynamics, to quantify their contribution to peak loading and fatigue damage. This work investigates boundary proximity effects on performance and loading by numerically simulating a 1.6 m experimental turbine with varying tip clearance to the free surface using the actuator line method. The effects of free surface deformation are quantified through comparison of results generated using multi-phase numerical simulations to those which assume the free surface to behave as a rigid lid. The azimuthal distributions of the root bending moments were not significantly affected by the modelling approach, and exhibited maximum fluctuation ranges of 2.8% and 2.2% in the flapwise and edgewise directions, respectively, when the turbine was operated at the closest simulated tip spacing of 0.063 rotor diameters. Phase shifts in the location of root bending moment peaks relative to top dead centre are observed, and explained in relation to the driving flow mechanisms. Boundary constriction effects were observed to accelerate the axial component of flow velocity through the rotor plane adjacent to the boundary. Immediately upstream of the rotor, a tangential velocity distribution symmetric about a vertical axis on the domain's centreline was observed, arising from the lateral diversion of the radially expanding incoming flow by the free surface boundary. The combination of these flow mechanisms leads to a velocity field at the rotor plane which is asymmetric about the vertical axis which bisects it, which in turn leads to asymmetric azimuthal variations in blade loads. The flapwise root bending moment is found to be dominated by variations in the relative velocity magnitude, yielding peaks which occur ahead of blade top dead centre. The edgewise root bending moment showed much greater dependence on the angle of attack variation, and as a result, its peak generally lagged blade top dead centre. Minor variations in rotor performance with changes to tip clearance are identified in the rigid lid results, consistent with widely accepted understanding of flow constriction effects. Reducing tip clearance increased the power and thrust coefficients by 0.13%. However, the multi-phase simulation data could not be used to substantiate these trends as the performance signals were relatively less converged.

Multi-objective optimisation can be used to reduce the cost of energy produced by wind and tidal turbines, enabling design relative to competing objectives. However, few studies have utilised such techniques to design tidal stream turbine rotors, and optimisations have not captured discrete blade and blockage effects. Azimuthally-averaged modelling approaches do not inherently capture discrete blade effects such as tip vortices and three-dimensional blade flows more generally. Hence,

the spanwise distributions of force and flow components they predict can differ from those of a discrete-bladed rotor. This work studies the impacts of design strategies, modelling techniques and tip corrections on the predicted optimal hydrodynamic shape of tidal stream turbine blades. Firstly, an existing iterative design approach, developed for actuator disc simulations, is extended to actuator line modelling to examine the impact of discrete blade effects. The incompatibility of the disc-based design criteria, which focus on local loading and blade angle of attack, with discrete blade modelling, and the desire for greater flexibility in design objectives, motivated the development of a new approach utilising multi-objective gradient-descent optimisation to adjust the blade geometry relative to competing cost-proxy objectives. The method is developed to evaluate the objective function with actuator line simulations, accounting for blockage and discrete blade effects in the design process. However, in developing the design procedure, the blade element-momentum method is also utilised as a low-cost model to allow extensive exploration of the design space, but noting its inability to capture discrete blade or blockage effects. A Pareto set of equally optimal blade shapes are produced spanning a diverse performance range, an example of which reduces the thrust on a given existing rotor by 19% without significant loss in power. Implementing the algorithm with tip-corrected actuator line simulations successfully minimised the objective function, but initial trials led to blade shapes which are unlikely to be effective in reality. Hence, alternative tip treatments and geometry constraining methods are considered to improve the output design.

Table of contents

Abbreviations **xi**

Nomenclature **xii**

I Introduction **1**

1 Background and objectives **2**
1.1 Background ... 2
1.2 Thesis outline and objectives ... 5
1.2.1 Objective 1: Free surface proximity effects ... 5
1.2.2 Objective 2: Development of a flexible multi-objective design tool ... 5
1.2.3 Objective 3: Identifying key design drivers relating the blade geometry and performance ... 6

2 Fundamental concepts **7**
2.1 Rotor performance ... 7
2.1.1 Steady performance characterisation ... 7
2.1.2 Blockage effects ... 8
2.2 Blade hydrodynamic loading ... 10
2.2.1 Steady loading definition ... 10
2.2.2 Transient blade loads ... 12

II Turbine geometry and modelling techniques **16**

3 The modelled turbine geometry **17**

4 Blade element theory and modelling applications **21**
4.1 Blade element theory ... 21
4.2 The blade element-momentum method ... 22
4.3 The RANS embedded blade element method ... 26
4.4 The actuator line method ... 28

5 Modelling practices for the actuator line method **31**
5.1 Details of the in-house actuator line method ... 31
5.2 Mesh and timestep constraints ... 33
5.3 Nacelle representation ... 34

III Free surface proximity effects **37**

6 Investigating the performance and loading of a tidal stream turbine operating near the free surface using the actuator line method **38**
6.1 Introduction ... 38
6.2 Methodology ... 41
6.2.1 Overview ... 41
6.2.2 Blade representation method ... 42
6.2.3 Numerical methods ... 42
6.2.4 Computational domain ... 43
6.2.5 Uncertainty estimation for deterministically varying quantities ... 45
6.3 Operation of tidal stream turbines in close proximity to a rigid boundary ... 46
6.3.1 Rotor performance ... 46
6.3.2 Azimuthal blade loading variations ... 49

6.3.3 Near-boundary flow effects 52
6.3.4 Relating boundary proximity impacts on blade loading to the experienced flow conditions 57
6.4 Free surface interaction effects of tidal stream turbines 59
6.4.1 Surface deformations 60
6.4.2 Rotor performance 62
6.4.3 Azimuthal blade loading variations 64
6.4.4 Near-boundary flow effects 66
6.5 Discussion 69
6.6 Conclusions 71

IV Blade design methods for tidal stream turbine rotors 73

7 Introduction 74

8 Iterative rotor design with thrust-based design criteria 80
8.1 Methodology of the existing RANS-BE design routine 80
8.2 Adaptation of design criteria to actuator line modelling 81
8.2.1 Design tool adaptation 81
8.2.2 Comparison of the RANS-AL and RANS-BE design tool outputs 82
8.2.3 Comparing actuator line, RANS-BE and blade resolved simulations without design iteration 83
8.3 Summary 86

9 Methodology of a deterministic blade design optimisation tool 88

10 Blade design optimisation with the blade element-momentum method 89

11 Blade design optimisation with the actuator line method 90

V Conclusions 91

12 Conclusions and future work 92
12.1 Conclusions 92
12.1.1 Free surface proximity effects 92
12.1.2 Blade design methods for tidal stream turbine rotors 93
12.2 Future work 93
12.2.1 Design validation and structural feasibility 93
12.2.2 Objective functions 93
12.2.3 Developments in rotor modelling techniques 94

Appendix A Rotor geometry coefficients 95

Appendix B Optimisation conditions 96

Bibliography 97

Abbreviations

2D	two-dimensional
3D	three-dimensional
AL	actuator line
AR	aspect ratio
BDC	bottom dead centre
BE	blade element
BEM	blade element-momentum
BR	blade resolved
CFD	computational fluid dynamics
CFL	Courant–Friedrichs–Lewy
COE	cost of energy
IB	immersed boundary
LMADT	linear momentum actuator disc theory
NR	nacelle resolved
RANS	Reynolds-averaged Navier-Stokes
RANS-AL	Reynolds-averaged Navier-Stokes - actuator line
RANS-BE	Reynolds-averaged Navier-Stokes - blade element
RBM	root bending moment
RL	rigid lid
SOUTTBP	Supergen ORE Unsteady Tidal Turbine Benchmarking Project
TDC	top dead centre
TI	turbulence intensity
TST	tidal stream turbine
VOF	volume of fluid

Nomenclature

Common variables

A	rotor swept area
A_c	cross-sectional area of the tidal channel or flow domain
B	global blockage ratio
c	chord length
C_d	hydrofoil drag coefficient
C_l	hydrofoil lift coefficient
C_P	power coefficient
C_T	thrust coefficient
d	blade sectional drag force per unit span
D	rotor diameter
f	blade sectional force per unit span
f_x	axial component of blade sectional force per unit span
f_θ	tangential component of blade sectional force per unit span
k	reduced frequency
l	blade sectional lift force per unit span
N_{Bl}	number of blades
N_t	number of turbines
P	rotor power
r	local radius
R	rotor radius
$R_{\mathbf{hub}}$	blade root radius
t	time
T	rotor thrust
u_x	blade local streamwise velocity at the rotor plane
u_θ	blade local tangential velocity at the rotor plane
U_∞	undisturbed or inflow velocity
V	blade local relative flow velocity
x	streamwise direction

y	cross-stream direction
z	vertical direction
α	angle of attack
β	blade geometric twist
δA	area increment on an actuator disc
δF_x	axial force generated by a blade element
δF_θ	tangential force generated by a blade element
δT	total axial force on an actuator disc area increment
Δp	pressure drop across an actuator disc element
Δx	rotor plane cell size
η	basin efficiency
θ	azimuth angle and direction
λ	tip-speed ratio
ρ	fluid density
σ_r	local solidity
τ	rotor period
ϕ	angle between the relative flow vector and the rotor plane
ω_g	angular frequency of a gust
Ω	rotor angular velocity

Part II: Modelling technique variables

a	axial flow induction factor
a'	tangential flow induction factor
$\tilde{a}$	azimuthally-averaged axial flow induction factor
$\tilde{a'}$	azimuthally-averaged tangential flow induction factor
a_b	blade-local axial flow induction factor
a'_b	blade-local tangential flow induction factor
$c_{\theta,_{Bl}}$	blade element torque coefficient
$c_{x,_{Bl}}$	blade element thrust coefficient
c_1	empirical coefficient used in the Wimshurst-Willden and Shen et al. tip corrections
c_2	empirical coefficient used in the Wimshurst-Willden and Shen et al. tip corrections
F	Glauert tip loss factor
F_1	Wimshurst-Willden or Shen et al. tip loss factor
N_ϵ	ratio of ϵ to the rotor plane cell size

r_c	radial distance from a collocation point
r_g	smearing radius
r_s	sampling radius
$u_{\theta,ds}$	tangential velocity prescribed downstream of an actuator disc
U_x	axial component of the flow velocity
δD	drag force generated by a blade element
δL	lift force generated by a blade element
δQ	total torque acting on an actuator disc area increment
δr	spanwise length of a blade element
Δs	distance travelled by the blade tip in a single timestep
Δt	timestep size
ϵ	smearing function strength parameter

Part III: Boundary proximity variables

N_B	number of bins
N_s	number of samples within an averaging bin
$\mathbf{RBM}_x$	flapwise root bending moment
$\mathbf{RBM}_\theta$	edgewise root bending moment
s	tip clearance to the free surface
U_θ	tangential component of the flow velocity
z_0	still water height
$\xi_{\mathbf{water}}$	phase fraction
ψ	angle between the blade sectional force and the axial direction

Part IV: Design optimisation variables

C	coefficient of the basis function approximation
C_p	pressure coefficient
c_x	local thrust coefficient
d_i	design variable
$f(\mathbf{d})$	aggregated objective function
$f_m(\mathbf{d})$	individual objective function
$\hat{f}(\mathbf{d}, \mu)$	penalised aggregated objective function
g	acceleration due to gravity
$g_k(\mathbf{d})$	inequality constraint function

h	finite-difference step length
$h_j(\mathbf{d})$	equality constraint function
L_{av}	length of a moving-average window
m_θ	blade sectional moment contribution per unit span in the tangential direction
n	gradient-descent iteration number
p	static pressure
$p_{\mathbf{atm}}$	atmospheric pressure
p_v	vapour pressure
t_{hr}	half-rise time of a perturbation
u	Chebyshev polynomial parameter space
w_m	objective function weighting parameter
Z	step length multiplier
Z_{init}	initial step length multiplier
γ_m	objective function scaling parameter
ζ_1	first Wolfe condition parameter
ζ_2	second Wolfe condition parameter
κ	step length parameter
κ_{init}	initial step length parameter
κ_{ref}	reference step length parameter
Λ	backtracking line search contraction parameter
μ	penalty parameter
Ξ	Chebyshev polynomial
$\Pi(\mathbf{d})$	penalty function
ς	stopping criterion
τ_r	rise time of a perturbation
υ	smoothing parameter in a piecewise linear approximation function
χ	arbitrary function
∇f	gradient of the objective function
$\mathbf{C}$	vector of basis function coefficients
$\mathbf{d}$	vector of design variables
$\mathbf{d}^*$	dominant vector of design variables
$\hat{\mathbf{e}}_i$	unit vector in the i^{th} direction
$\mathbf{S}$	search direction
$\mathbf{X}$	vector of observation locations

$\mathbf{Y}$	vector of discrete observations
$\mathbf{\Xi}$	matrix of Chebyshev polynomial observations

Frequently used notation

$\bar{.}$	time-averaged
$.^*$	quantity at the operational point for maximum C_P
$\langle . \rangle$	phase-averaged
SE	standard error
SE^{Φ}	standard error within a phase bin
σ^{Φ}	standard deviation within a phase bin
$\lvert . \rvert$	modulus
$\lVert . \rVert$	Euclidean norm of a vector
$\cdot_d$	the selected design value of a quantity
$\cdot_{md}$	quantity of a turbine operating at mid-depth

Part I

Introduction

Chapter 1

Background and objectives

1.1 Background

In 2024, the combined electricity generation from wind and solar sources exceeded that from gas-fired power stations in the UK for the first time. A total of 285 TWh was generated that year, 50.4% of which was from renewable sources [1]. Primarily due to the electrification of heating and transport, the Balanced Net Zero Pathway proposed in the UK Climate Change Committee's Sixth Carbon Budget estimates that annual electricity demand will rise to 610 TWh by 2050, and suggests that 80% of this should be produced by variable renewable sources [2]. The collective global commitment to mitigating climate change is exemplified by the Paris agreement, an international treaty between 194 parties that aims to limit the rise in global average temperature to well below 2°C above pre-industrial levels [3]. In light of this strategy, the UK has committed to reduce greenhouse gas emissions by 81% by 2035 relative to 1990 levels, and further aims to achieve net zero by 2050 [4].

However, as the national electricity demands are increasingly met by variable renewable sources, the challenge of balancing supply and demand becomes greater. For example, the overall grid balancing costs of 2024/25 were 10% higher than those in 2023/24 [5]. A review by the University of Edinburgh's Policy and Innovation Group states that no single technology can deliver the energy transition, and to do so in a cost-effective and secure manner will require a diverse and resilient energy mix, utilising all of the UK's resources [6].

The tidal stream energy concept harnesses power from tidal current flows, typically utilising the hydrodynamic forces on a horizontal axis rotor to drive an electrical generator. Given that the tidal flows are determined by astronomical cycles, their power generating potential can be accurately predicted far into the future with low levels of forecasting uncertainty relative to the solar and wind resources, providing an advantage in terms of grid balancing [7].

The current cost of energy generated by tidal stream turbines (TSTs) is estimated to be 240 £/MWh [7], significantly higher than that of offshore wind and solar technologies [8]. However, the predictability of the resource can have benefits to the energy system as a whole, for example by reducing the reliance on rapid-start, gas-fuelled power stations to make up the shortfall when the supply from other renewable sources is low, increasing energy security and minimising greenhouse

gas emissions [9]. A case study of the energy system on the Isle of Wight finds that integrating tidal stream energy with offshore wind and solar minimises the net energy shortage and surplus, reducing the reliance on reserve energy supplies [10]. The adoption of tidal stream energy also minimises the required capacity of short-term and inter-seasonal energy storage systems, and can provide a reduction in the whole-system cost of energy when the reserve energy supply price exceeds 240 £/MWh [10].

In addition to mitigating the environmental consequences of climate change, the decarbonisation of the energy supply should also provide socioeconomic benefit. The location of the most energetic tidal resources in the UK ensures that the commercialisation of tidal stream energy technologies will bring high value industrial activity, and provide skilled job opportunities and energy security to coastal and island communities [6]. For example, the development of the Morlais demonstration zone on Anglesey is expected to provide more than 230 jobs and generate up to £30 million in gross value added to North Wales [6].

The UK has positioned itself as the world leader in tidal stream energy, and is responsible for installing 19 MW of the 35 MW of global cumulative capacity [6, 11]. A review of 426 candidate sites estimates that $\sim 30\%$ of the global quasi-practical tidal stream resource is located in UK waters, anticipating the maximum practical annual energy yield to be 34 TWh, equivalent to 11% of the UK electricity demand in 2025 [11]. The European Marine Energy Centre is the world's leading facility for demonstrating wave and tidal stream energy devices in marine environments, and MeyGen is the largest operational tidal stream project with four 1.5 MW turbines currently in service [6]. By the end of 2025, the MeyGen site had exported 84 GWh of electrical energy to the grid, and has consent to increase its installed capacity to 86 MW. Meanwhile, the electrical infrastructure at the Morlais site was completed in 2023, and is consented for a total installed capacity of 240 MW. The project is backed by the Welsh Government, which has invested over £16 million into its development [6].

The emergence of the tidal stream energy industry in the UK has been enabled by government support, particularly through the Contracts for Difference scheme which encourages investment by shielding developers from the volatility of wholesale energy prices. Contracts were awarded to tidal stream energy projects totalling 122 MW of installed capacity in allocation rounds four, five and six, reflecting the government's commitment to array-scale tidal energy deployment [9]. In these rounds, tidal stream energy projects benefitted from a ringfenced minimum budget allocation, allowing them access to support without competing against other renewable energy technologies in the auction [6, 12]. The results of the latest allocation round (7a) were published in January 2026, in which an additional 20.9 MW of tidal stream energy projects were awarded contracts [13].

Although the budget was allocated separately for more established technologies such as offshore wind, tidal stream projects were required to compete with other emerging technologies, including wave energy, highlighting the importance of continued cost reduction to maintain government support.

For tidal stream energy to provide a meaningful contribution towards the energy transition, technological innovation is required to reduce the capital and operational costs, and to improve the reliability and energy yield [9]. Considering all cost reduction factors, the levelised cost of energy generated by TSTs is projected to fall to approximately 150 £/MWh by 2031, assuming a cumulative installed capacity of 160 MW by this point [7]. To support this cost reduction, the Offshore Renewable Energy Catapult's Tidal Stream Technology Roadmap outlines the areas of innovation with the greatest potential to reduce the cost of energy [9]. Those most relevant to the work in this thesis are discussed below.

Firstly, an increase in the rated generator power for devices of a particular rotor diameter is anticipated to yield cost reductions by increasing the annual energy yield at a given rated flow speed. Increasing the power per device allows a given site capacity to be realised with fewer turbines, reducing the length of cable required to connect the array. However, to ensure these generators can be driven reliably, the report identifies the need to improve understanding of the mechanical loads experienced by large turbines.

An increase in the rotor diameter is predicted to have the greatest potential to return significant cost savings. Similarly, increasing the rotor swept area increases the proportion of the energy resource which is captured by each device, increasing their individual annual energy production. Transport and manufacturing costs are expected to increase with blade length, and the structure will be required to withstand greater hydrodynamic loads. Despite this, increasing the rotor diameter was noted as one of the most effective cost-reduction drivers in the emergence of the offshore wind industry [9]. The specific spatial constraints imposed on TSTs, due to presence of the seabed and free surface, limit the maximum rotor diameter, highlighting the need for efficient blade design to maximise the energy yield from a particular rotor size.

Finally, the development of controllers which optimise the lifetime performance is expected to reduce the cost of energy by enabling devices and arrays to operate more efficiently, and across a wider range of flow conditions. Previously implemented control strategies, predominantly focussing on minimising the fatigue damage rate caused by cyclic loading, often negatively impacted the energy yield. While the work in this thesis does not explore control strategies, the trade-off between blade loading and energy yield is a central theme throughout.

1.2 Thesis outline and objectives

Designing and operating cost-effective tidal stream turbines requires careful consideration of the rotor performance and the structural loading which is necessary for energy extraction. The work in this thesis analyses the loading implications of power production on a 1.6 m diameter experimental turbine, firstly with respect to operation in close proximity to the free surface, and secondly in relation to the blade's hydrodynamic geometry through the study of rotor design processes. Although other modelling techniques are implemented as appropriate, the research primarily utilises the actuator line method to generate time-varying performance and loading data along the span of discrete blades, while capturing the effects of blockage.

The turbine geometry and modelling techniques are presented in Part II, identifying key similarities and differences between the methods. Part III reports the results of the boundary proximity study, examining the effects of surface deformation and revealing the underlying physics behind the load fluctuations. Finally, rotor design processes are reviewed in Part IV. A novel rotor design method using multi-objective optimisation is developed and tested, and the impacts of different modelling techniques on the obtained blade geometry are analysed.

The research is carried out with respect to the following three objectives:

1.2.1 Objective 1: Free surface proximity effects

The progression of the tidal stream energy industry towards higher capacity turbines, and the prevalence of floating device concepts, leads to rotors operating in closer proximity to the free surface relative to their diameter. The effects of flow constriction on turbine performance are widely acknowledged, and previous studies have identified load fluctuations associated with blades passing near flow boundaries. However, the connections between the azimuthal load variations, performance changes, and the governing flow mechanisms are not well understood for turbines operating near the free surface. The first objective of this thesis is to quantify the effects of free surface proximity on the performance and loading of tidal stream turbines, and to assess the suitability of the commonly-used rigid lid assumption which represents the free surface as an undeformable boundary.

1.2.2 Objective 2: Development of a flexible multi-objective design tool

The hydrodynamic design of tidal stream turbine rotors presents a unique challenge in that the optimal geometry is dependent on the blockage conditions. Specific design approaches which consider the intended operational blockage ratio have not been studied in detail, and the majority

of design methods aim to maximise only power production. However, such design criteria are unlikely to yield the most cost-effective rotors as minimising the cost of energy requires multiple, often competing, objectives to be considered simultaneously. The second thesis objective is to develop a novel rotor design method, capable of optimising the blade geometry relative to multiple cost-proxy objectives while capturing discrete blade and blockage effects.

1.2.3 Objective 3: Identifying key design drivers relating the blade geometry and performance

The blade geometry obtained from a particular design routine is expected to vary with the design objectives, the operating conditions and the modelling approach. The final objective is to determine the dominant geometric features which drive the performance relative to different design objectives, and to identify those which arise due to the characteristics of the modelling technique or tip treatment.

Chapter 2

Fundamental concepts

2.1 Rotor performance

2.1.1 Steady performance characterisation

Tidal stream turbines extract energy from the current by applying a resistance to the flow. The rotor thrust (T) is the force applied in the axial direction, and the mechanical power generated is denoted by P. The power and thrust coefficients, C_P and C_T respectively, are dimensionless expressions of a turbine's performance, and are defined in Equations 2.1 and 2.2, in which U_∞ is the undisturbed flow velocity in the tidal channel, ρ is the fluid density, and A is the rotor's swept area.

$$C_P = \frac{P}{\frac{1}{2}\rho {U_\infty}^3 A} \tag{2.1}$$

$$C_T = \frac{T}{\frac{1}{2}\rho {U_\infty}^2 A} \tag{2.2}$$

Assuming the hydrodynamic performance of the blades is independent of the Reynolds number (see, for example, the NACA0012 aerofoil at pre-stall angle of attack and Reynolds number greater than 5×10^5 in [14]), the power and thrust coefficients of a particular rotor design are a function of the tip-speed ratio (λ), defined in Equation 2.3 where R and Ω are the rotor's radius and angular velocity respectively.

$$\lambda = \frac{\Omega R}{U_\infty} \tag{2.3}$$

The C_P - λ and C_T - λ profiles are referred to as the performance curves, and characterise a rotor's steady-state performance at different combinations of flow velocity and rotational speed.

However, the rotor power does not account for all of the energy removed from the flow as some is lost to viscous dissipation, particularly through the remixing of the core and bypass flows in the wake. The basin efficiency (η) represents the ratio of energy extracted by the turbine to the total energy removed from the flow, quantifying the efficiency of resource utilisation. This should be considered as a performance metric alongside the power and thrust coefficients, particularly if the total capacity of turbines deployed at tidal sites is to increase beyond the current pre-commercial scales.

Applying linear momentum actuator disc theory (LMADT) to a tidal channel of constant cross-sectional area, which assumes that the change in free-surface height due to energy extraction

is small relative to the water depth, Vogel [15] showed that the total power removed from the flow can be expressed as the product of the total thrust and U_∞. In LMADT, the actuator disc provides the only source of thrust, whereas the flow through a real turbine experiences a thrust force from both the rotor and the support structure. The turbine nacelle, which generates a small thrust relative to the rotor, is the only part of the support structure modelled in this work. Hence, the total power removed from the flow is approximated as $T\,U_\infty$, and the basin efficiency is defined as in Equation 2.4.

$$\eta = \frac{P}{T\,U_\infty} = \frac{C_P}{C_T} \tag{2.4}$$

The theoretical optimum performance of a wind turbine was independently derived by Lanchester, Betz and Joukowsky using LMADT, assuming incompressible flow which is unconstrained in an infinite domain. The power coefficient describes the ratio of the power generated to the kinetic energy flux through an equivalent rotor area in the undisturbed flow, and is predicted to have a maximum value of 16/27 under these conditions [16]. This maximum, often referred to as the Betz limit, occurs when the rotor presents the optimum resistance to the incoming flow, imparting enough force to maximise the power production without overly choking the flow through the rotor. The optimum resistance occurs when the axial velocity at the rotor plane becomes 2/3 of the free stream flow speed, corresponding to a thrust coefficient of 8/9. However, the water depth in which TSTs are typically operated is of a similar order to the rotor diameter, so the assumption of an infinite domain is not appropriate. The presence of the nearby seabed and free surface constrains the flow, changing the balance of optimal rotor resistance. Consequently, the Betz limit is not directly applicable to TSTs [17, 18].

2.1.2 Blockage effects

Blockage effects refer to the influence of flow constraint, provided by flow boundaries or other nearby turbines, on a rotor's performance and loading. The proportion of the channel's cross-sectional area (A_c) which is occupied by the swept area of turbine rotors on a specific plane is known as the global blockage ratio (B). Assuming that the turbines have the same swept area ($A = \pi R^2$), the global blockage ratio is defined as in Equation 2.5, where N_t is the number of turbines.

$$B = \frac{N_t \pi R^2}{A_c} \tag{2.5}$$

For a given operating condition, the power and thrust coefficients of a TST typically increase with the degree of blockage in its flow domain. Constraining the bypass flow causes it to accelerate, reducing its static pressure. Assuming that the static pressure of the core and bypass flows become

equal at some downstream position, the accelerated bypass flow results in an increase in the static pressure drop across the rotor plane, allowing a greater thrust to be sustained by the rotor [19].

This effect was captured by Garrett and Cummins [20] in their application of LMADT to a parallel sided channel with constant free surface height, demonstrating that the maximum power coefficient is modified to become $(16/27)(1-B)^{-2}$. Hence, the Betz limit can theoretically be exceeded in blocked flow domains, and increasing B always increases the maximum C_P. The model of [20] was later extended to include the effects of free surface deformation associated with open channel flow at a non-zero Froude number, predicting even greater exceedance of the Betz limit [18, 21].

The one-dimensional models of [18], [20] and [21] assume that the blockage is uniform in the vertical and horizontal directions, applicable to a single turbine in a square channel or a closely-spaced co-planar array spanning the entire width of a rectangular channel. As these scenarios are unlikely to occur in practice, the influence of channel aspect ratio (AR) was assessed alongside the effects of blockage ratio by simulating an actuator disc in a three-dimensional domain with the Reynolds-averaged Navier-Stokes (RANS) method [22]. It was found that the maximum C_P and C_T were higher when operating in the channel with AR=4 than those at AR=1, However, the effects of AR were minor in comparison to those of channel blockage. The study demonstrated numerically that the Betz limit could be exceeded in blocked domains, and found the performance limits predicted by one-dimensional LMADT to be satisfactory.

Turbines arranged in co-planar arrays experience flow constraint on two scales: a global blockage, as discussed previously, and a local blockage determined by the lateral spacing between rotors. The local blockage is defined as the ratio between the swept area of a single rotor and the area of its local flow passage. Considering economic and regulatory constraints, variations in site bathymetry, and the impacts on shipping and mammal passage, installing co-planar arrays which span the entire width of a channel may not always be feasible [23]. Practical turbine deployment is more likely to be in the form of partial arrays, only spanning part of the channel. Nishino and Willden [24, 25] introduced the two-scale blockage concept for such cases, and demonstrate that TSTs spaced closely in a partial co-planar array can exceed the Betz limit even in an infinitely wide channel where the global blockage ratio is negligible. They found that an optimal inter-turbine spacing exists for a given global blockage ratio, and in the case of an infinitely wide channel, the array performance depends on the local blockage only. The concept of local blockage has since been observed in numerous numerical and experimental studies [19, 25, 26, 27, 28, 29, 30].

Blockage effects also affect the optimal hydrodynamic design of TST rotor blades. Schluntz and Willden [31] utilised the design approach developed by [32] to generate rotor geometries optimised

for different blockage ratios. Rotors designed for more highly constrained flow environments had greater solidity as they apply more thrust to the flow to reach their maximum power coefficient. Also, in agreement with the theoretical predictions of [20], the axial velocity through the rotor plane was lower at the operational point for maximum power in more highly blocked conditions. Hence, the blade twist angle required to achieve to the target angle of attack decreased as blockage increased [31]. The various rotor designs were simulated with the Reynolds-averaged Navier-Stokes - blade element (RANS-BE) method across the range of blockage ratios, each time finding that the maximum power coefficient was achieved by the rotor designed for that particular blockage condition.

Two of the rotors designed by [31] were simulated at higher fidelity by Wimshurst and Willden [33] using blade resolved RANS computational fluid dynamics (CFD) to validate their performance. The rotors were confirmed to produce the maximum power at their intended blockage ratio, at a tip-speed ratio close to the optimal predicted by RANS-BE. However, the rotor designed for unblocked conditions could produce similar power in the blocked domain to the rotor designed for that blockage ratio if it was operated at a higher tip-speed ratio, thereby increasing its thrust. Hence, the operational strategy could mitigate the performance deficit due to design, but only if the rotational speed is not limited by cavitation or generator constraints [33].

2.2 Blade hydrodynamic loading

2.2.1 Steady loading definition

The hydrodynamic torque and thrust produced by the rotor are the sum of the tangential moments and axial forces generated across each of the blades. The majority of the blade span forms a hydrodynamic lifting surface, designed with a hydrofoil shaped cross-section. The forces can be analysed per unit span at each radial station by analysing two-dimensional (2D) cross sections of the blade, as in Figure 2.1 which illustrates the key velocity components and parameter definitions.

The relative flow vector (V) is the sum of all velocity contributions, and its angle to the rotor plane is denoted by ϕ. The axial velocity contribution at the rotor plane (u_x) is driven by the tidal current, but is lower than in the free stream as the thrust decelerates the incoming flow. The tangential velocity contribution has two sources: the relative tangential motion velocity (Ωr) at a given radial position (r), and the whirl velocity (u_θ) which is induced in the opposite direction to the rotor's torque to satisfy the conservation of angular momentum. The blade is designed with decreasing geometric twist (β) from root to tip to maintain a target angle of attack (α), particularly as ϕ changes with the increasing Ωr component. The angle of attack is the incidence angle between

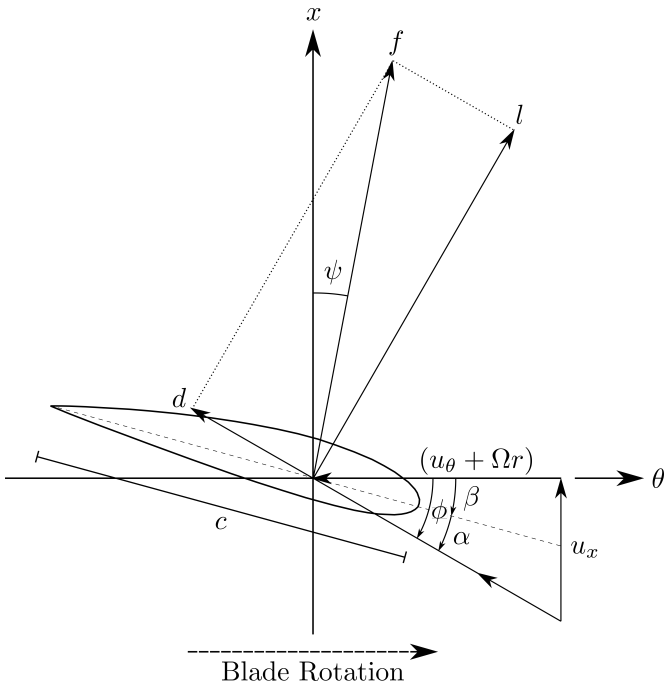


Figure 2.1: An illustration of key velocity components and force vectors used to determine the sectional blade loads with the blade element method.

the hydrofoil's chord line and V.

The performance of each hydrofoil geometry is characterised by the non-dimensional lift and drag coefficients, C_l and C_d, which vary as a function of α and Reynolds number, and are typically obtained from numerical simulations or experiments. At each radial location, the hydrofoil profile generates lift and drag forces, defined to be perpendicular and parallel to the relative flow vector, respectively. Equations 2.6 and 2.7 define the magnitude of the lift and drag forces per unit span in steady flow conditions, l and d, where c is the chord length of the hydrofoil section. The blade sectional force (f) is the vector sum of the lift and drag forces, also measured per unit span.

$$l = \frac{1}{2}\rho V^2 c C_l(\alpha) \tag{2.6}$$

$$d = \frac{1}{2}\rho V^2 c C_d(\alpha) \tag{2.7}$$

The angle between the blade sectional force vector and the streamwise direction is denoted by ψ, hence, the axial and tangential components of f are $f\cos(\psi)$ and $f\sin(\psi)$, respectively. The rotor thrust is the integral of the axial component of f across the span of all blades. Similarly, the torque is the spanwise integral of the tangential moment generated by f about the rotor's axis. Particularly near the blade tips, the lift force is predominantly in the axial direction, contributing to the thrust, while the drag force is largely in the tangential direction, opposing torque generation. The positive

torque, and hence power, is driven by the small component of lift which is resolved in the direction of rotation. Thus, a large lift-to-drag ratio is sought for effective torque generation, and typical hydrofoils used for horizontal axis rotors achieve maximum lift-to-drag ratios of $C_l/C_d \sim 100$ within the Reynolds number range encountered by commercial-scale TST blades [14].

The blades of axial flow TSTs are typically configured as a cantilever beam, fixed only to the hub at the root connection, located at radius R_{hub}, and free at the tip. It is typical to report blade loading in terms of the root bending moments (RBMs), which are the moments generated by the hydrodynamic forces about the root connection. The root bending moment in the flapwise direction (RBM_x) is linked to the rotor thrust, but considers the radial distance from the root connection at which the axial force is generated. The edgewise root bending moment (RBM_θ) is similar to an individual blade's contribution to the torque, but measured about R_{hub}.

The above discussion assesses the forces generated by TST rotor blades under steady flow conditions by considering the flow around 2D hydrofoil sections. However, this neglects three-dimensional (3D) flow effects and the spanwise transfer of momentum which is prevalent near the blade tips, and significantly impacts the loads generated in this region [34]. At the tip of the blade, the static pressure on the suction and pressure surfaces must equalise. The resultant spanwise pressure gradients lead to a rotational flow component around the tip which is shed into the wake as a tip vortex. The shed vorticity induces downwash and spanwise flow accelerations, decreasing the angle of attack and reducing the difference between the static pressure on the suction and pressure surfaces [35, 36]. This tip loss mechanism causes a reduction in the blade loads as the tip is approached, such that the forces are lower than predicted by 2D hydrofoil analysis.

2.2.2 Transient blade loads

The average current flow speed and direction at a tidal site are predictable; however, the flow environment at the device scale is complex with numerous sources contributing to the unsteadiness in the flow velocity experienced by the rotor blades. The phenomena which contribute to the spatial and temporal unsteadiness in the flow can be categorised as deterministic or stochastic. The predominant deterministic sources are associated with the blade rotating through a spatially varying flow field leading to periodic load fluctuations. These include rotation through the vertical shear profile generated by seabed roughness, the blade passing support structures, or anisotropy in the local flow passage due to boundaries or other nearby turbines [30, 37, 38]. Stochastic unsteadiness primarily arises from the velocity perturbations and platform motions induced by surface waves, as well as turbulence generated by seabed roughness, underwater bathymetry features and upstream turbines [37].

Various studies have been conducted to assess the impact of the unsteady flow sources on turbine loading and performance. Blade resolved CFD and experimental testing find the influence of upstream turbulence intensity on the mean power and thrust coefficients to be minimal [39, 40]. However, the increase in power and thrust fluctuations with turbulence intensity are significant [40]. A similar study to [39], but including a realistic turbulence and mean velocity profile, reports performance and load fluctuations due to the interaction with the shear layer and support structure [41]. Scarlett and Viola [42] study the combined effects of the vertical shear layer, waves and turbulence. They find waves to be the largest source of RBM fluctuations, while turbulence also leads to significant load peaks. The load variations caused by rotation through the shear layer were found to be negligible in comparison to those driven by waves and turbulence [42].

Studies isolating the impact of waves report significant load fluctuations, but the effect of waves on the mean power and thrust is insignificant; see, for example, [43, 44, 45, 46, 47, 48]. Using an approach based on the blade element-momentum (BEM) method with unsteady hydrodynamic modelling, Scarlett et al. report RBM fluctuations of up to 50% of the mean load when operating close to the optimal λ in large waves. Upon simplifying their model, they found that quasi-steady predictions of the time-varying loads were reasonable. However, operating the turbine at below optimal tip-speed ratios lead to a significant region of the blades experiencing flow separation and dynamic stall, in which case the simplified model with quasi-steady approximations underpredicted the load amplitude relative to their unsteady BEM-based model [43].

Turbines mounted on floating support structures also experience changes in their relative flow velocity due to the response of the platform to surface waves. The impact on turbine loading and performance has been investigated numerically through prescribed displacements replicating platform surge [49, 50, 51], roll [52], heave [51] and pitch [51]. In all cases, the mean performance coefficients were affected, and increasing the motion amplitude and frequency increased the rotor loads. At large amplitudes of surge and pendulum motion, flow separation can occur as the turbine advances into the flow causing abrupt power losses [50, 51].

At the hydrofoil scale, unsteadiness in the relative flow vector affects the blade loads through changes in the angle of attack and velocity magnitude. In addition, depending on the time scale of the unsteadiness, the hydrofoil's lift and drag coefficients at a particular angle of attack can deviate from their steady-state value [53, 54]. Quasi-steady predictions of blade loads differ from the unsteady response as they do not include the effects of added mass and the unsteady wake [53]. The added mass effect is associated with the resultant force on the hydrofoil due to acceleration of the fluid around it, introducing hysteresis to the lift-α curve. The unsteady wake effect refers to the vorticity shed from the trailing edge due to changes in the hydrofoil's circulation, required to

satisfy Kelvin's theorem [55]. The shed vorticity induces downwash on the hydrofoil which damps the lift response to a gust, reducing the peak load and introducing a phase shift [54].

The degree to which the hydrofoil behaviour deviates from steady-state performance depends on the reduced frequency, $k = \omega_g c/V$, where ω_g is the angular frequency of the gust [53, 56]. The flow can be considered quasi-steady when $k \leq 0.1$ and unsteady for larger values of k [53]. The sources of unsteadiness experienced by a TST are classified by Sequeira and Miller [56], reporting that the velocity perturbations induced by surface waves can be considered quasi-steady, while the higher frequency fluctuations due to turbulence are expected to result in unsteady hydrofoil behaviour.

The contribution of unsteadiness to the axial blade root bending moment was quantified experimentally by subjecting a TST to planar oscillatory motions in the surge direction with reduced frequency up to $k = 0.14$ [57, 58, 59]. The unsteady loads increased with oscillation frequency, exceeding the steady loads by a maximum of 15% in attached flow conditions [58, 59]. Flow separation occurred at a lower tip-speed ratio, in which case the maximum unsteady load was 25% greater than the steady loads due to dynamic stall effects [57, 59].

The quasi-steady hydrofoil force calculation used in rotor models based on 2D blade element theory can be corrected for unsteady flow effects by the use of dynamic stall models. A commonly used example is the Beddoes-Leishman model [60], implemented in [43, 44], which reverts to the Theodorsen function when the flow is attached [61]. The Theodorsen function [61] is an analytical transfer function, derived for a 2D flat plate, which relates the unsteady load variations to the 2D quasi-steady prediction [53]. However, 3D flow effects are expected to be significant on TST blades due to their low aspect ratio, leading to studies of their influence on the unsteady load response [54, 61, 62]. Smyth et al. [61] investigate the unsteady loads on a TST blade modelled with the 2D Theodorsen function, a 3D inviscid vortex lattice model, and blade resolved (BR) unsteady RANS. The 2D model does not predict the same loading amplitude and phase as the 3D models as no tip vortex is produced, so the effects of its downwash are not captured [61]. The 2D model provides a conservative estimate of the load amplitude provided that a steady tip loss correction is not applied. However, if a tip loss correction is used, the unsteady load amplitude can be severely underestimated [61, 62].

These investigations demonstrate the challenges in accurately simulating the unsteady load response of TSTs with reduced fidelity models relying on the blade element (BE) method. While the actuator line (AL) method also uses the BE method in its force calculation, it is known to produce tip vortices [63] so should experience the corresponding downwash. To the best of the author's knowledge, an application of the AL method with dynamic stall model for horizontal axis

turbines is not present in the literature, so its potential efficacy in modelling the unsteady load response remains to be determined.

Part II

Turbine geometry and modelling techniques

Chapter 3

The modelled turbine geometry

A single turbine geometry is used throughout this thesis to model the effects of boundary proximity and to serve as a reference point in the rotor design processes. The turbine has a 1.6 m diameter three-bladed rotor, and was designed and manufactured in-house to gather experimental reference data for the Supergen ORE Unsteady Tidal Turbine Benchmarking Project (SOUTTBP) [64]. The geometry specification is publicly available [65], and access to detailed accounts of the design process has been beneficial to this work. The rotor was designed with a single hydrofoil profile along the entire length of the blade span, without a transition piece at the root connection. This allows numerical modellers to more easily reproduce the blade shape, and avoids the need to interpolate between polars when using methods which rely on pre-defined hydrofoil data tables. In addition, the turbine has been modelled by numerous groups across academia and industry, using a variety of techniques, the results of which are compared to those generated in the carefully conducted experiments [66].

The SOUTTBP aims to improve the accuracy of modelling techniques, and build confidence in their use for evaluating the loads on TSTs by engaging the community in blind prediction exercises. The first phase of the project received 26 submissions from 12 research groups seeking to reproduce the loading and performance results of the turbine in steady flow conditions [66]. The turbine was sized to achieve Reynolds number independence allowing comparison to full-scale devices. The

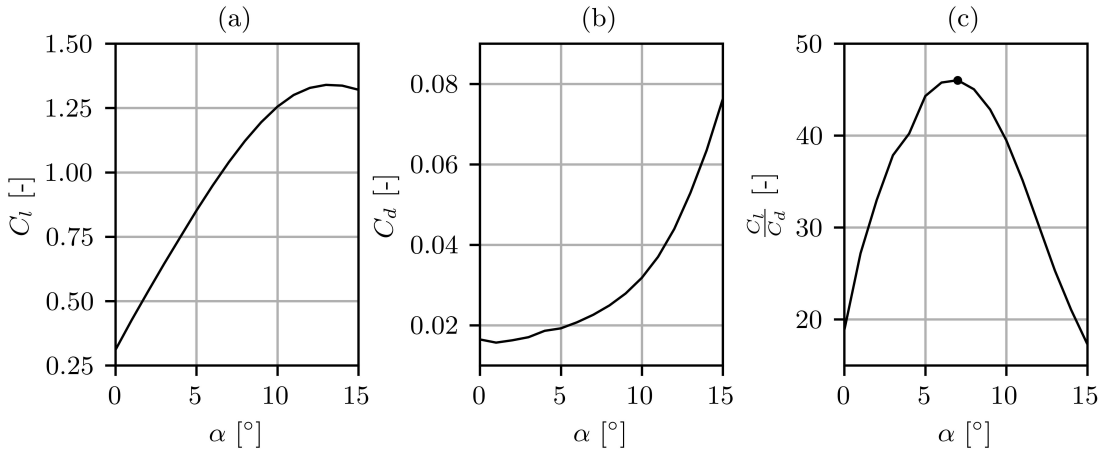


Figure 3.1: The variation of (a) lift coefficient, (b) drag coefficient and (c) lift-to-drag coefficient ratio for the NACA 63-415 hydrofoil with trailing edge thickening function at $TI = 1.0\%$, as provided by the organisers of the SOUTTBP [65]. The point of maximum C_l/C_d ratio, at $\alpha = 7^{\circ}$, is marked.

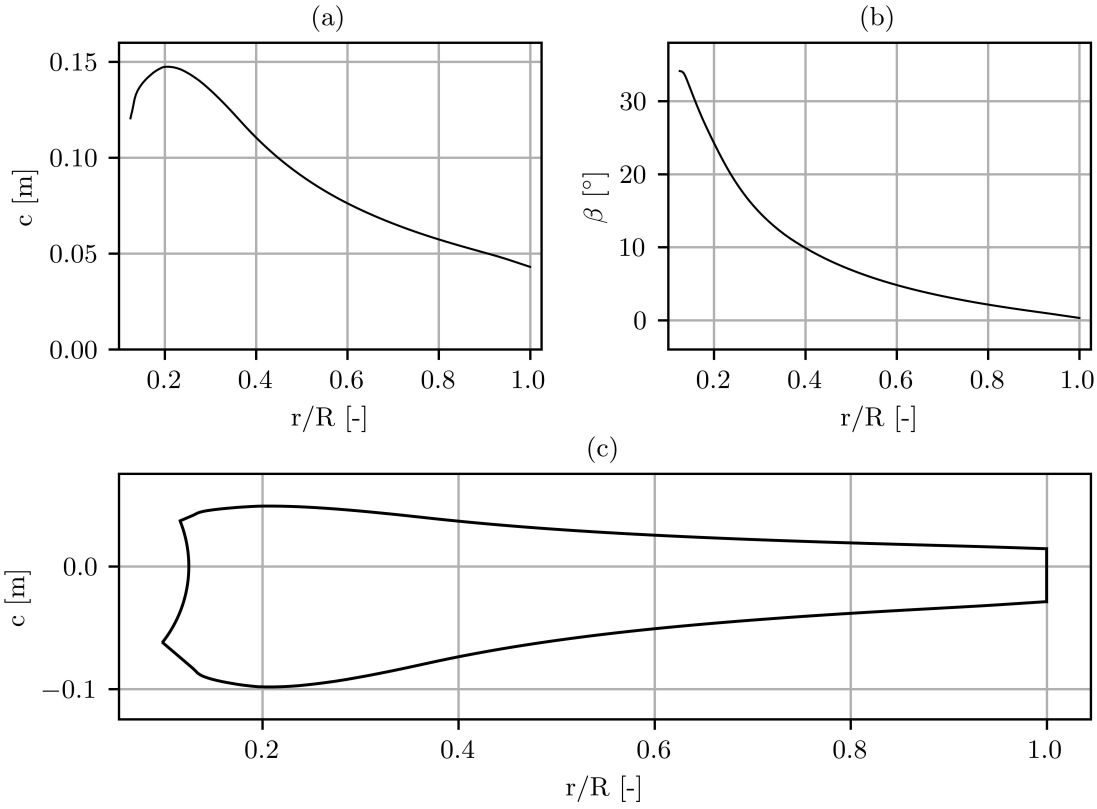


Figure 3.2: The (a) chord and (b) twist distributions which describe the hydrodynamic shape of the SOUTTBP turbine blades [65]. Tile (c) shows the blade planform, plotted as the chordwise blade length centred on the one-third chord position, and is linearly interpolated to meet the nacelle surface at the root. The axes of tile (c) are scaled to maintain the true geometric ratio.

Reynolds number based on the blade chord length is post-transitional, between 250×10^3 and 300×10^3, at the design tip-speed ratio ($\lambda_d = 6$) [67]. To keep the blockage ratio low (3.05%), the experimental testing was carried out at the QinetiQ Haslar towing tank, which has a width of 12.2 m (7.625D), a water depth of 5.4 m (3.375D), and is 270 m in length. As the turbulence intensity (TI) in towing tank facilities is typically very low, a turbulence grid with a porosity of 0.95 was mounted upstream of the turbine for half of the steady-flow experiments. The carriage speed remained at 1.0 m/s for tests with and without the turbulence grid, and the flow conditions are referred to as *Elevated Turbulence* and *Low Turbulence*, respectively. In the wake of the turbulence grid, without the presence of the turbine, the flow was measured to have $U_\infty = 0.899$ m/s and $TI = 3.1\%$ at the rotor plane location. When the turbulence grid was not in place, the TI was taken to be $\sim 0\%$ at an undisturbed flow speed of $U_\infty = 1.0$ m/s [67]. The turbine is instrumented with strain gauges at six locations along the blade span to measure the spanwise distribution of bending moments in the edgewise and flapwise directions. Strain gauges are also placed in the hub connection to measure the RBMs in both directions. A torque-thrust transducer is mounted along with a rotary encoder on the low-speed shaft to observe the total thrust and torque generated by

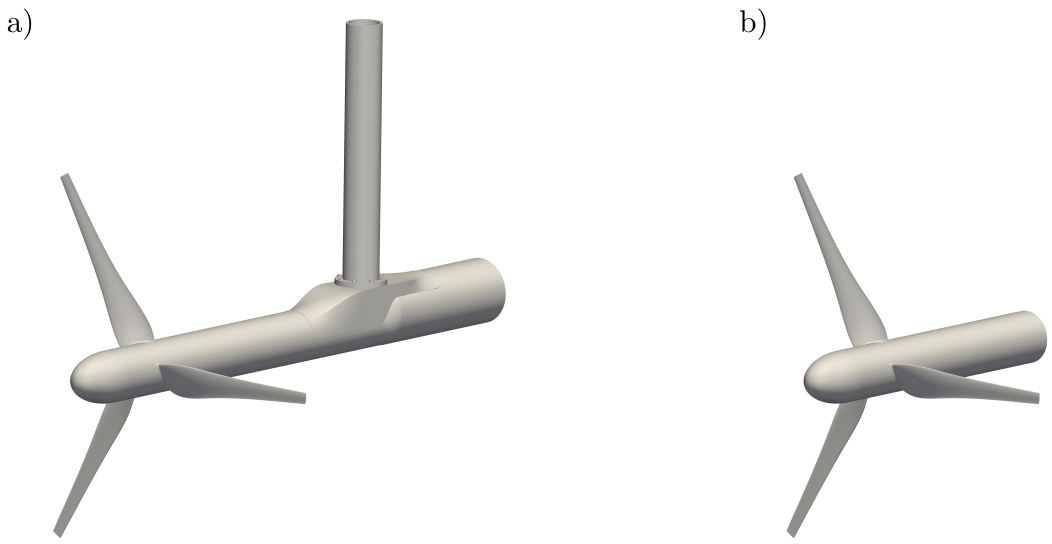


Figure 3.3: A 3D render of a) the full SOUTTBP device, and b) the sections of the device modelled in this work [65].

the rotor, and to record its angular position and rotational speed.

The NACA 63-415 hydrofoil profile was selected, and used across the entire length of the blade span. For safety and manufacturing purposes, the hydrofoil profile was modified by means of a thickening function to increase the trailing edge thickness to 0.625% of the chord length [68]. Hydrofoil polars were provided by the organisers of the SOUTTBP, shown in Figure 3.1, generated by 2D RANS simulations with k-ω SST turbulence closure across a range of angle of attacks and TIs. Unless otherwise stated, these polars are used when lift and drag coefficient data tables are required.

The hydrodynamic shape of the blades is described by the chord and twist distributions depicted in Figure 3.2. These profiles were generated using the RANS-BE design method, first introduced by [32] and discussed further in Chapter 8, in a cylindrical domain of equivalent blockage to the experimental towing tank facility. The target angle of attack is 6° at the design tip-speed ratio, maximising the C_l/C_d ratio in the hydrofoil polars available at the point of design, which differed slightly from the current data.

The nacelle of the experimental turbine is 2.4 m in length with an elliptical nose cone. The upstream section of the nacelle has a constant circular cross section of 0.2 m diameter which expands to 0.248 m just ahead of the tower. To minimise the meshing complexity, only the upstream 1.295 m nacelle section with constant diameter was included in the numerical modelling in this thesis. The tower has diameter 0.14 m and is positioned 1.3 m downstream of the rotor plane, however, it was also not modelled in this work to avoid the associated computational cost. Additionally, modelling the tower in the boundary proximity study would introduce variable parasitic drag as the turbine

immersion depth changes, and its inclusion in rotor design simulations would disrupt the azimuthal consistency required by the implemented design methods. Figure 3.3 shows the geometry of the entire experimental device, including the full nacelle and tower, alongside the portion of which is modelled in this work.

Chapter 4

Blade element theory and modelling applications

4.1 Blade element theory

Blade element (BE) theory, first introduced by Froude [69] to analyse propellers, is an approach to calculating the total force on a lifting surface by discretising the span into elements. The blade is divided into individual spanwise sections of length δr, and it is assumed that the hydrodynamic force generated by each element can be calculated using the 2D quasi-steady hydrofoil characteristics [14]. The relative flow velocity is considered only in the cross-sectional plane of the hydrofoil at the blade element, so any spanwise components of the flow are ignored. Three-dimensional flow effects are also not considered.

The lift and drag forces generated by a blade element are calculated using Equations 4.1 and 4.2, where c is the chord length at the element's midpoint, assuming linear chord variation within the element.

$$\delta L = l\delta r = \frac{1}{2}\rho V^2 c C_l \delta r \tag{4.1}$$

$$\delta D = d\delta r = \frac{1}{2}\rho V^2 c C_d \delta r \tag{4.2}$$

Using tabulated C_l and C_d data, this method can be used to approximate the total hydrodynamic force generated by a blade, knowing only the local flow velocity relative to each blade element and their cross-sectional shape.

Assuming an axisymmetric flow field at the rotor plane, and resolving the lift and drag forces into the axial and tangential directions, the thrust and torque increments produced by the blade elements of a rotor at a particular radius (r) are given by Equations 4.3 and 4.4, respectively, where N_{Bl} is the number of blades.

$$\delta T = \frac{1}{2}\rho V^2 c N_{Bl}(C_l \cos(\phi) + C_d \sin(\phi))\delta r \tag{4.3}$$

$$\delta Q = \frac{1}{2}\rho V^2 c N_{Bl}(C_l \sin(\phi) - C_d \cos(\phi)) r \delta r \tag{4.4}$$

4.2 The blade element-momentum method

The BEM method is a combination of blade element theory with a momentum-based analysis of an actuator disc, known as momentum theory. It provides a computationally inexpensive way of calculating the performance and loading on a rotor without numerically solving the flow field. The rotor plane area is discretised into a number of radially independent annuli, corresponding to concentric streamtubes within which momentum theory is applied separately. The blade element lengths are made equivalent to the radial widths of the annuli, and it is assumed that the rate of change of momentum of the fluid passing through each streamtube equates to the sum of the forces generated by the blade elements within it. Hence, the streamtubes are assumed to be independent with no radial transfer of momentum between them [14].

Under the assumption of an unbounded flow domain, applying momentum theory in the axial and tangential directions leads to expressions for the thrust and torque increments applied to the flow within each streamtube, Equations 4.5 and 4.6, respectively.

$$\delta T = 4\pi\rho r {U_\infty}^2 a(1-a)\delta r \tag{4.5}$$

$$\delta Q = 4\pi\rho r^3 U_\infty \Omega a'(1-a)\delta r \tag{4.6}$$

The expressions are written in terms of the axial and tangential induction factors, a and a', respectively. The axial induction factor represents the fractional reduction in axial velocity from the free stream to the rotor plane, as defined in Equation 4.7.

$$u_x = U_\infty(1-a) \tag{4.7}$$

Meanwhile, the tangential induction factor relates the tangential flow velocity immediately downstream of the rotor plane to the tangential velocity of the rotor through Equation 4.8.

$$u_{\theta,ds} = 2\Omega r a' \tag{4.8}$$

Given the incoming flow has no rotational velocity component, the total change in tangential velocity across the rotor plane is $u_{\theta,ds}$. In determining the incident flow vector on a blade element, the BEM method takes the tangential flow velocity at the rotor plane to be the average of its values immediately upstream and downstream, $u_\theta = u_{\theta,ds}/2$ [70]. Therefore, the axial and tangential components of the relative flow velocity incident on a blade element are $U_\infty(1-a)$ and $\Omega r(1+a')$, respectively, such that ϕ is defined according to the relationships in Equations 4.9, 4.10 and 4.11.

$$\sin(\phi) = \frac{U_\infty(1-a)}{V} \tag{4.9}$$

$$\cos(\phi) = \frac{\Omega r(1+a')}{V} \tag{4.10}$$

$$\tan(\phi) = \frac{U_\infty(1-a)}{\Omega r(1+a')} \tag{4.11}$$

Equating the thrust and torque formulae obtained from momentum theory with those derived from BE theory (that is Equation 4.5 with 4.3, and 4.6 with 4.4), while making use of Equations 4.9 and 4.10, leads to Equations 4.12 and 4.13 in which σ_r is the local solidity representing the proportion of the annulus occupied by blade elements.

$$\frac{a}{1-a} = \frac{\sigma_r(C_l\cos(\phi) + C_d\sin(\phi))}{4\sin^2(\phi)} \tag{4.12}$$

$$\frac{a'}{1+a'} = \frac{\sigma_r(C_l\sin(\phi) - C_d\cos(\phi))}{4\sin(\phi)\cos(\phi)} \tag{4.13}$$

$$\sigma_r = \frac{N_{Bl}c}{2\pi r} \tag{4.14}$$

However, without correction, the BEM method assumes an infinite number of blades and does not model the effect of tip vortices. Momentum theory considers the induction factor from the overall change of momentum within an annulus, assuming every fluid particle experiences the same interaction with the blades, and has the same loss of momentum. In reality, the finite number of blades means that fluid particles which pass between the blades are decelerated less than those which pass in close proximity to them. Hence, the induction factor local to the blades should be greater than the azimuthal average [36]. Also, as demonstrated by [14], the tip vortex causes large values of axial induction factor local to the blade, with greatest effect towards the tip.

The concept of a tip loss factor was introduced by Prandtl to account for the difference between an actuator disc and a rotor comprising of a finite number of blades [71, 72]. The tip loss factor (F) expresses the ratio between the azimuthally-averaged induction factors ($\tilde{a}$ and $\tilde{a'}$), used in momentum theory, and the blade-local induction factors (a_b and a'_b) required by the BE method [36, 72].

$$F = \frac{\tilde{a}}{a_b} = \frac{\tilde{a'}}{a'_b} \tag{4.15}$$

Prandtl proposed an expression for the tip loss factor, which was later simplified by Glauert [73] to the form shown in Equation 4.16 to be more easily applied to BEM modelling [36, 72]. An example of the radial profile of the Glauert tip loss factor is illustrated in Figure 4.1 [73].

$$F = \frac{2}{\pi}\cos^{-1}\left[\exp\left(-\frac{N_{Bl}(R-r)}{2r\sin(\phi)}\right)\right] \tag{4.16}$$

Under the assumption that the rotor is comprised of an infinite number of blades, the azimuthally-averaged and blade-local induction factors are identical. Hence, the blade element

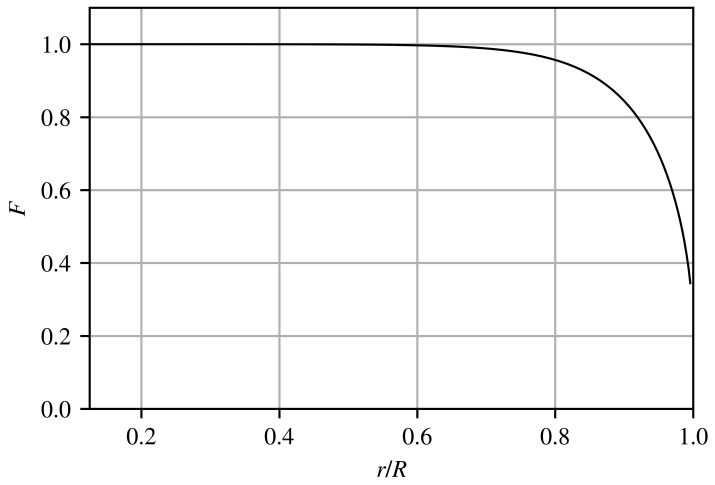


Figure 4.1: An example of the radial profile of the Glauert tip loss factor [73].

equations and the momentum equations can be expressed in terms of general axial and tangential induction factors, allowing them to be solved as described above. However, for a rotor with a finite number of blades, the blade element equations (Equations 4.3 and 4.4) and the relationships which define the inflow angle (Equations 4.9, 4.10 and 4.11) are functions of the blade-local induction factors, while the momentum equations (Equations 4.5 and 4.6) are functions of the azimuthally-averaged inductions factors. In Glauert's BEM formulation, the tip loss factor is used to write the momentum theory expressions for the thrust and torque increments in terms of the blade-local induction factors as in Equations 4.17 and 4.18 [72, 74].

$$\delta T = 4\pi\rho r {U_\infty}^2 a_b F(1-a_b)\delta r \tag{4.17}$$

$$\delta Q = 4\pi\rho r^3 U_\infty \Omega a'_b F(1-a_b)\delta r \tag{4.18}$$

Hence, Equations 4.12 and 4.13 become Equations 4.19 and 4.20.

$$\frac{a_b}{1-a_b} = \frac{\sigma_r(C_l\cos(\phi) + C_d\sin(\phi))}{4F\sin^2(\phi)} \tag{4.19}$$

$$\frac{a'_b}{1+a'_b} = \frac{\sigma_r(C_l\sin(\phi) - C_d\cos(\phi))}{4F\sin(\phi)\cos(\phi)} \tag{4.20}$$

The effect of the Glauert tip loss correction on the blade-local flow velocity components is illustrated in Figure 4.2. The tip loss factor drives the blade-local induction factors to 1 at the tip [72], decreasing both u_x and u_θ. The reduction of u_x, which acts to decrease ϕ, has a more significant effect than the reduced u_θ, which acts to increase ϕ, leading to an overall reduction of the inflow angle. Consequently, the angle of attack is decreased, reducing the lift and drag coefficients and, ultimately, the blade forces.

The typical implementation of the BEM method solves Equations 4.19 and 4.20 iteratively, starting from an initial guess of a_b and a'_b. Using Equation 4.11 and the geometric twist of each

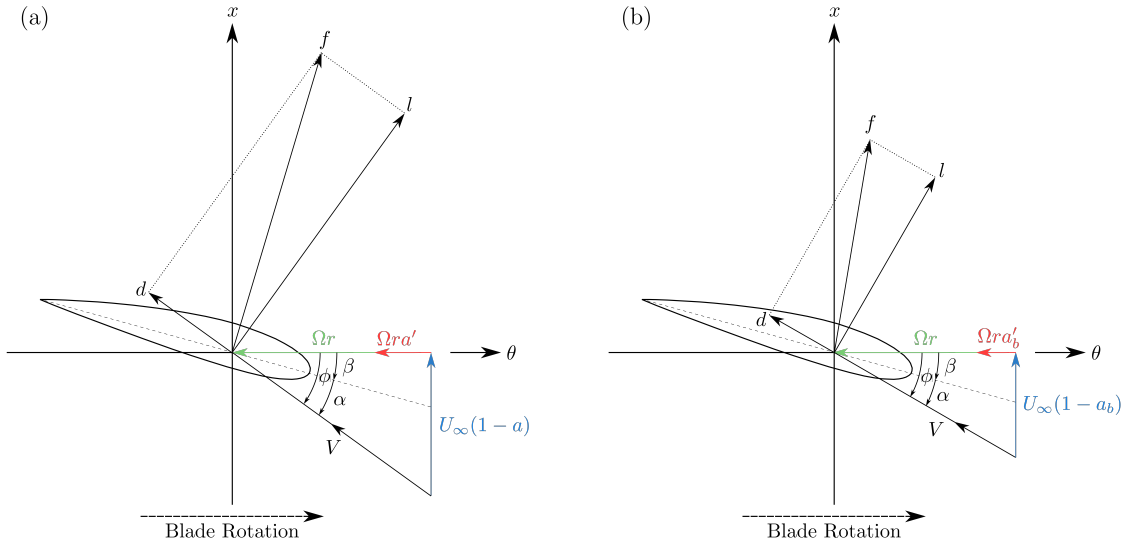


Figure 4.2: An illustration of the blade-local velocity components which are obtained from the BEM method near the blade tip (a) without and (b) with the Glauert tip correction [73]. The inclusion of the tip loss factor decreases u_x, u_θ and α, ultimately reducing the forces generated by the blade section.

blade element, the current values of the induction factors are used to calculate ϕ and α, hence C_l and C_d can be determined from tabulated hydrofoil data. The right hand side of Equations 4.19 and 4.20 are solved, and used to generate new values of a_b and a'_b. The iterative process is repeated until the values of a_b and a'_b converge. However, this work adopts another approach to solving the BEM equations, proposed by Ning [75], which is proven to be numerically efficient while guaranteeing convergence. The BEM equations are reduced to a single equation in terms of ϕ enabling the use of root-finding algorithms such as Brent's method [76].

Following Ning's formulation [75], the right hand side of Equations 4.19 and 4.20 are defined as Υ and Υ' (Equations 4.21 and 4.22), respectively, for convenience.[1] Hence, the axial and tangential induction factors are solved as in Equations 4.23 and 4.24, respectively.

$$\Upsilon \equiv \frac{\sigma_r(C_l\cos(\phi) + C_d\sin(\phi))}{4F\sin^2(\phi)} \tag{4.21}$$

$$\Upsilon' \equiv \frac{\sigma_r(C_l\sin(\phi) - C_d\cos(\phi))}{4F\sin(\phi)\cos(\phi)} \tag{4.22}$$

$$a_b(\phi) = \frac{\Upsilon(\phi)}{1 + \Upsilon(\phi)} \tag{4.23}$$

$$a'_b(\phi) = \frac{\Upsilon'(\phi)}{1 - \Upsilon'(\phi)} \tag{4.24}$$

[1] Note that, in the work of Ning [75], Υ and Υ' are denoted as κ and κ'.

The induction factors are now expressed as functions of the local inflow angle, and can be related through the geometric relationship described by Equation 4.11. Finally, Equation 4.11 is rearranged to form a residual function (Equation 4.25), for which a satisfying solution of ϕ is found using a one-dimensional root-finding algorithm.[2]

$$f(\phi) = \frac{\sin(\phi)}{1 - a_b} - \frac{U_\infty \cos(\phi)}{\Omega r(1 + a'_b)} = 0 \tag{4.25}$$

In addition to Glauert's tip loss correction, Ning's BEM approach also implements Buhl's [77] empirical correction for the axial momentum model at high induction factors ($a_b > 0.4$). Further details can be found in [75].

4.3 The RANS embedded blade element method

The RANS embedded blade element (RANS-BE) method uses the incident flow data obtained from CFD in the blade element equations to calculate the forces generated by a rotor modelled as an actuator disc. The rotor's interaction with the flow is modelled by imposing the calculated forces as a boundary condition on the surface of the actuator disc. This section describes the in-house implementation developed by [32] for modelling tidal turbines which, uniquely, incorporates an optional tool for iterative rotor design. Similar approaches combining numerically modelled actuator discs with blade element force calculations have been applied to studies of both wind [78, 79, 80] and tidal [81, 82] turbines.

The in-house model is azimuthally averaged when the iterative rotor design tool is in use, applying the rotor forces uniformly within each annulus. When used for modelling only, individual cells of the actuator disc can be treated independently allowing the rotor forces to be non-uniform in an anisotropic flow field. The blades are not modelled discretely; instead, the total chord at each radial location is accounted for by the local solidity (σ_r) defined in Equation 4.14.

The flow velocity is extracted from the RANS simulation and used to calculate the lift and drag forces generated by a blade element, which are resolved into the axial and tangential directions to give δF_x and δF_θ respectively.

$$\delta F_x = \delta L \cos(\phi) + \delta D \sin(\phi) \tag{4.26}$$

$$\delta F_\theta = \delta L \sin(\phi) - \delta D \cos(\phi) \tag{4.27}$$

The corresponding non-dimensional coefficients are the blade element thrust and torque coefficients, $c_{x,_{Bl}}$ and $c_{\theta,_{Bl}}$, defined in Equations 4.28 and 4.29.

$$c_{x,_{Bl}} = C_l \cos(\phi) + C_d \sin(\phi) \tag{4.28}$$

[2] Note that, in the work of Ning [75], Equations 4.11 and 4.25 are written in terms of a local tip-speed ratio $\lambda_r = \Omega r / U_\infty$.

$$c_{\theta,_{Bl}} = C_l \sin(\phi) - C_d \cos(\phi) \tag{4.29}$$

The turbine's axial force is imparted on the flow as a static pressure drop across the disc, calculated as the total axial force (δT) per unit area (δA) as in Equation 4.30.

$$\Delta p = \frac{\delta T}{\delta A} = \frac{1}{2}\rho {V}^2 \sigma_r c_{x,_{Bl}} \tag{4.30}$$

Unlike irrotational actuator disc methods, the tangential force is also modelled. This tangential force is imparted on the flow by introducing a tangential velocity component ($u_{\theta,ds}$) immediately downstream of the disc in the direction opposite to turbine rotation. The downstream tangential velocity, defined by Equation 4.31, is derived by equating the torque acting on the flow passing through an increment of disc area to its change of angular momentum.

$$u_{\theta,ds} = \frac{\frac{1}{2}\rho {V}^2 \sigma_r c_{\theta,_{Bl}}}{\Delta p u_x} \tag{4.31}$$

In a manner consistent with analytical BEM models, the tangential velocity at the rotor plane is assumed to be half of the downstream value. Hence, the relative inflow velocity is calculated as in Equation 4.32.

$$V = \sqrt{\left(\Omega r + \frac{u_{\theta,ds}}{2}\right)^2 + {u_x}^2} \tag{4.32}$$

When the model is implemented axisymmetrically, δA is the annulus area ($2\pi r \delta r$), and δT and δQ are the sum of contributions from all of the blade elements (see Equations 4.33 and 4.34).

$$\delta T = N_{Bl} \delta F_x \tag{4.33}$$

$$\delta Q = N_{Bl} \delta F_\theta r \tag{4.34}$$

However, when the force increments are calculated independently for each cell of the actuator disc, the total blade area within an annular ring ($N_{Bl} c \delta r$) is apportioned according to the ratio of the cell area to the annulus area. As described by [26], given the modification factor to the increment of force and the area over which they act are the same, Equations 4.30 and 4.31 are applicable to both individual cells and disc annuli.

Through this approach, the forces generated by a rotor of known geometry are modelled in combination with the flow domain, inherently capturing their interaction and the resultant blockage effects. However, similar to the BEM method, the actuator disc model cannot capture discrete blade effects and no tip vortices are produced. Hence, the Glauert tip loss correction is often used with the in-house RANS-BE implementation.

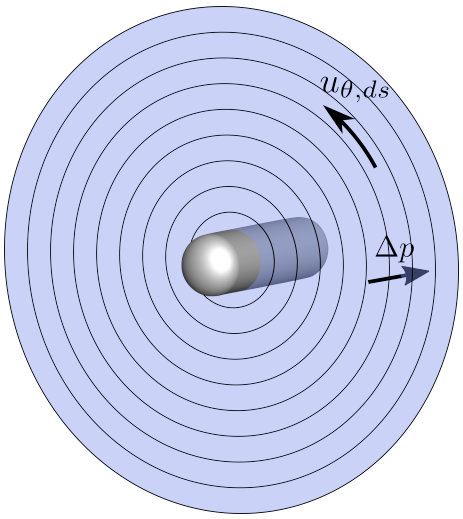


Figure 4.3: An illustration of the turbine representation in the RANS-BE method. The nacelle is resolved in the mesh, while the rotor is represented as an actuator disc, divided into annuli. The axial and tangential forces are imposed on the flow as a pressure drop across the disc (Δp) and a tangential velocity ($u_{\theta,ds}$) immediately downstream of the disc, respectively.

4.4 The actuator line method

The actuator line (AL) method utilises BE theory to calculate the forces at a series of points, known as collocation points, which discretise lines representing the position of the blades in time and space. The assumption of an axisymmetric distribution of rotor solidity used in the BEM and RANS-BE methods is relaxed, instead, the forcing region is concentrated around the collocation points creating a virtual discrete blade representation. The forces are embedded in unsteady CFD simulations, and the collocation points are rotated around the nacelle in time, modelling the time-varying response of each blade independently.

During each timestep, the AL method implements a routine of four key steps, some of which are illustrated in Figure 4.4. First, the collocation points are advanced around the azimuth by an angle $\Delta\theta = \Omega\Delta t$, where Ω is the rotor's angular velocity and Δt is the timestep size. Once in their new position, the flow field is sampled at each collocation point and the result combined with the blade's local tangential velocity to determine the angle of attack and relative velocity magnitude. The hydrodynamic forces generated by each blade section are calculated using the blade element method, with hydrofoil lift and drag coefficients obtained from pre-determined data tables according to the sampled angle of attack. The resultant blade forces are imposed on the flow field and the flow momentum equations are advanced in time.

The AL method was first introduced for horizontal axis rotors by Sørensen and Shen [83] to model the wake dynamics and tip vortices of wind turbines. Since then, it has been widely used as a medium-fidelity modelling tool to study both wind and tidal turbine rotors, offering an attractive compromise between computational expense and resolved physics. Importantly for

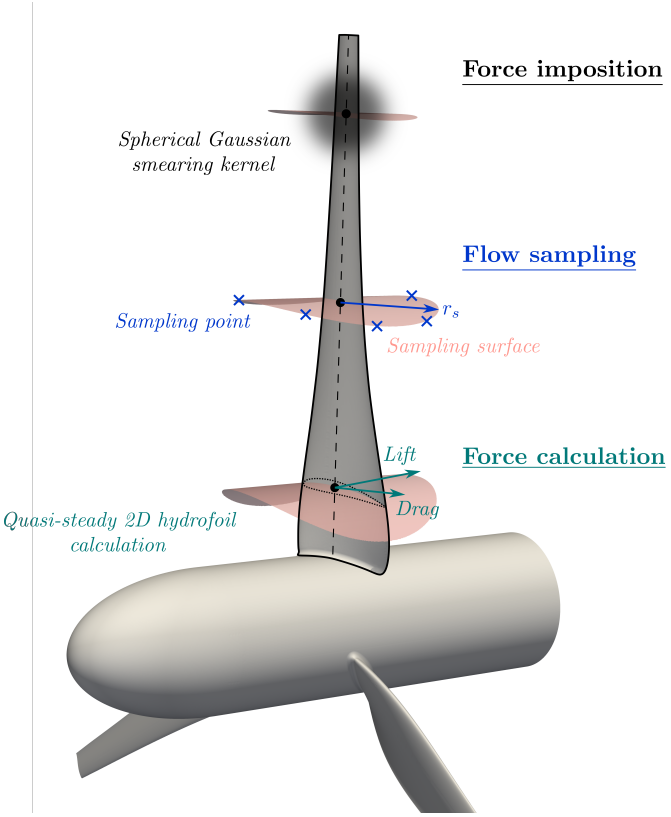


Figure 4.4: An illustration of the stages involved in the AL method including 1) flow sampling (blue annotations) on a curved sampling surface (pink), 2) the force calculation by BE method (green annotations), and 3) the force imposition using a spherical Gaussian smearing kernel (black annotations). The 3D blade geometry is not resolved in the mesh, but represented virtually as a set of collocation points (solid black circles) distributed along the blade span (dashed black line).

wake studies, tip and root vortices are produced by the discrete blade forcing strategy [63], and differences between actuator disc and AL predictions have been studied [63, 84]. Embedding the virtual discrete blade representation in unsteady 3D CFD allows the investigation of a turbine's response to non-uniform flow fields, as would be experienced in real operation. Meanwhile, the blade geometry is not resolved in the mesh, negating the need to model their surface boundary layers with fine cell resolutions. Additionally, the mesh does not need to be altered to modify the blade geometry or pitch angle, and rotor displacements can be prescribed without dynamic meshing strategies. Since the spatial and temporal variations of performance and loading are modelled, the AL method has been utilised in studies of tidal turbines in numerous non-uniform flow conditions. Examples include studies of turbines in arrays [26, 85], exposed to various combinations of waves, shear and turbulence [47, 86, 87, 88], subject to prescribed platform motions [89, 90], and in close proximity to the free surface [38].

However, there are drawbacks to virtually modelling only the main effects of the lift and drag forces, which are predicted under the assumption of 2D quasi-steady hydrofoil behaviour. Although the main vortical structures are produced, the fine-scale turbulence generated by viscous interaction

with the blade surface are not. For modelling rotor loads, the reliance on tabulated hydrofoil data is a limitation, and discretising the blade into independent elements ignores spanwise pressure gradients. This assumption of two-dimensionality is not always valid, particularly near the blade tips, and the load reduction associated with tip loss effects is not accurately reproduced without correction. To address this, tip loss corrections have been designed specifically for the AL method, such as the Shen et al. correction [72] and the Wimshurst-Willden correction [91]. Also, since the input data tables store steady-state lift and drag coefficients, unsteady hydrofoil behaviour cannot be fully reproduced. Finally, the AL method is sensitive to the numerical setup parameters, and in-house codes require experience and validation to produce reliable results. However, the impact of these setup choices have been studied, primarily for wind turbine applications [63, 92, 93, 94], but also for tidal turbines [94].

Chapter 5

Modelling practices for the actuator line method

5.1 Details of the in-house actuator line method

The in-house implementation of the AL method is built as a source term model for OpenFOAM. Following [94], 101 collocation points are used per blade, radially spaced along the span with a cosine distribution which provides greater measurement density at the root and tip where the spanwise gradients are expected to be largest.

In the flow sampling phase, the 2D angle of attack and relative flow velocity magnitude must be deduced from the inherently 3D flow field in the rotor vicinity. The hydrofoil lift and drag coefficients used in the BE force calculation are tabulated according to an angle of attack defined relative to a uniform free-stream velocity; hence, the flow disturbance caused by the blade's presence must be eliminated from the measured flow velocity. This challenge is not unique to AL methods, and numerous flow sampling strategies have been developed to extract the angle of attack from the flow fields of both AL and blade resolved simulations. Details of alternative sampling methods can be found in [94, 95, 96, 97], for example. In this work, the line average sampling method with 8 points is chosen as it has been found to be more robust than other approaches with less sensitivity to the timestep size (Δt) and forcing parameters [94]. This approach, first introduced by Jost et al. [96], samples the velocity field at an even number of points, diametrically opposed and spaced evenly around the circumference of a circle centred on the collocation point. Owing to symmetry, taking the average of the flow sampled at each point eliminates the circulatory velocity induced by the bound vorticity, returning the undisturbed blade-local flow velocity at the collocation point. As shown in Figure 4.4, the sampling points are placed on a cylindrical surface of constant radius to the rotor's axis, in accordance with the local 2D coordinate system of the rotating hydrofoil section. The spanwise velocity component is not included in the determination of the flow velocity magnitude. The sampling radius (r_s) defines the radial distance at which the sampling points are placed around the collocation points. This is chosen to be $1.1r_g$, where r_g is the smearing radius within which the blade forces are imposed, ensuring that the flow is sampled outside the disturbed region.

Table 5.1: The Wimshurst-Willden tip correction coefficients used in this work [36].

	c_1	c_2
Axial direction	0.108	20.90
Tangential direction	0.141	15.15

To avoid a numerical singularity when imposing the sectional blade forces on the flow field, the forces at each collocation point are apportioned to the surrounding cells within r_g according to a spherical Gaussian smearing function. This smearing kernel shape was introduced by Sørensen and Shen [83], and is described by Equation 5.1 where r_c is the distance from the collocation point.

$$\eta_\epsilon(r_c) = \frac{1}{\epsilon^3 \pi^{3/2}} e^{-(r_c/\epsilon)^2} \tag{5.1}$$

The width of the smearing function (r_g) is controlled by its standard deviation ϵ, with $r_g = 3\epsilon$. Following [93], ϵ varies radially from 33% of the blade's average chord at the root to 33% of the local chord at the tip, according to a power function which roughly approximates the shape of the chord distribution. The extent of the forcing region is calculated on simulation start-up, so is adjusted as the geometry evolves in the blade design optimisation activities presented in Chapter 11.

In the majority of this work's AL simulations, the Wimshurst-Willden tip correction [91] is applied to account for the impact of 3D flow effects on the blade sectional loading in the vicinity of the blade tips. It is a recalibration of the earlier Shen et al. correction [72], applied anisotropically such that the tangential force is penalised more aggressively than the axial force (see Figure 5.1). To implement both the Wimshurst-Willden and Shen et al. corrections, the blade sectional forces computed from the lift and drag coefficients are multiplied by the correction factor F_1 before they are imposed on the flow field. However, the Wimshurst-Willden approach defines F_1 separately, using a unique set of c_1 and c_2, for forces in the axial and tangential directions.

$$F_1 = \frac{2}{\pi} \cos^{-1} \left[\exp \left(-g_1 \frac{N_{Bl}(R-r)}{2r \sin(\phi)} \right) \right] \tag{5.2}$$

$$g_1 = \exp(-c_1(N_{Bl}\lambda - c_2)) + 0.1 \tag{5.3}$$

Wimshurst and Willden perform rotor specific calibrations of c_1 and c_2 to generate the penalisation functions required to collapse the loading distributions generated by uncorrected AL onto those observed in BR simulations [34, 91]. The specific set of coefficients used in this work, given in Table 5.1, are calibrated for a TST rotor designed by [31] for low blockage operation. The influence of different tip treatments on the performance modelled by the in-hourse AL method was investigated as part of the SOUTTBP, comparing the numerically predicted and experimentally measured power and thrust coefficients across a range of tip-speed ratios. The choice of tip correction did

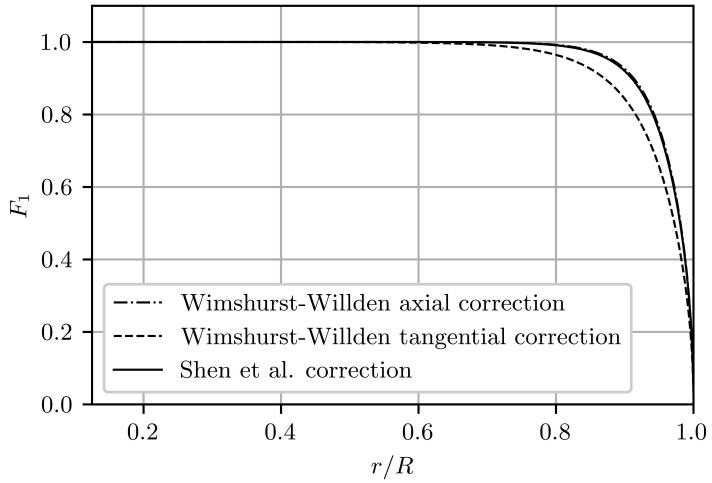


Figure 5.1: The radial distribution of the Shen et al. [72] and Wimshurst-Willden [91] tip correction factor at λ=6.

not significantly affect the thrust coefficient. However, the power coefficient modelled with the Wimshurt-Willden tip correction more closely agreed with the experimental data than that obtained with the Shen at al. correction [38].

5.2 Mesh and timestep constraints

The width of the smearing kernel is known to affect the numerical stability of AL simulations, and the accuracy of their load predictions. Larger values of ϵ reduce the sensitivity to user defined parameters, and Martínez-Tossas et al. [63] find that the $N_\epsilon = \epsilon/\Delta x \geq 5$ is required for the power to become independent of the rotor plane cell size (Δx). A widely observed constraint is that ϵ should be at least twice the value of Δx, or $N_\epsilon \geq 2$. This was found to be necessary to avoid numerical oscillation [92]. However, excessively large smearing kernels overly diffuse the body force relative to the effective size of the blade, negatively affecting the production of tip vortices. Shives and Crawford [93] find that $\epsilon/c = 0.25$ is sufficiently small to produce an accurate tip vortex core radius. However, they also note that larger values are reasonable given the mesh density must increase to maintain stability as ϵ decreases, and predict that the solution would only be affected very close to the tip. The implemented value of $\epsilon/c = 0.33$ at the blade tip balances computational cost and modelling accuracy, while remaining close to the recommendations of [93].

Throughout this work, the mesh at the rotor plane is kept at a uniform resolution, with Δx chosen to meet the stability constraint of $N_\epsilon \geq 2$ [63, 92]. Given the radius of the forcing region roughly approximates the chord distribution, the maximum cell size at the rotor plane is limited by the value of ϵ at the blade tips. The resultant mesh has 230 cells per diameter, within the range used by [98], classifying this AL application as amongst those focussed on the accuracy of blade

load modelling according to the description of Zormpa et al. [94].

The necessary temporal resolution of AL simulations is typically not governed by the streamwise Courant–Friedrichs–Lewy (CFL) condition, but rather the more restrictive timestep condition associated with the tangential velocity of the blade tip. The distance travelled by a collocation point within a timestep (Δs) should not exceed the length of a single cell. Hence, the timestep constraint is expressed as $\Delta s/\Delta x = \Omega R \Delta t/\Delta x \leq 1$, where Δt is the timestep size. Therefore, for a given rotational speed, the timestep is limited by the cell size at the rotor plane. This condition is widely observed in AL studies to ensure a smooth application of the rotor force [63, 83, 92].

The presence of spurious oscillations in the rotor plane velocity field, which motivated the $N_\epsilon \geq 2$ constraint, are found by [94] to be a function of both N_ϵ and Δt. Using a large timestep relative to the smearing radius leads to insufficent overlap of the forcing regions between subsequent actuator line positions, resulting in spurious momentum streaks in the flow field. When the line average sampling method is used with $N_\epsilon = 2$, Zormpa et al. [94] show that $\Delta s/\Delta x = 1$ is sufficient for power convergence, and that spurious oscillations in the flow field are eradicated once the number of timesteps per rotations exceed 200. In this work, the timestep is adjusted to maintain $\Delta s/\Delta x = 1$, equivalent to ~ 700 timesteps per rotation at the optimal operating point of the SOUTTBP turbine.

5.3 Nacelle representation

An adequate nacelle representation is essential to correctly model the root flow velocity. Without a nacelle, the lack of resistance leads to accelerated flow through the centre of the rotor and errors in the axial velocity predicted at the root of the blade [63]. Two nacelle representation methods are considered: a nacelle resolved (NR) technique and an in-house version of the immersed boundary (IB) method previously used by Apsley et al. [85] for similar AL model applications.

The IB technique first approximates the surface topology using a polygonal cut through the intersection points of the surface with a given cell's boundaries. The resulting partial cell blocking is achieved by modifying the source term in the finite-volume equations for the momentum components. Combining the AL method with an IB represented nacelle allows very simple, quick to generate, background meshes to be used as there is no resolved geometry. As shown in Figure 5.2, there are no empty regions to which the mesh must conform. For the NR method, OpenFOAM's snappyHexMesh is used to automatically conform the square grid cells to the curved nacelle surface. In both modelling approaches, a cylindrical refinement region encompasses the nacelle, the diameter of which is 1.5 times the nacelle diameter, and generates a background mesh of the same density as that at the rotor plane. When the geometry is resolved in the mesh, an additional level of

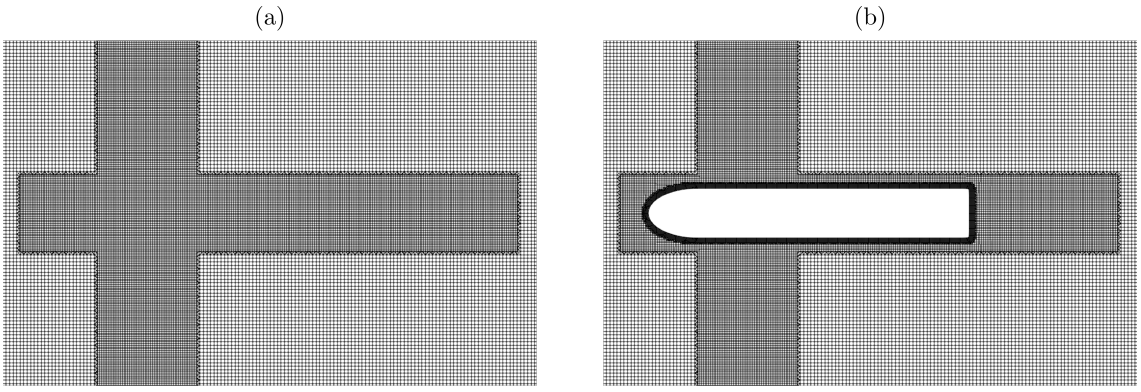


Figure 5.2: A cross-sectional view of the near-nacelle meshes used for the a) IB and b) NR nacelle representations.

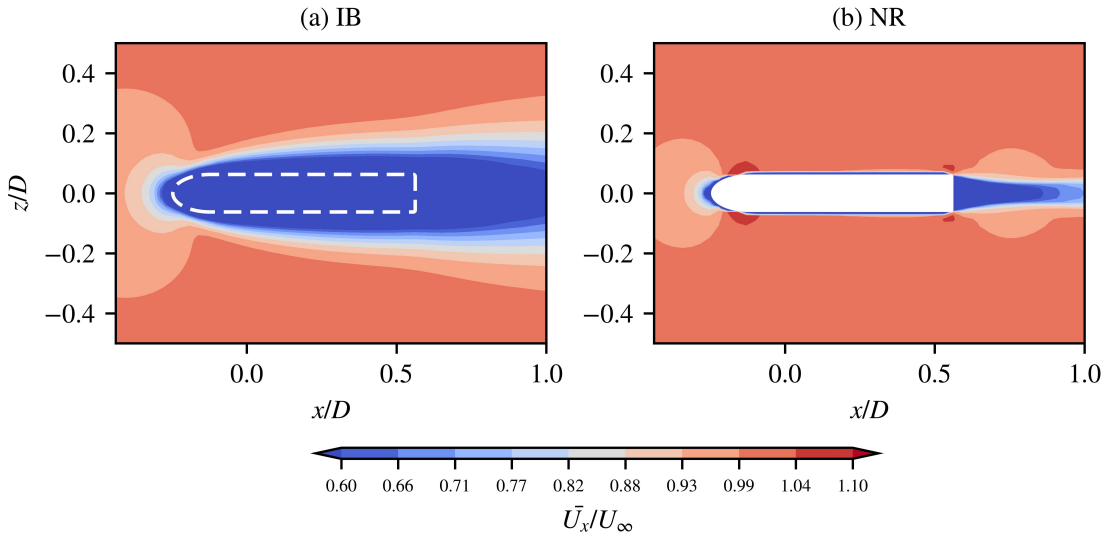


Figure 5.3: Contours of the normalised time-averaged axial flow velocity on a streamwise-vertical surface in the vicinity of isolated nacelles (no rotor) modelled using the (a) IB and (b) NR methods. Tile (a) outlines the region in which the nacelle is modelled virtually with a dashed line.

refinement is applied to cells within 0.1 nacelle diameters of its surface to achieve a y^+ value of 95, suitable for the use of wall functions. Despite the additional refinement, the empty region in the NR mesh results in a similar number of cells to the IB mesh.

The two techniques are compared by simulating the nacelles in isolation, without the presence of rotor forces from actuator lines. Figure 5.3 presents the time-averaged axial flow velocity on the x-z plane at $y = 0$, and shows that the IB modelled nacelle generates a larger region of decelerated flow, and a wider nacelle wake, than that modelled with the NR approach. This observation is consistent with that of [99], who report the axial force on an IB modelled nacelle to be ~ 1.5 times greater than a NR counterpart.

A vertical traverse of time-averaged axial flow velocity at the rotor plane is depicted in Figure 5.4, confirming that the in-house IB method generates a significantly thicker nacelle boundary layer

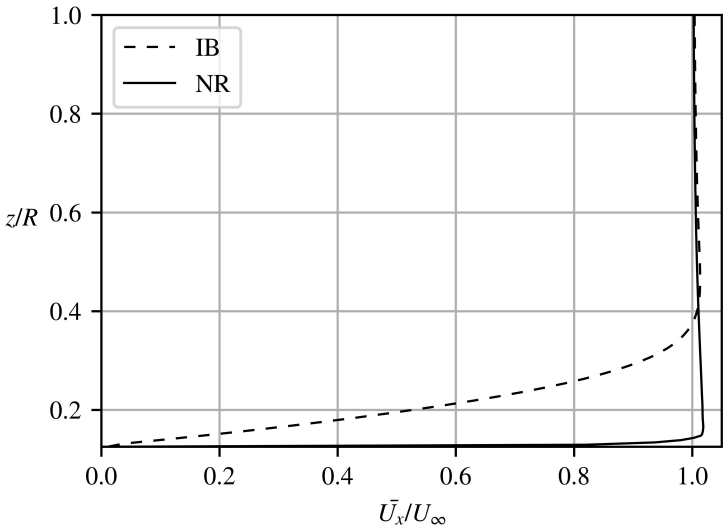


Figure 5.4: The normalised time-averaged axial flow velocity in the vicinity of isolated nacelles (no rotor) modelled using the NR and IB methods. The velocity data are extracted at the intended rotor plane, and are plotted from the nacelle surface ($z/R = 0.125$) to the edge of the intended rotor swept area ($z/R = 1.0$).

than the NR mesh. Consequently, the use of the in-house IB approach results in a large proportion of the blade's inboard section, up to $r/R = 0.4$, being placed in a region of reduced the streamwise velocity, decreasing the local blade forces. The impact of the nacelle representation approaches on the rotor performance is demonstrated in the results of the SOUTTBP. The reduction of blade forces in the root region decreases the power and thrust predictions of AL simulations using an IB nacelle relative to those which resolve its geometry in the mesh [38]. Additionally, an underprediction of the streamwise velocity reduces the angle of attack, which would result in root twist angles which are less than optimal in reality should the IB approach be used in rotor design simulations. While the IB method has benefits due to its simplicity, the NR technique is adopted for this work for a more physical representation of the near-nacelle flow.

Part III

Free surface proximity effects

Chapter 6

Investigating the performance and loading of a tidal stream turbine operating near the free surface using the actuator line method

6.1 Introduction

Recent trends in the emerging tidal stream energy industry see developers moving towards increasingly larger rotor diameters to increase the energy yield per device. Additionally, locating turbines close to the surface, for example by supporting them below floating platforms, allows easier access compared to seabed mounted devices, presenting an attractive opportunity for reducing operation and maintenance costs. Furthermore, operating at the top of the shear layer maximises the flow speed at rotor plane [37], potentially leading to greater energy extraction. Consequently, rotor designs increasingly occupy a larger proportion of the water column, and are likely to be operated with a lower surface tip clearance relative to their size. However, operating in the vicinity of a fluid boundary introduces azimuthal variations in the flow environment leading to time-varying blade loads which increase the fatigue damage rate necessitating more robust blade design [30]. As boundary proximity effects become more prevalent in the operation of tidal stream turbines, it becomes increasingly important to quantify and understand their impact on the rotor performance and blade loads.

As discussed in Section 2.1.2, flow constriction effects associated with the boundaries of the flow domain or other nearby turbines impact the maximum power generating potential of a TST. While studies of global blockage effects often assume the flow constriction to be isotropic, considering only the channel area, the proximity of the rotor to the flow boundaries has a secondary influence on the performance. Nishino and Willden show, using RANS simulations of an actuator disc, that the maximum C_P and C_T can be increased slightly when the aspect ratio of a channel with constant cross-sectional area is increased from $AR = 1$ to $AR = 4$ [22]. Keogh carried out further investigation through experiments on a single porous disc in a circulating water flume [100]. By

varying the free surface height and flow velocity, they investigated the effect of AR in the range $AR = 1 \rightarrow 7$ at constant Froude number. They find that the disc's thrust coefficient initially increases with AR up to a point, beyond which increasing AR begins to decrease C_T. The optimal AR was found to be dependent on the channel blockage ratio, and the AR-C_T behaviour was attributed to changes in the balance of vertical and lateral flow constriction as the aspect ratio changes. Mascrier et al. also find the relationship between the degree of domain anisotropy and the rotor performance to be non-linear in their RANS simulations of a turbine modelled using the AL method [101]. In channels of low global blockage ratio, increasing the channel aspect ratio decreased the thrust and power coefficients. However, at higher values of B, a minor uplift in C_P was observed when the channel aspect ratio was increased from $AR = 1$ to $AR = 3.3$. Additionally, anisotropy in the domain introduced a loading cycle to the tangential force generated by an individual rotor blade. Relative to those generated in a square domain, the tangential forces increased when the blade was adjacent to the nearer boundaries, and decreased when it passed those made further away by the channel's AR [101].

The above studies explore anisotropic flow constriction effects by varying the shape of a rigid-boundary domain around a centrally located rotor. However, similar effects may also arise due to proximity to the free surface, in which case the flow constriction is likely to be greater above the rotor than below, and the nearby boundary can deform. The effect of free surface proximity on the performance of a 0.8 m diameter turbine was investigated by varying its immersion depth in a towing tank [102]. As the tip clearance to the free surface was decreased from $0.55D$ to $0.19D$, the power coefficient decreased by 10% - 15%. A similar effect was observed by Wang et al. [103], who studied the performance of a TST at various immersion depths, including those which result in the blades penetrating the free surface, using multi-phase CFD simulations. When the rotor remained full submerged, the time-averaged C_P and C_T decreased with the tip clearance as the performance of an individual blade was diminished in the region adjacent to the free surface. However, a study by Kolekar et al. reported contrasting results when a turbine was tested in a recirculating water channel [104]. The power coefficient increased when the tip clearance was decreased from $0.55D$ to $0.27D$ due to the accelerated bypass flow velocity and compression of the wake as the free surface height decreased behind the rotor plane. However, C_P decreased relative to the value at $0.27D$ as the clearance was reduced further to $0.05D$. The same performance trends are observed in a prior study by Kolekar and Banerjee [105], using a similar experimental setup to [104]. In this case, complementary multi-phase CFD simulations with the volume of fluid (VOF) method were also performed, numerically reproducing the acceleration of the constrained bypass flow and the surface height reduction immediately downstream of the rotor [105].

Assuming the surface deformations are small, and noting the differences in the pressure boundary condition, the fluid boundary presented by the free surface is expected to approximate the behaviour of a symmetry plane. Hence, the proximity effects experienced by two co-planar counter-rotating turbines are likely to be analogous to those of a single turbine operating near a free surface. Using a RANS-embedded blade element actuator disc approach, Schluntz and Willden [31] and Vogel and Willden [19] found that the mean C_P and C_T increase as the rotor spacing decreases, in studies of an infinitely long fence and a four-turbine co-planar array, respectively. Their results are consistent with the findings of Schluntz [26], who employed the AL method to model infinite and partial array fences. Despite the unsteady discrete blade representation of the AL method used by Schluntz, no analysis of the blade loading was presented.

Similar observations are reported in separate experimental studies using the same pair of 1.2 m diameter turbines [29, 30]. McNaughton et al. (2022) [29] found that, when arranged side-by-side with a tip spacing of $0.25D$, the turbines' power and thrust coefficients exceed those of a single isolated turbine by 10.8% and 5.2%, respectively, after accounting for differences in the global blockage ratio. Constructive interference between the closely spaced rotors increased the mean blade loads, and the RBMs in the edgewise and flapwise directions peaked as the blades passed the neighbouring turbine. A later study by McNaughton et al. (2023) [30] evaluated the effect of inter-turbine spacing on a quasi-four-turbine array, using the same two 1.2 m diameter turbines and treating the towing tank wall as a symmetry plane. Reducing the inter-turbine spacing from $1.5D$ to $0.25D$ increased the mean power coefficient by 1.4%. The quasi-inboard turbine contributed more to the performance uplift than the outboard turbine, experiencing higher blade loads and producing more power as a result of the lateral flow constraint on both sides of the rotor. Blade loads peaked as they passed a neighbouring turbine or boundary, and a phase shift was observed. The edgewise RBM peaks lagged the horizontal position, at which there was closest proximity to the neighbouring turbine or wall, while the flapwise RBM peaks occurred ahead of the same horizontal position [30].

The above cited studies demonstrate how the rotor performance of TSTs can be influenced by flow constriction effects unrelated to the global blockage ratio. However, there have been limited investigations of the azimuthal load variations caused by local flow passage anisotropy; see for example [30]. Further, many of these studies had limited access to the detailed flow field data required to explain the observed load variations due to the nature of the experimental setup.

In this study, a single TST rotor is simulated using the AL method embedded in a RANS solver with varying tip clearance to the free surface to understand the driving mechanisms behind changes in the performance and loading distributions associated with near-boundary operation. The

surface is first assumed to behave as a rigid lid, before comparing the results to those obtained from multi-phase simulations which capture the turbine's interaction with a deformable free surface. The intention is to quantify the magnitude of turbine-induced deformations on the free surface, and to evaluate the appropriateness of the commonly-used rigid lid assumption. The investigation replicates the experimental conditions of the SOUTTBP, with a 1.6 m rotor simulated in a computational domain of equivalent dimensions to the towing tank at the QinetiQ Haslar facility in which the turbine was tested experimentally [67]. The discrete blade representation and unsteady nature of the AL method allows investigation of the spanwise load distributions and local flow parameters at different azimuthal positions.

6.2 Methodology

6.2.1 Overview

The impact of free surface proximity on tidal stream turbines is investigated by numerical simulation at a range of tip clearances and tip-speed ratios close to the optimal operating point. A single rotor is modelled using the actuator line method to capture the time-averaged performance and the unsteady components of force and flow velocity encountered as the blades rotate. The tip clearance is varied about the position used in the SOUTTBP experiments, and the results are analysed relative to those obtained from a rotor simulated in the centre of the domain.

At each position in the water column, the operating point which yields the maximum power coefficient is found using an iterative method described by Ettema [106]. Three initial tip-speed ratios are modelled around the experimentally predicted optimal value and a quadratic curve is fitted to the C_P-λ data points. The curve is used to predict the maximum power coefficient ($C_P{}^*$) and its corresponding λ, at which a new simulation is performed. After each iteration, a new curve is fitted to the three data points of highest C_P in the enlarged data set, and the process is repeated until the simulated $C_P{}^*$ differs from the predicted value by less than 0.01%. At this point, the predicted λ for maximum C_P is adopted as the optimal and denoted λ^*.

Two options for modelling the free surface are compared to examine the importance of capturing its deformation. Firstly, data are gathered across a sweep of operating points using single-phase CFD simulations, neglecting any deformations by assuming the surface to be a rigid lid. Secondly, the same operating conditions are repeated using multi-phase simulation techniques to capture the position of the deforming free surface at the expense of reduced numerical stability and increased computational cost.

6.2.2 Blade representation method

The rotor blades are modelled virtually in the flow field using the in-house implementation of the AL method described in Chapter 5 to provide an unsteady, discrete blade representation without the need to resolve their geometry in the mesh.

The hydrofoil coefficient data tables were supplied by the organisers of the SOUTTBP, and were generated using wall-resolved 2D RANS simulations with the k-ω SST turbulence closure [66]. The hydrofoil data tabulates the lift and drag coefficients under steady flow conditions, hence, unsteady hydrofoil dynamics are not accounted for in the model. Despite the discrete blade representation, the use of 2D hydrofoil data and the omission of spanwise flow components and pressure gradients in the blade element force calculation implicitly assumes two-dimensional flow behaviour. Three-dimensional flow effects in the vicinity of the blade tips are not well captured without the use of spanwise loading corrections.

The rotor performance coefficients predicted by the in-house AL implementation with the Wimshurst-Willden tip correction [91] and Shen et al. tip correction [72] are compared against the experimental results of the SOUTTBP in [38]. When the nacelle is resolved in the mesh, as opposed to the use of an in-house immersed boundary nacelle representation, Edwards et al. [38] find close agreement in the C_T predicted by the AL method and the experimental results, with a mean error of less than 1% when either tip correction was applied. The choice of tip correction had a more significant impact on the simulated C_P, and greater variation was observed between the AL predictions and the experimental results in both cases. Compared to the experimental results, the in-house AL implementation with Wimshurst-Wilden tip correction overpredicted the power coefficient by an average of 5%, while the mean overprediction was 13% with the Shen et al. correction. In this study, the Wimshurst-Willden tip correction is applied, and was chosen over the correction factor proposed by Shen et al. as it was found to yield results which more closely matched the experimental results of the SOUTTBP [38, 72, 91].

6.2.3 Numerical methods

The AL method is embedded in a flow field modelled using the unsteady RANS method with the k-ω SST turbulence model. Simulations are performed in OpenFOAM-v2006 with solvers which utilise the PIMPLE algorithm to solve the RANS equations. The pimpleFOAM solver is used for the single-phase flow cases, while the interIsoFOAM solver is used for the multi-phase cases. InterIsoFOAM is similar to interFOAM in that it utilises the VOF approach to model the interface between different phases, however, the interface is sharply reconstructed using the isoAdvector scheme. The free surface between the water and air in this study is a continuous-continuous phase

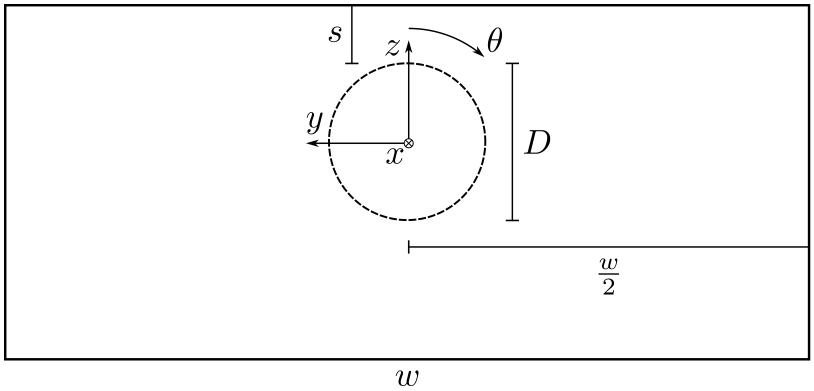


Figure 6.1: The computational domain viewed from upstream of the rotor plane, i.e. the flow direction (positive x) is into the page. Key dimensions and coordinate systems are shown. The turbine rotates clockwise in the positive θ direction and its circumference is represented as a dashed line.

interaction with a discrete interface, suitable for modelling with the VOF approach.

During each iteration of the flow solver, the AL method forces are calculated using information from the previous iteration's flow field data, and imposed as a source term in the momentum equation. To ensure a smooth application of the rotor force to the flow, the timestep condition $\Delta s/\Delta x \leq 1$ is enforced throughout this study. In the single-phase simulations, the timestep size was adjusted for each rotational speed such that $\Delta s/\Delta x$ was approximately equal to, but always less than 1.

The numerical stability of the multi-phase simulations proved to be a challenge in this study. To address this, the modelling software was allowed to reduce the timestep below that required for $\Delta s/\Delta x \leq 1$ if required to maintain a CFL < 1 in the flow field of the multi-phase simulations. The default timestep was the same as that in the equivalent single-phase case. In addition, an under-relaxation factor of 0.8 was applied to the field variables to limit their change from one iteration to the next. This was necessary for stability in certain cases, but is noted as a limitation of the method as the rotor performance was affected. A small number of cases across the operational range could be solved without under-relaxation, so were used as a point of comparison to estimate its influence. Implementing this degree of under-relaxation was found to increase the time-averaged power and thrust coefficients by an average of 0.45% and 0.16%, respectively. To mitigate the impact on fair comparison between the results, the under-relaxation factor was applied uniformly to all multi-phase simulations.

6.2.4 Computational domain

To allow the comparison between rigid lid and deformable surface simulations to be as direct as possible, only the minimum necessary changes in computational setup are made between the

modelling approaches. This section first outlines the setup used for the rigid lid modelling, followed by the modifications made for the more complex multi-phase simulations. Unless otherwise stated, the setup between the two methodologies remains the same.

An illustration of the computational domain used for the rigid lid simulations is shown in Figure 6.1, with annotations showing the coordinate systems and key dimension definitions. The domain has a rectangular cross section of width $7.625D$ in the cross-stream (y) direction, and height $3.375D$ in the vertical (z) direction equivalent to the water depth. The origin of the coordinate system is placed at the rotor's centre for all instances of tip clearance, and the streamwise direction aligns with the positive x direction. The computational domain is 48 m long in the x direction, with the rotor plane being located at a distance of $10D$ from the inlet and $20D$ from the outlet. Blade rotation is in the positive θ direction: clockwise when viewed from upstream. The tip clearance (s) describes the position of the rotor in the water column, defined as the vertical distance between the tip of a blade in the top dead centre position and the free surface, and tests are carried out at non-dimensional tip clearances of $s/D = 1.188$ (mid-depth), 0.712, 0.222 and 0.063.

The meshes used in this study are structured grids of octree type generated using OpenFOAM's snappyHexMesh utility. The meshes contain primarily hexahedral elements with some polyhedral elements where the cells automatically conform to the surface of the nacelle. Mesh refinement is achieved within specified regions by successively halving the size of elements in each dimension, once for each refinement level. A cylindrical refinement region of diameter $1.25D$ and streamwise dimension $0.25D$ is centred around the origin to achieve cuboidal cells at the rotor plane of sufficiently small dimension (Δx) to satisfy the stability constraint $N_\epsilon = \epsilon/\Delta x \geq 2$ [63, 92]. The mesh is also refined in the vicinity of the nacelle surface to achieve a y^+ value of ~ 95, suitable for the use of wall functions. Finally, refinement zones are placed in the near wake region to ensure a progressive transition in cell size from the fine near-rotor resolution to the coarser background mesh, and to capture flow features where the field variable gradients, wake expansion and fluid shear effects are expected to be significant.

The vertical and bottom surfaces of the domain are modelled as inviscid walls using the slip boundary condition. This mimics the experimental testing in the towing tank in which the water has no velocity relative to the outer walls. In the rigid lid modelling, the slip condition is also applied to the upper boundary as the free surface is assumed to behave as a non-deformable symmetry plane. The inlet boundary is prescribed a fixed uniform velocity of 0.899 m/s with zero pressure gradient in the streamwise direction, while the outlet is defined to have fixed uniform pressure with a zero-gradient condition on velocity. An isotropic turbulence of 4% intensity is applied to the inlet flow, which decays to $\sim 3\%$ at the rotor plane to replicate the flow conditions of the *Elevated*

Turbulence cases in the SOUTTBP experiments [67].

In the multi-phase simulations, the computational domain is extended by $0.625D$ in the z direction to model a portion of the air above the free surface. In these cases, the tip clearance is defined relative to the still water surface position. Additional refinement zones encompass the water-air interface with the finest region having a vertical extent of $0.0375D$ above and below the still water position. To manage computational expense, the finest region of surface refinement is focussed on an area of $10D$ by $5D$ in the x and y directions, placed directly above the turbine where the rate of surface elevation change is expected to be greatest. Further refinement, in the vertical direction only, is applied to all cells in the surface region to achieve a $x:y:z$ cell aspect ratio of $4:4:1$. The resultant cell height around the surface above the rotor plane is $2.125 \times 10^{-3}D$ (3.4 mm), sufficient to capture the small deformations which are expected. The mesh adaptions implemented to model the free surface position increase the cell count from 12 million to 46 million, significantly increasing the computational cost.

For the multi-phase simulations, the inlet boundary remains a fixed uniform velocity condition. However, the pressure gradient is set to achieve the mass flux prescribed by the velocity condition and the inlet fluid height condition, which is fixed at the still water level. At the outlet, the pressure is assigned a zero-gradient condition while the free surface height is allowed to vary in the cross-stream direction. However, the mean velocity of the water phase is fixed at a value equal to the inlet flow velocity, enforcing a mean surface elevation equal to that at the inlet.

The simulated tidal channel is a subcritical free surface flow, hence energy extraction by the turbine is expected to yield a decrease in water depth. Removing energy from the flow results in a decrease in static head and an acceleration of the bulk flow. It is recognised that the imposed boundary conditions enforce a non-physical energy conservation across the domain, restricting the simulation from producing such a drop in surface elevation. However, *a priori* estimates anticipate the energy extraction, and associated change in surface elevation, to be negligible relative to that in the bulk flow. In practice, the numerical error is pushed upstream in these simulations, resulting in a surface height greater than z_0 upstream of the turbine, and a small local numerical oscillation in surface height towards the inlet that corrects for the energy extraction across the system. This simplification is a limitation of the numerical setup, but the error manifests far upstream of the turbine and should have negligible impact on the rotor performance metrics.

6.2.5 Uncertainty estimation for deterministically varying quantities

As will be demonstrated, the variations in the blade forces, relative flow velocity and overall rotor performance associated with changes in s/D are small, hence, it is important to quantify

the uncertainty in the data. Additionally, the anisotropy of the local flow passage introduces regular-frequency oscillations to the data, the amplitude of which can be significantly larger than the numerical noise. Therefore, these deterministic-frequency oscillations must be excluded in the uncertainty estimation.

Data are typically presented in this work as time-averaged, or phase-averaged quantities to reduce the uncertainty associated with cycle-to-cycle variations. An overbar is used to signify that a quantity is time-averaged ($\bar{.}$), while phase-averaged quantities are enclosed in angled brackets ($\langle . \rangle$). An averaging window of length equal to 10 rotational periods is used throughout, with time-averaged quantities being calculated as the mean of all samples within the window. For phase-averaged quantities, the samples within the averaging window are divided into phase bins of width 2° according to the position of the rotor, and the mean is calculated within each bin.

To eliminate the boundary-induced deterministic oscillation from the uncertainty estimation, the confidence interval of unprocessed time-series data is calculated at each phase of the rotation from the standard deviation of the values contained within the corresponding bin, denoted σ^{Φ}. Similarly, the uncertainty associated with phase-averaged data is calculated from the standard error within each phase bin, SE^{Φ}. Finally, a global standard error (SE) is defined to estimate the uncertainty in time-averaged values, calculated as the mean of SE^{Φ} across the full cycle. SE and SE^{Φ} are defined in Equation 6.1, where N_s is the number of samples in each bin, and N_B denotes the total number of bins. Assuming the data to be normally distributed, 95% confidence intervals are approximated for unprocessed, phase-averaged and time-averaged values as $\pm 2\sigma^{\Phi}$, $\pm 2SE^{\Phi}$ and $\pm 2SE$ respectively.

$$SE = \frac{1}{N_B} \sum_{b=1}^{N_B} SE^{\Phi} = \frac{1}{N_B} \sum_{b=1}^{N_B} \frac{\sigma^{\Phi}}{\sqrt{N_s}} \tag{6.1}$$

6.3 Operation of tidal stream turbines in close proximity to a rigid boundary

6.3.1 Rotor performance

The performance of the rotor at each tip clearance is analysed in terms of the time-averaged power ($\bar{C_P}$) and thrust ($\bar{C_T}$) coefficients. The power and thrust values used to calculate the coefficients are time-averaged over the final 10 revolutions of the simulated period, once the cycle-to-cycle residuals for all cases are less than 0.005% and 0.0025%, respectively. The residuals are defined as the relative change in time-averaged performance coefficient, calculated over successive windows each spanning one rotor period. The results are shown in Figure 6.2 which presents the three initial operating points, and the optimal operating point discovered using the iterative method described in Section 6.2.1. The iterative method converged after just one iteration for all tip clearance cases.

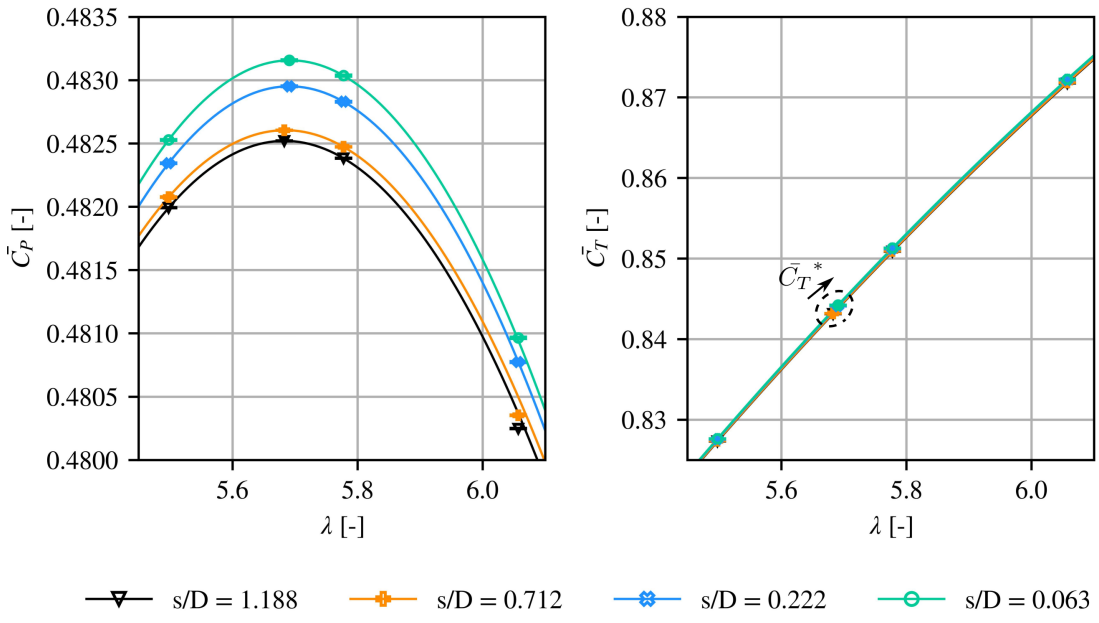


Figure 6.2: Rigid lid modelling: Performance curves of time-averaged power and thrust coefficient with λ for varying tip clearances. The three initial operating points at $\lambda = 5.50$, 5.78 and 6.06 are shown (hollow markers) as well as the discovered optimal point of $\bar{C_P}^*$ at λ^* (filled markers). Vertical bars (which are consistently within the vertical extent of the data point markers) show an estimation of the 95% confidence interval, taken to be twice the average of the standard error calculated for each phase bin of the last 10 revolutions.

Although the impact is small, decreasing the tip clearance increases both $\bar{C_P}$ and $\bar{C_T}$ at each of the simulated operating points. As summarised in Table 6.1, the lowest tip clearance of $s/D = 0.063$ yields the largest increase in $\bar{C_P}^*$ and $\bar{C_T}^*$ of 0.13% relative to their mid-depth values. Alongside this, the optimal operating point moves to a slightly higher tip-speed ratio as the rotor is positioned closer to the boundary.

The results in Figure 6.2 support the hypothesis that the nearby boundary acts to constrict the bypass flow in the adjacent region as the trends are consistent with those expected from prior understanding of blockage effects. As discussed by Vogel and Willden [19], constraining the bypass flow causes it to accelerate, reducing its static pressure. Assuming that the static pressure of the core and bypass flows equalise at some downstream position, the accelerated bypass flow results in an increase in the static pressure drop across the rotor plane, increasing the generated thrust at a given operating condition. In addition, constraining the bypass region inhibits the expansion of the core flow streamtube as it passes through the rotor, allowing λ^* to increase to a point of higher thrust without choking the flow through the rotor plane.

The vertical bars in Figure 6.2 represent $\pm 2SE$ as an estimation of the 95% confidence interval. Owing to the stringency of the convergence criteria, the uncertainties are negligible relative to the changes induced by s/D giving confidence in the statistical significance of the observed trends.

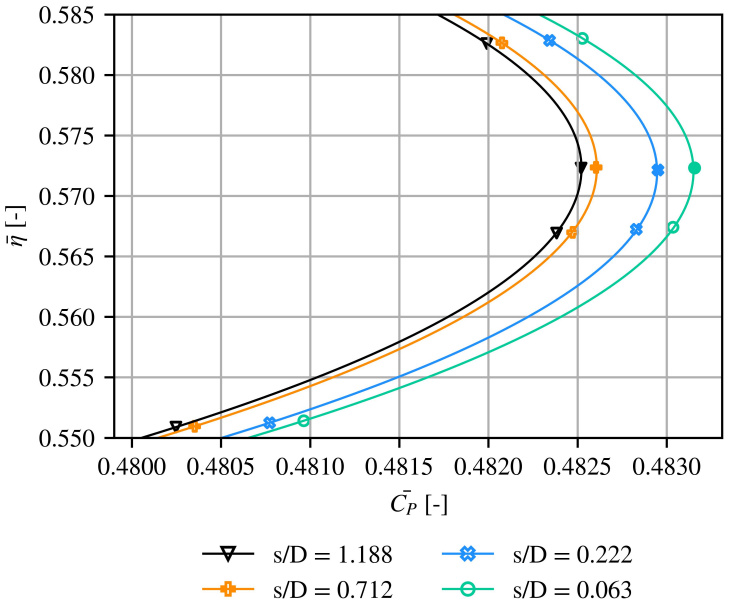


Figure 6.3: Rigid lid modelling: The impact of boundary proximity on the time-averaged basin efficiency ($\bar{\eta} = \bar{C_P}/\bar{C_T}$). Hollow markers denote the three initial operating points while the optimal points are shown as filled markers. The trendlines are a quadratic fit between all points.

An alternative performance metric is the basin efficiency (η) which quantifies resource utilisation as the ratio C_P/C_T. This represents the ratio of energy extracted by the turbine to the total energy removed from the flow, with the latter including the energy lost in remixing the core and bypass flows downstream of the turbine.

Table 6.1: Rigid lid modelling: Rotor performance, $\bar{C_P}$, $\bar{C_T}$ and $\bar{\eta}$, at the optimal operating point (tip-speed ratio). Simulated $\bar{C_P^*}$ and $\bar{C_T^*}$ are normalised by their values at $s/D = 1.188$ (mid-depth).

s/D	λ^*	$\bar{C_P}^*/\bar{C_{P_{md}}^*}$	$\bar{C_T}^*/\bar{C_{T_{md}}^*}$	$\bar{\eta}^*$
0.063	5.6909	1.0013	1.0013	0.5723
0.222	5.6909	1.0009	1.0012	0.5721
0.712	5.6828	1.0002	1.0001	0.5724
1.188	5.6828	1.0000	1.0000	0.5723

Figure 6.3 presents the time-averaged basin efficiency of the cases shown in Figure 6.2 plotted against $\bar{C_P}$. For all tip clearances, following the curves in the direction of decreasing $\bar{\eta}$ corresponds to increasing tip-speed ratio and $\bar{C_T}$. Increasing the rotor's thrust increases the velocity difference between the core and bypass flows, increasing the energy lost in their remixing. Decreasing the tip clearance shifts the performance curves to the right, indicating that more power can be extracted for a given basin efficiency. As noted in Table 6.1, the basin efficiency at the point of maximum power coefficient ($\bar{\eta}^*$) is independent of s/D. Additionally, the data over this narrow range of

tip-speed ratios indicates that when operating at $\lambda < \lambda^*$, a target off-peak $\bar{C_P}$ can be achieved at a higher basin efficiency by decreasing the tip clearance. In Figure 6.3, this corresponds to a vertical shift across the family of curves, to a point of lower λ and $\bar{C_T}$ where the same power is extracted at lower detriment to the tidal resource.

6.3.2 Azimuthal blade loading variations

This section presents the phase-averaged blade loads on polar plots to analyse their dependence on azimuthal position. As is true of all figures plotted on polar axes in this chapter, the angular coordinate represents the azimuthal position in the y-z plane as viewed from upstream of the rotor. Hence, the rotor rotates clockwise in the positive θ direction.

The data are phase-averaged within bins of width 2° over the last 10 revolutions of each simulation time series. At each azimuthal position of the polar line plots, a shaded region of $\pm SE^{\Phi}$ is plotted as a 95% confidence interval of the mean within each phase bin.

The time history of spanwise-varying sectional blade forces are used to derive the root bending moments and mapped to a spatial position. The RBM in the edgewise direction (RBM_θ) is similar to the torque generated by an individual blade, with moments calculated about the hub connection rather than the rotor's axis, while the flapwise RBM (RBM_x) is the moment due to forces in the thrust direction.

Figure 6.4 shows the azimuthal variation of phase-averaged RBMs at $\lambda = 5.78$. The characteristic shape of the load variations did not vary significantly with λ within the scope of this study, hence, the subsequent analysis focuses on a single rotational speed for clarity. The radial axis is the RBM normalised by the azimuthal mean across all bins of the phase-averaged result at mid-depth, $\frac{1}{N_B}\sum_{b=1}^{N_B}\langle RBM_{md}\rangle$, where the subscript $_{md}$ is used to denote the case of $s/D = 1.188$. The shaded confidence interval is plotted, however, the uncertainty magnitude is too small to be visible, with a maximum value of 3.3×10^{-4} across all cases and azimuthal positions.

In accordance with the $\bar{C_P}$ and $\bar{C_T}$ results of Section 6.3.1, decreasing the tip clearance increases the azimuthal mean of the RBMs in both directions. However, the overall increase in blade loading is not uniformly distributed around the azimuth, with the RBMs even decreasing with s/D at certain azimuthal positions. As s/D is decreased, the range of the load variation around the azimuth increases. Interestingly, the azimuthal positions of maxima and minima in the edgewise and flapwise RBMs are not in phase with each other, and do not occur when the blade is either exactly closest to, or furthest away from the free surface boundary.

In the edgewise direction, the RBM is generally enhanced in the near-boundary half of the rotation, but peaks at a position which lags top dead centre. At $s/D = 0.063$, the peak

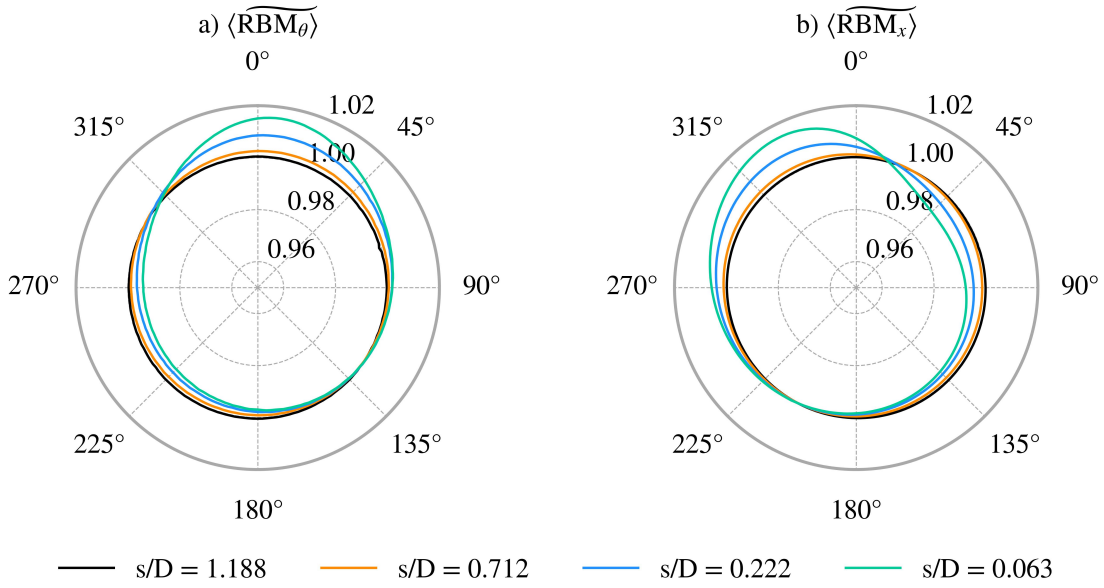


Figure 6.4: Rigid lid modelling: Phase-averaged root bending moment of an individual blade in the (a) edgewise and (b) flapwise directions at $\lambda = 5.78$. The free surface is directly above such that the point of closest proximity to the free surface is at 0°. The radial axis is normalised by the azimuthal mean of the phase-averaged RBM at $s/D = 1.188$ (mid-depth), $\frac{1}{N_B}\sum_{b=1}^{N_B}\langle RBM_{md}\rangle$. This normalisation is denoted by $\widetilde{(\cdot)}$. Although not visible due to its small magnitude, a shaded region of $\pm 2SE^{\Phi}$ is plotted around each line as a 95% confidence interval.

normalised $\langle \text{RBM}_\theta \rangle$ reaches a value of 1.016 at $\theta = 8°$. Boundary influence alleviates the load in the edgewise direction during the lower left quadrant of rotation. The minimum normalised $\langle \text{RBM}_\theta \rangle$ at $s/D = 0.063$ occurs at $\theta = 254°$ with a value of 0.994.

Operating near the boundary only increases $\langle \text{RBM}_x \rangle$ on the upstroke, as the top dead centre (TDC) position is approached. Boundary proximity induces a degree of asymmetry about the vertical axis which bisects the rotor plane; $\langle \text{RBM}_x \rangle$ is increased ahead of TDC but becomes less than that at mid-depth on the downstroke following TDC. However, the unity crossing point lags TDC and the minimum has a smaller amplitude than the maximum. At $s/D = 0.063$, the peak has a normalised value of 1.015 at $\theta = 330°$. The minimum normalised value of 0.991 occurs at $\theta = 58°$.

To further investigate the origin of the observed RBM distributions, Figures 6.5 and 6.6 show contours of the phase-averaged blade sectional force ($\langle f \rangle$) variations in the axial and tangential directions. The polar coordinates represent the rotor swept area with the radial axis denoting the radial position along the blade span normalised by the tip radius (r/R). Blade sectional forces generally increase from root to tip, owing to the increase in relative velocity magnitude, up to a point where tip losses begin to take effect. To highlight the azimuthal variations, the forces at each radial station are plotted relative to the azimuthal mean of the phase-averaged load at this radius.

Figures 6.5 and 6.6 concur with the RBM observations in that there is no significant azimuthal

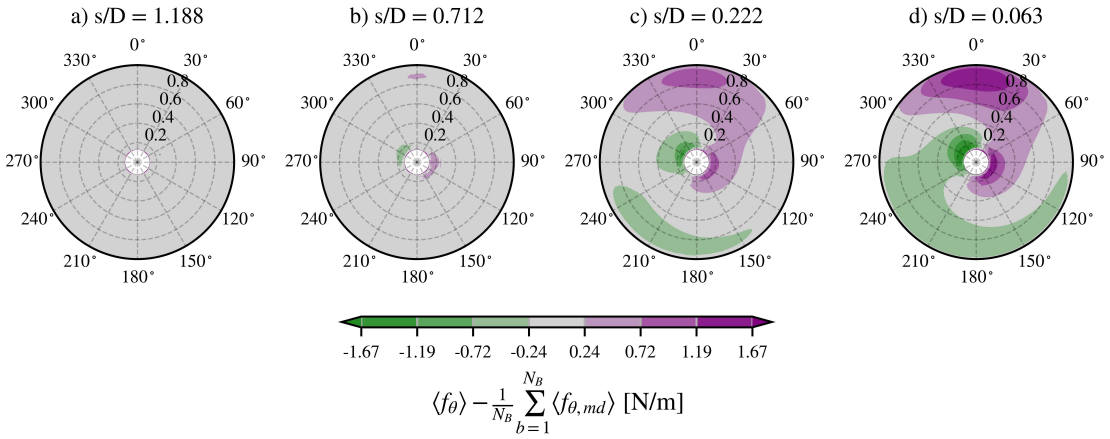


Figure 6.5: Rigid lid modelling: Contours showing the phase-averaged tangential sectional force component across the rotor plane at $\lambda = 5.78$, plotted relative to the azimuthal mean of the phase-averaged sectional force at $s/D = 1.188$ (mid-depth), calculated individually for each radial position. The radial axis is $r/R \in [0, 1]$ while the angular coordinate is the azimuthal position.

load variation at mid-depth, while increasingly greater azimuthal load variations occur as the boundary is approached from $s/D = 0.712 \rightarrow 0.063$. The RBMs are influenced most by outboard sections of the blade where the forces and moment arm are largest, and it is in these regions where the blade sectional forces are most affected by the boundary.

For the closest spacings, the loading peak in the tangential direction (Figure 6.5) close to the tip, in the region $r/R \in [0.8, 1]$, is roughly centred around TDC. However, the regions of maximum loading for sections in $r/R \in [0.3, 0.8]$ show a bias to the upper right quadrant, consistent with the phase lag observed in the $\langle \mathrm{RBM}_\theta \rangle$ peak.

The green regions of load alleviation have a less well defined minimum, with the relative $\langle f_\theta \rangle$ generally being negative in the lower half of the rotation close to the blade tip. However, the proportion of the blade with negative relative $\langle f_\theta \rangle$ grows in the lower left quadrant, leading to an $\langle \mathrm{RBM}_\theta \rangle$ minimum in this region. The magnitude of the largest relative $\langle f_\theta \rangle$ peak exceeds that of the lowest trough by close to four times at $s/D = 0.063$.

The blade sectional force variations in the axial direction also correlate well with their associated RBM. In Figure 6.6, large values of relative $\langle f_x \rangle$ are concentrated in the outboard sections of the blade, with no appreciable variation near the hub. On the outboard sections of the blade, the axial force peaks in the upper left quadrant while its minimum value occurs in the upper right quadrant. Similar to the $\langle \mathrm{RBM}_x \rangle$ distribution (Figure 6.4), the $\langle f_x \rangle$ variations are approximately antisymmetric in the upper half of the rotation, about an axis formed between $\theta = 20°$ and $\theta = 200°$.

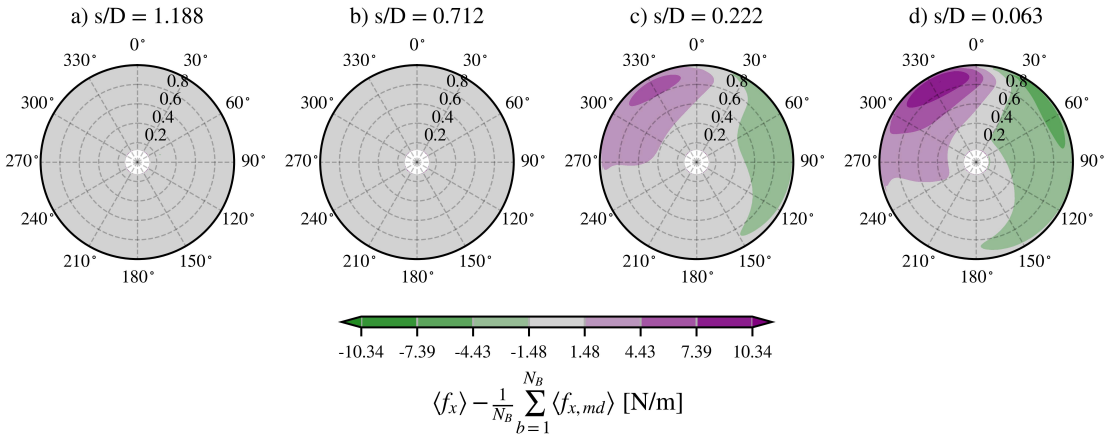


Figure 6.6: Rigid lid modelling: Contours showing the phase-averaged axial sectional force component across the rotor plane at $\lambda = 5.78$, plotted relative to the azimuthal mean of the phase-averaged sectional force at $s/D = 1.188$ (mid-depth), calculated individually for each radial position. The radial axis is $r/R \in [0, 1]$ while the angular coordinate axis is the azimuthal position.

6.3.3 Near-boundary flow effects

Figure 6.7 shows contours of the time-averaged tangential velocity ($\bar{U_\theta}$), defined to be positive in the anticlockwise direction, opposite to turbine rotation. The Cartesian contour plots are in the same reference frame as those plotted in polar coordinates: in the y-z plane viewed from upstream of the turbine such that the turbine rotates clockwise. The first column presents the flow field at a station $0.05D$ upstream of the rotor plane; close to the rotor, but sufficiently far upstream that the torque-induced whirl velocity is not seen. The second column shows data at the rotor plane, and the final column is the result of subtracting the upstream $\bar{U_\theta}$ in the first column from the rotor plane $\bar{U_\theta}$ in the second.

At mid-depth (first row), the flow approaching the turbine expands isotropically and there is no rotational component to the flow upstream of the rotor (see tile (a)). At the rotor plane (tile (b)), the tangential velocity is observed to be constant around the azimuth, indicative of the torque-induced whirl velocity which must be generated to satisfy conservation of angular momentum. Trivially, subtracting (a) from (b) returns this same torque-induced whirl velocity as $\bar{U_\theta}$ is approximately zero everywhere in tile (a).

The second row of Figure 6.7 shows data taken from the flow field of a turbine operating near the boundary at $s/D = 0.063$. The flow upstream of the turbine (tile (d)) now has tangential components of equal magnitude but opposite sign in the upper left and right quadrants. As a result, the tangential velocity at the rotor plane becomes azimuthally non-uniform (see tile (e)). In the upper left quadrant, the tangential component of the incoming flow acts in addition to the torque-induced whirl velocity, increasing $\bar{U_\theta}$ over the mid-depth case. However, in the upper right

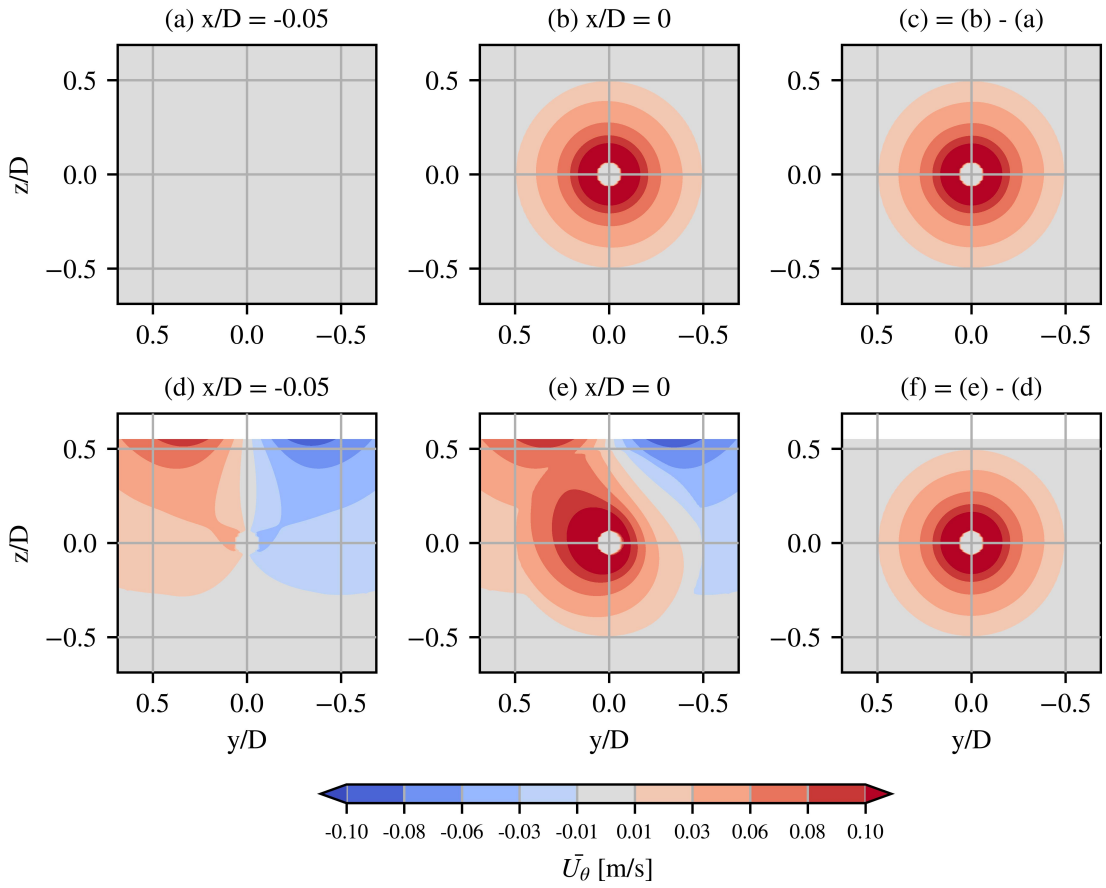


Figure 6.7: Rigid lid modelling: Contours of the time-averaged tangential velocity component extracted from the flow field at stations $0.05D$ upstream of the rotor plane ((a) and (d)), and at the rotor plane ((b) and (e)). Also shown is the subtraction of the upstream $\bar{U}_\theta$ field from that measured at the rotor plane ((c) and (f)). The first row ((a) to (c)) shows results of a turbine operating at mid-depth ($s/D = 1.188$), while the second row ((d) to (f)) shows results from a turbine near the boundary at $s/D = 0.063$. All plots are shown at $\lambda = 5.78$ and $\bar{U}_\theta$ is defined to be positive in the anticlockwise direction. White space at the top of the contours at $s/D = 0.063$ are due to the viewing window extending outside the boundary of the computational domain, so indicates the position of the rigid lid boundary used here to model the free surface.

quadrant the incoming flow has negative tangential velocity which opposes the torque-induced whirl velocity. This results in a decreased $\bar{U}_\theta$ in this region of the rotor plane (tile (e)), even becoming negative close to the tip at some azimuthal positions in the upper right quadrant.

Tile (f) confirms that the non-uniform $\bar{U}_\theta$ observed in tile (b) is a direct superposition of the incoming tangential velocity field with the torque-induced whirl velocity. When the upstream rotational component is subtracted from the rotor plane flow field, a constant torque-induced whirl velocity is returned.

Figure 6.8 demonstrates that the non-uniformity of the rotor plane flow field's $\bar{U}_\theta$ is identified in the sampled velocity vector, and shows that the antisymmetric effect intensifies as the rotor operates in closer proximity to the boundary. The azimuthal variation is negligible at mid-depth

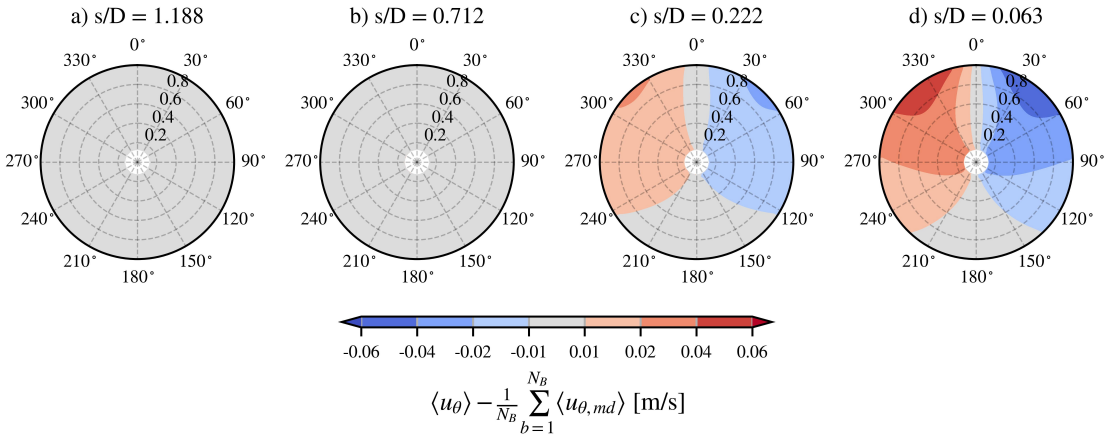


Figure 6.8: Rigid lid modelling: Contours showing the phase-averaged tangential velocity component, defined to be positive in the anticlockwise direction, as sampled by the AL method at each position on the rotor plane at $\lambda = 5.78$. The velocity is shown relative to the azimuthal mean of the phase-averaged velocity at $s/D = 1.188$ (mid-depth), calculated individually for each radial position. The radial axis is $r/R \in [0, 1]$ while the angular coordinate is the azimuthal position.

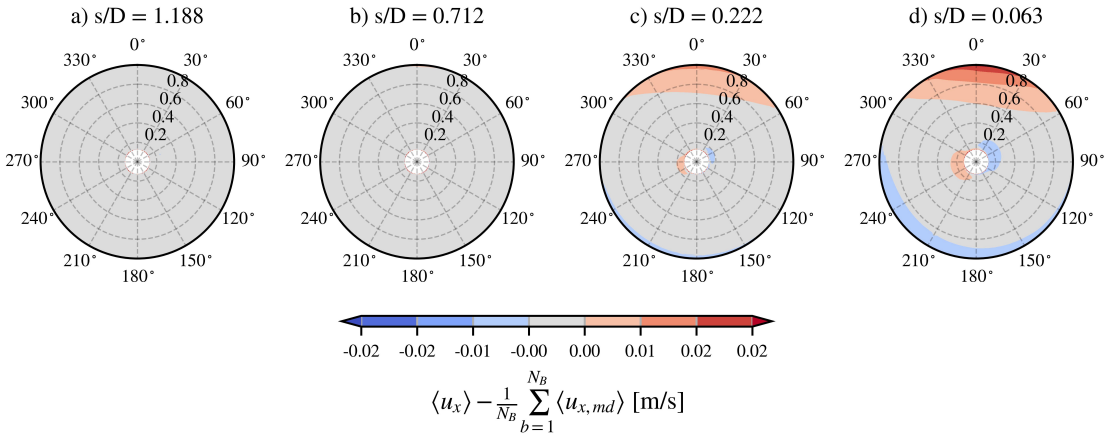


Figure 6.9: Rigid lid modelling: Contours showing the phase-averaged axial velocity component as sampled by the AL method at each position on the rotor plane at $\lambda = 5.78$. The velocity is shown relative to the azimuthal mean of the phase-averaged velocity at $s/D = 1.188$ (mid-depth), calculated individually for each radial position. The radial axis is $r/R \in [0, 1]$ while the angular coordinate is the azimuthal position.

and $s/D = 0.712$, but as the tip clearance decreases the variation of $\langle u_\theta \rangle$ increases relative to its azimuthal mean, particularly on the outboard sections of the blade. The approximately azimuthally constant torque-induced component of $\langle u_\theta \rangle$ is removed by plotting its value in a relative sense, hence the distributions exhibit the same symmetry seen in tile (d) of Figure 6.7.

Figure 6.9 supports the proposition that the nearby boundary generates an anisotropic flow constriction effect. The axial component of velocity is azimuthally constant at mid-depth. However, as the boundary is approached, $\langle u_x \rangle$ is increasingly accelerated in the upper region of the rotor plane. The nearby boundary constrains the bypass flow driving greater mass flux through the rotor

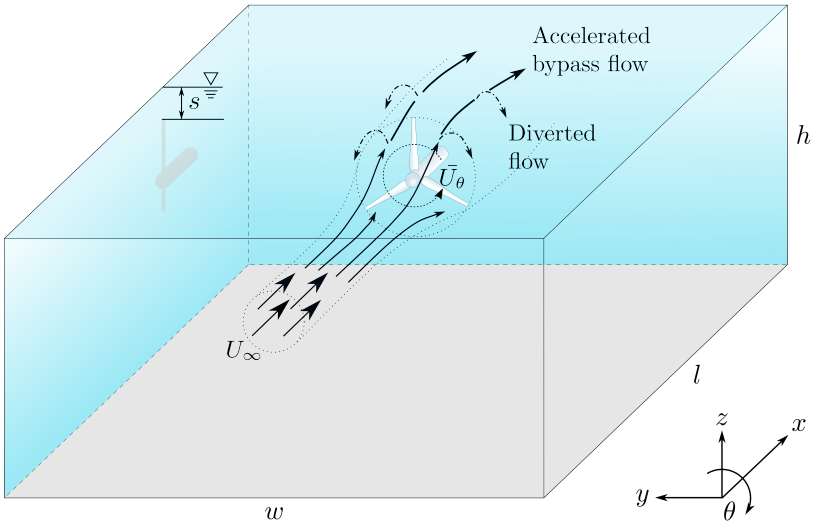


Figure 6.10: An illustration of the flow mechanisms which contribute towards the azimuthally varying flow observed at the rotor plane of turbines operating in close proximity to the free surface. The illustration highlights the expanding streamtube of the incoming flow (solid line), the acceleration of the bypass flow between the rotor and the boundary, the flow component which is laterally diverted by the boundary (dash-dot line) and the torque induced whirl velocity $\bar{U}_\theta$ (dashed line). The turbine is rotating clockwise in the positive θ direction.

plane increasing $\langle u_x \rangle$ in the adjacent region near top dead centre. There is a slight bias towards the downstroke such that the region of higher $\langle u_x \rangle$ has greater extent on the right hand side, likely due to the thrust force being lower during this period of the rotation. As shown in Figure 6.6, the blade sectional forces in the axial direction decrease in the upper right quadrant, thereby reducing the resistance to streamwise flow in the quadrant.

As the incoming flow approaches the turbine, it decelerates in response to the rotor's thrust. The core flow streamtube expands inviscidly and the bypass flow is pushed around the outside of the rotor. For both core and bypass flows, the flow acquires a radial velocity component as it approaches the turbine. For a turbine operating in unbounded flow, or where the domain boundaries are at constant radius from the rotor centre, the resistance to expansion of the incoming flow is constant around the azimuth. Therefore, the core flow streamtube and the diverting bypass flow expand isotropically in the radial direction upstream of the turbine.

When the rotor operates near an impenetrable boundary, the radial expansion of the incoming flow is restricted in the adjacent region. Dash-dot lines in Figure 6.10 represent the flow which is laterally diverted by the boundary to conserve mass flow as it attempts to expand radially. This flow diversion into the tangential direction results in the incoming flow acquiring a positive (anticlockwise) $\bar{U}_\theta$ in the upper left quadrant, and a negative (clockwise) $\bar{U}_\theta$ in the upper right quadrant just ahead of the rotor plane. It is this mechanism, combined with the streamwise velocity distribution caused by bypass constriction effects, which generates the rotor plane flow conditions

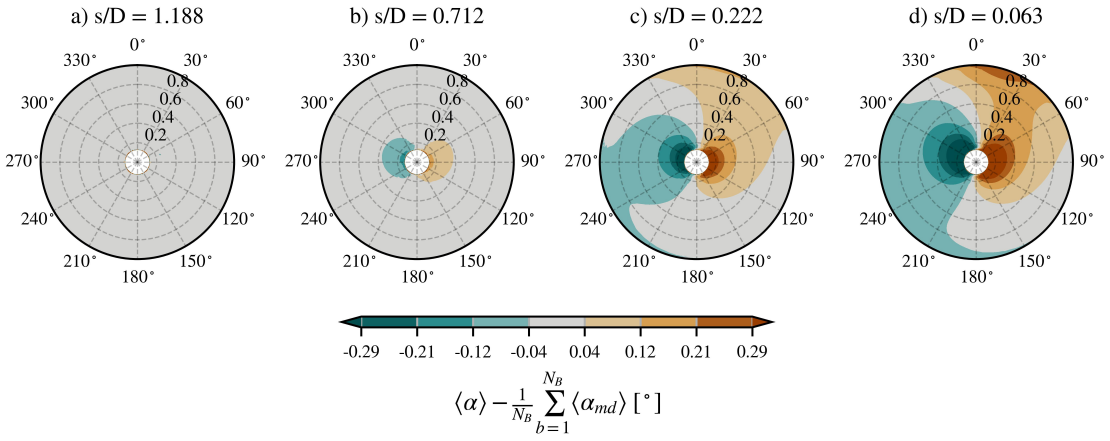


Figure 6.11: Rigid lid modelling: Contours showing the phase-averaged angle of attack as sampled by the AL method at each position on the rotor plane at $\lambda = 5.78$. The angle of attack is shown relative to the azimuthal mean of the phase-averaged angle of attack at $s/D = 1.188$ (mid-depth), calculated individually for each radial position. The radial axis is $r/R \in [0, 1]$ while the angular coordinate is the azimuthal position.

observed in Figures 6.8 and 6.9.

In this study, a fixed pitch turbine is operated at a constant rotational speed. Therefore, the angular velocity and geometric twist at a particular radial location remain unchanged. Hence, the length of the relative velocity vector (V), and its relative inflow angle (ϕ) are affected by u_x and u_θ only. Given that the geometric twist remains fixed, changes in ϕ directly affect the angle of attack (α). Increasing u_x leads to higher values of both V and α, whereas an increase in u_θ raises V but reduces α. In the AL model used in this study, the sectional blade forces are calculated according to the values of V and α, hence, the relative inflow velocity is now studied in terms of these parameters to enable an explanation of the RBM distributions.

Contours of the angle of attack variation are shown in Figure 6.11. The root of the blade is subject to large angle of attack variations, which are largely symmetric about the vertical axis. These variations are visible at $s/D = 0.712$, indicating that a small degree of boundary influence is experienced even at this large tip clearance. The magnitude of angle of attack variation increases as the boundary is approached across the entire span of the blade. Outboard of $r/R = 0.6$, relative $\langle\alpha\rangle$ is positive in the upper right quadrant and negative in the middle and lower left portions of the rotor plane. Close to the tip of the blade, the regions of increased and decreased $\langle\alpha\rangle$ begin earlier in the rotational phase than further inboard, closer to TDC and bottom dead centre (BDC), respectively, resulting in a swirl-like pattern in the observed $\langle\alpha\rangle$.

In the upper right quadrant, the increase in $\langle u_x\rangle$ and the reduction in $\langle u_\theta\rangle$ act constructively to increase $\langle\alpha\rangle$. The relative $\langle u_x\rangle$ variation is greatest at the blade tip which shifts the $\langle\alpha\rangle$ peak closer to TDC, and increases its strength, as $r/R \to 1$.

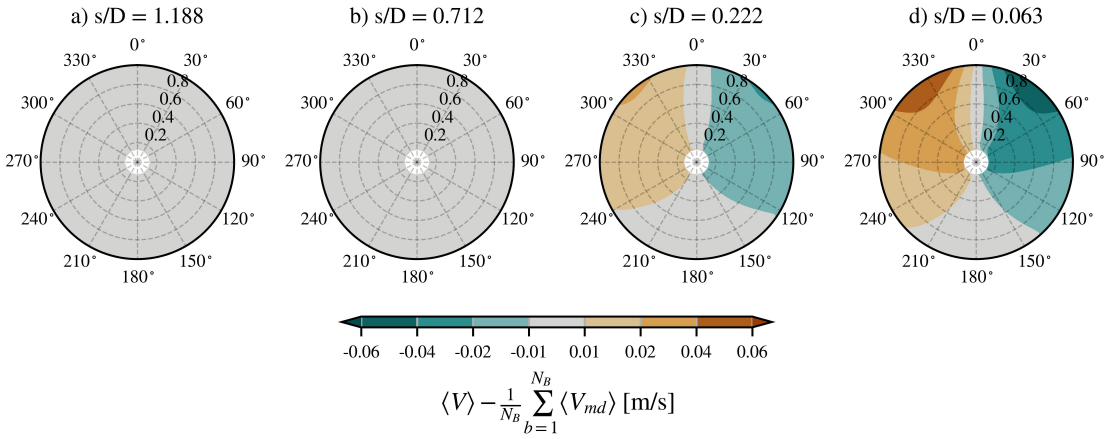


Figure 6.12: Rigid lid modelling: Contours showing the phase-averaged relative velocity magnitude as sampled by the AL method at each position on the rotor plane at $\lambda = 5.78$. The velocity is shown relative to the azimuthal mean of the phase-averaged velocity at $s/D = 1.188$ (mid-depth), calculated individually for each radial position. The radial axis is $r/R \in [0, 1]$ while the angular coordinate is the azimuthal position.

On the left hand side of the rotor plane, the increased $\langle u_\theta \rangle$ decreases the angle of attack. The reduced $\langle u_x \rangle$, which acts to decrease $\langle \alpha \rangle$, close to the tip in the lower left quadrant is responsible for extending the region of lower $\langle \alpha \rangle$ closer to BDC. In the upper left quadrant, the increased $\langle u_x \rangle$ due to bypass acceleration begins to take effect, acting to counter the effect of increased $\langle u_\theta \rangle$. The opposing contributions result in a relatively neutral effect on $\langle \alpha \rangle$.

The azimuthal variations of phase-averaged relative velocity magnitude, shown in Figure 6.12, have similar distributions to those in Figure 6.8 indicating that they are dominated by changes in $\langle u_\theta \rangle$. The variations increase with boundary proximity and the contours are approximately symmetrical about the vertical axis, consistent with the $\langle u_\theta \rangle$ variations in Figure 6.8. In the upper right quadrant, the reduction in $\langle u_\theta \rangle$ is much more significant than the increase in $\langle u_x \rangle$ which results in a negative relative $\langle V \rangle$. Both $\langle u_x \rangle$ and $\langle u_\theta \rangle$ increase in the upper left quadrant, with cumulative effect to give a positive relative $\langle V \rangle$.

6.3.4 Relating boundary proximity impacts on blade loading to the experienced flow conditions

The rotor loads in the AL method are determined by the blade sectional lift and drag (l and d) forces which are calculated using the BE method assuming quasi-steady 2D hydrofoil behaviour. The forces are calculated based on the flow sampled at each collocation point and the local chord length, as detailed in Equations 2.6 and 2.7.

The relationship between the blade sectional force (f) and the experienced relative flow velocity magnitude is clear: the magnitude of f scales with V^2, but V has no impact on its direction (ψ)

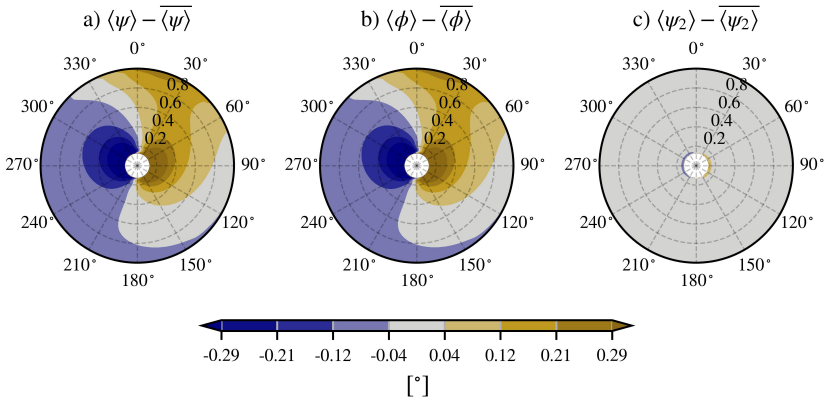


Figure 6.13: Rigid lid modelling: Contours showing the angle of the force vector $\psi = (\alpha + \beta) - \tan^{-1}(C_d/C_l)$ derived from the AL method's phase-averaged forces and sampled flow components at $\lambda = 5.78$. The angle is shown relative to the azimuthal mean at $s/D = 1.188$ (mid-depth), calculated individually for each radial position. The two constituent terms, $\phi = \alpha + \beta$ and $\psi_2 = \tan^{-1}(C_d/C_l)$, are plotted separately. The radial axis is $r/R \in [0, 1]$ while the angular coordinate is the azimuthal position.

(see Figure 2.1 for the definition of ψ) as the lift and drag forces are affected equally. Meanwhile, the angle of the relative flow velocity, here measured by α since the blade pitch remains fixed, can affect both the magnitude and direction of f. The angle of attack determines the lift and drag coefficients which affect the values of l and d. Additionally, α influences ψ through two mechanisms. Firstly in the rotation of the coordinate system by which the lift and drag are defined, and secondly in the variation of the lift-to-drag ratio, C_l/C_d.

The gradient of the hydrofoil's C_l/C_d curve is low around the design angle of attack, hence, small changes in α return only small changes in the C_l/C_d ratio. As a result, changes in angle of attack affect the sectional force angle ψ principally through the rotation of the lift-drag coordinate system, with changes associated to variations in C_l/C_d being insignificant in comparison.

An expression for ψ is given in Equation 6.2, separating the two constituent terms, $\phi = \alpha + \beta$ and $\psi_2 = \tan^{-1}(C_d/C_l)$.

$$\psi = \phi - \psi_2 = (\alpha + \beta) - \tan^{-1}\left(\frac{C_d}{C_l}\right) \tag{6.2}$$

Figure 6.13 shows contours of the phase-averaged ψ, as well as its two constituent terms. The variation in $\langle\phi\rangle$ approximates that of $\langle\psi\rangle$, while $\langle\psi_2\rangle$ exhibits almost no variation. Therefore, the azimuthal variation of the sectional force angle ψ is almost entirely driven by variations in the angle of attack.

At any given local radius, the contribution of a blade element to the flapwise RBM is given by $f\cos(\psi)\delta r\,[r - R_{\text{hub}}]$ while the contribution to the edgewise RBM is $f\sin(\psi)\delta r\,[r - R_{\text{hub}}]$, where R_{hub} is the hub radius and δr is the spanwise length of the blade element. Outboard sections of the blade span, which contribute significantly to the RBMs, were observed to have small ψ.

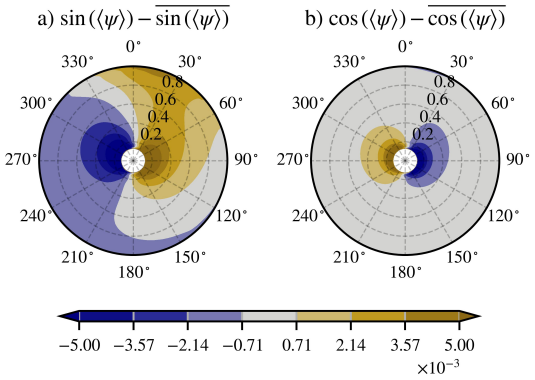


Figure 6.14: Rigid lid modelling: Contours showing the variations of the sine and cosine functions of the phase-averaged angle of the force vector $\langle\psi\rangle$ at $\lambda = 5.78$. The variations are shown relative to the azimuthal mean at $s/D = 1.188$ (mid-depth), calculated individually for each radial position. The radial axis is $r/R \in [0, 1]$ while the angular coordinate is the azimuthal position.

Accordingly, observing the gradients of the sine and cosine functions at small angles, the edgewise force is expected to be more sensitive to changes in ψ than the flapwise force. This is confirmed in Figure 6.14 which shows that the variation in $\sin(\langle\psi\rangle)$ approximates that of $\langle\psi\rangle$, whereas $\cos(\langle\psi\rangle)$ is effectively independent of $\langle\psi\rangle$ on the outboard sections of the blade.

Hence, the RBM distributions observed in Figure 6.4 can now be explained. The flapwise RBM distribution follows that of $\langle V \rangle$ with a peak in the upper left quadrant, and a trough in upper right (Figure 6.12). Similarly, the edgewise forces take influence from the resultant force magnitude, but are also much more sensitive to changes in the resultant force angle. Consequently, the edgewise RBM is increased in the upper left quadrant where $\langle V \rangle$ is greatest, but peaks in the upper right quadrant in correspondence with the region of maximum $\langle\alpha\rangle$ (Figure 6.11). Despite the lower $\langle V \rangle$ in the upper right quadrant, the increased $\langle\alpha\rangle$ provides sufficient rotation of f towards the tangential direction to yield a net increase in RBM_θ.

6.4 Free surface interaction effects of tidal stream turbines

The previous section analyses the flow mechanisms which drive the performance changes and azimuthal loading variations when a rotor operates in close proximity to an air-water boundary which is assumed to be rigid. However, the observed changes are of small magnitude, and it remains unclear to what extent the rigid lid assumption influences the conclusions drawn. Therefore, the following results repeat the experiment using a simulation method which represents the deforming free surface, albeit at the expense of computational cost and numerical stability. Through comparison to the rigid lid results, the added value of the increased modelling complexity is assessed to inform future practitioners. Simulations carried out with the rigid lid assumption are hereafter referred to

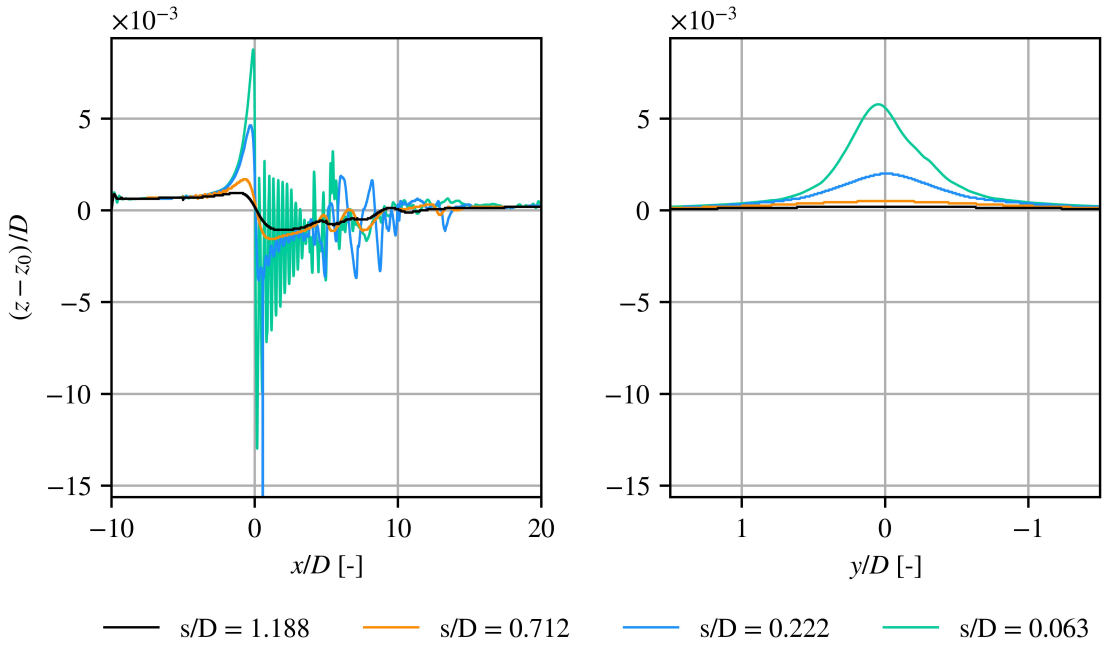


Figure 6.15: The instantaneous surface height (z) relative to the still water surface height (z_0) at $t = 49.92$ s, extracted as the isosurface of $\xi_{\text{water}} = 0.5$. The surface deformations are compared for tip clearances of $s/D = 1.188$, 0.712, 0.222 and 0.063 at a tip-speed ratio of $\lambda = 5.78$. The surface heights are shown in the x-z plane along the centreline $y = 0$ (left), and the y-z plane at $x = 0$ (right).

as rigid lid (RL), while the deformable surface simulations are referred to as VOF.

6.4.1 Surface deformations

Figure 6.15 shows the impact of the turbine on the instantaneous z position of the free surface relative to the still water height (z_0) for all tip clearances at $\lambda = 5.78$, at a time close to the end of the simulation. As the rotation speed is the same between cases, the blades are in the same position at the snapshot. The surface deformation is shown along the domain centreline ($y = 0$) in the streamwise direction, and in the cross-stream direction directly above the rotor plane ($x = 0$). The free surface position is taken to be the position at which the phase fraction (ξ_{water}) is equal to 0.5. In all cases, the centreline surface height decreases between positions far upstream and downstream. As the power extracted by the experimental turbine is small relative to the energy in the flow, this overall change in height is expectedly small, in the region of $6.25 \times 10^{-4} D$ (1 mm), but nevertheless reinforces that static head is removed by the turbine in sub-critical flow conditions.

The change in surface height between far upstream and downstream positions does not change noticeably with s/D as the changes in energy extraction are not significant. However, surface deformations local to the rotor plane increase as the tip clearance is decreased. Ahead of the turbine, the core flow deceleration and radial expansion pushes up the surface to a peak height just

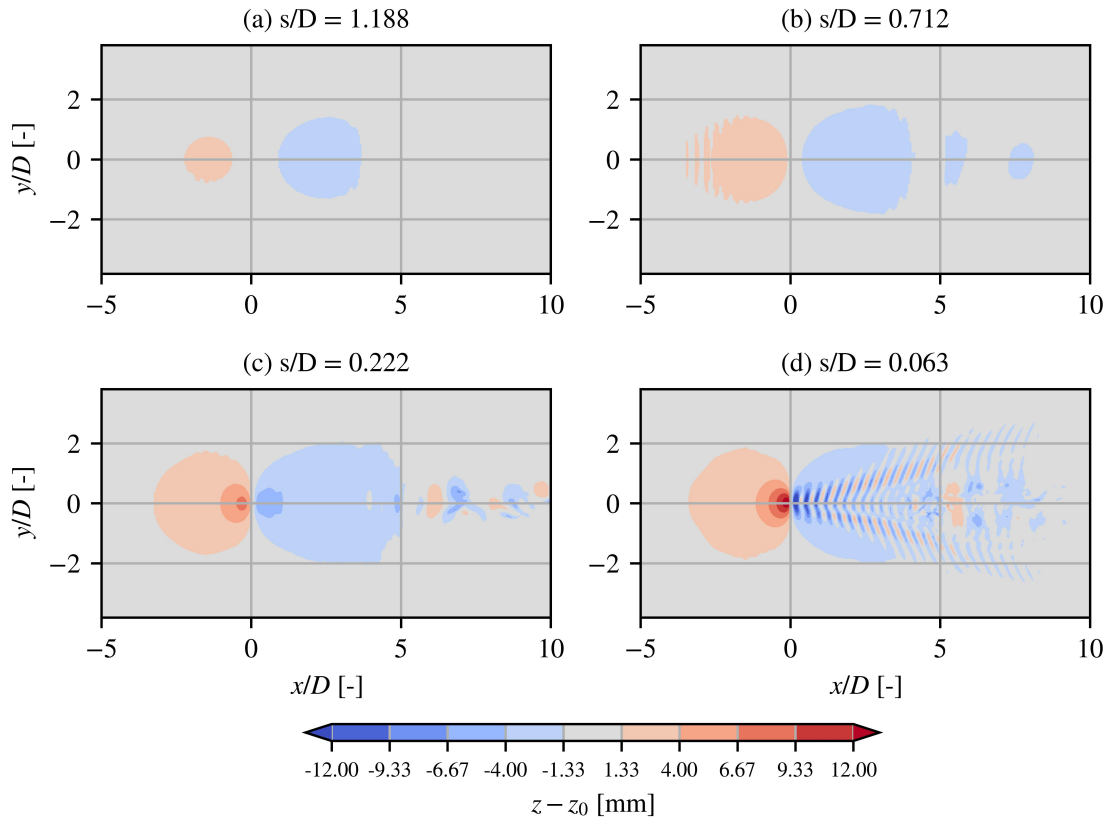


Figure 6.16: Contours of the instantaneous surface height (z) relative to the still water surface height (z_0) at $t = 49.92$ s, extracted as the isosurface of $\xi_{\text{water}} = 0.5$. Tiles (a), (b), (c) and (d) show the surface deformations at tip clearances of $s/D = 1.188$, 0.712, 0.222 and 0.063, respectively, at a tip-speed ratio of $\lambda = 5.78$. The viewing window covers the entire width of the domain in the y direction, but only half of its length in the x direction.

ahead of the rotor plane. Across the rotor plane, the step change in static head due to the applied thrust results in a drop in surface elevation. The amplitude of the downstream set-down correlates with that of the upstream set-up, greatest when the turbine is operating in close proximity to the boundary. In all cases, the deformations are small relative to the turbine diameter, with a range from highest to lowest free surface level of 35 mm ($0.022D$) at most. Above the rotor plane, the region of increased surface elevation extends approximately $1D$ in the y direction either side of the centreline.

As the tip clearance is decreased, the free surface begins to fluctuate downstream of the turbine. In Figure 6.15, oscillations begin at $s/D = 0.222$ and become prominent at $s/D = 0.063$. Contours of surface elevation relative to z_0 are shown in Figure 6.16 and offer additional insight into the structure and spatial extent of the oscillations. At $s/D = 1.118$, 0.712 and 0.222, the surface height recovery downstream of the rotor plane is smooth. However, at the closest simulated proximity, ripples in the surface are generated as the flow passes above the rotor, leading to a V-shaped wave

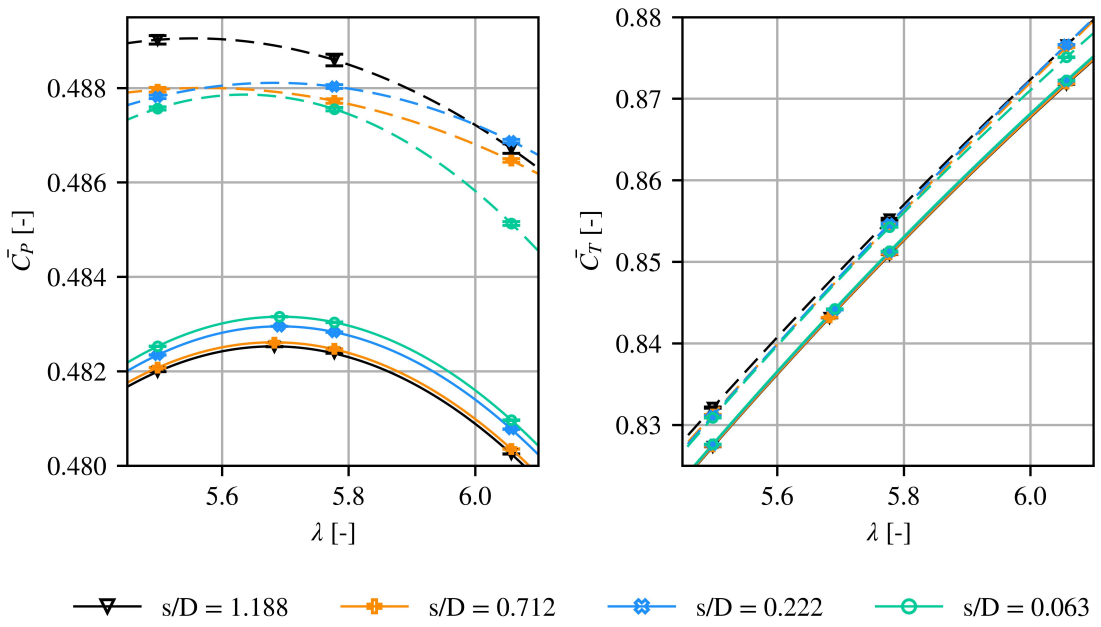


Figure 6.17: A comparison of the time-averaged power (left) and thrust (right) coefficient performance curves predicted by the rigid lid and deformable surface models for varying tip clearances. Solid lines denote results obtained from the rigid lid model, while dashed lines refer to those of the deformable surface model. Vertical bars show an estimation of the 95% confidence interval, taken to be twice the average of the standard error calculated for each phase bin of the last 10 revolutions.

pattern downstream of the turbine. These small wave structures resemble a Kelvin wave pattern, and begin to break down after a downstream distance of $\sim 4D$, most prominently at the centreline where the turbine's wake is closest to the surface.

6.4.2 Rotor performance

The rotor performance coefficients obtained from the VOF simulations are plotted in comparison to their RL counterparts in Figure 6.17. As with the RL results, $\bar{C_P}$ and $\bar{C_T}$ are obtained by time-averaging the power and thrust signals over the last 10 cycles of the simulation. As in Section 6.3.1, vertical bars of $\pm 2SE$ are plotted as an estimation of uncertainty in the mean.

Both $\bar{C_P}$ and $\bar{C_T}$ are higher across the studied range of λ and s/D when the surface deformations are modelled. Taking the average of all cases, a mean increase in power and thrust of 1.1% is observed between the RL and VOF results. However, within the VOF results, straightforward trends in power and thrust are no longer visible. The results show that the mid-depth case produces the highest power, while the case nearest the boundary produces the lowest. Meanwhile, the $\bar{C_P}$ predicted at $s/D = 0.222$ is generally higher than at $s/D = 0.712$, so there is no monotonic trend in $\bar{C_P}$ with respect to tip clearance.

The shape of the $\bar{C_P}$ performance curves predicted by the VOF model, plotted as a quadratic

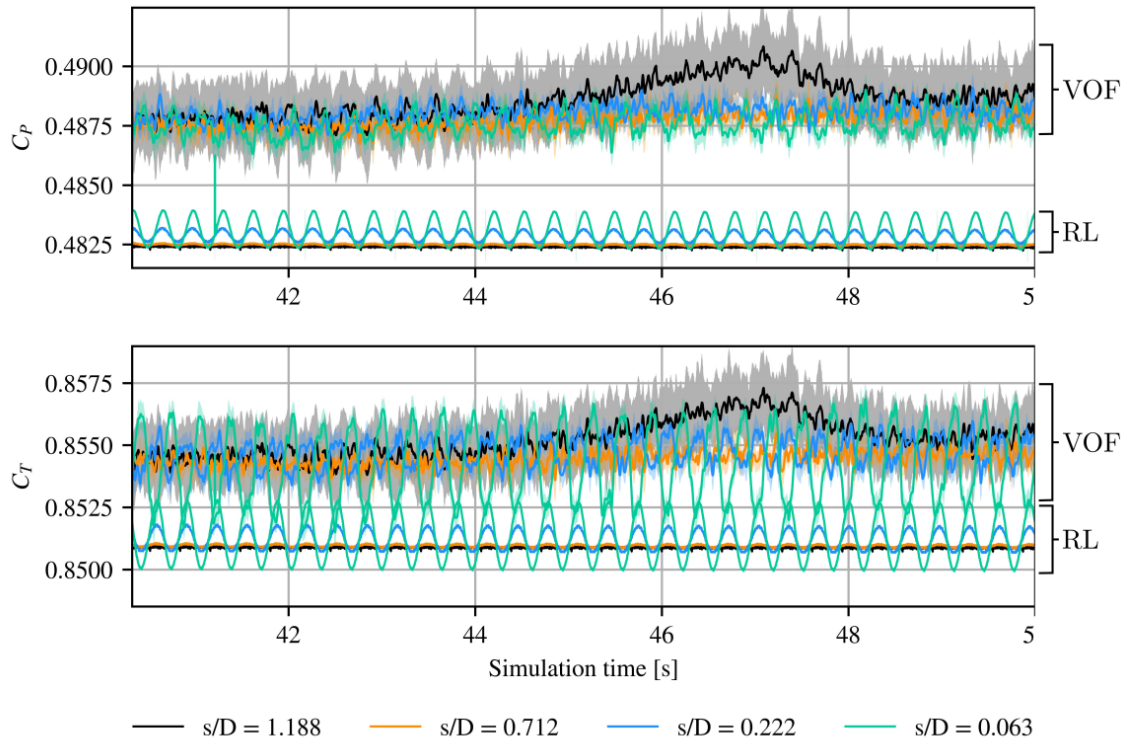


Figure 6.18: Comparing the time series of power coefficient (top) and thrust coefficient (bottom) at $\lambda = 5.78$ predicted by the rigid lid and deformable surface models. Data are plotted over the last 10 rotor revolutions, the window over which the data are averaged in the preceding analyses of Figures 6.2 and 6.17. A shaded region is plotted around each line as a 95% confidence interval according to the rotor's phase. This region represents $\pm 2\sigma^{\Phi}$, where σ^{Φ} is the standard deviation of the data within each 2° phase bin.

fit between data points with dashed lines, is also not consistent across the range of s/D. There is reasonable agreement between cases at the extremes of the tip clearance range, however, the intermediate s/D cases have flatter performance curves. Given the inconsistency in the curve predicted λ^* values across the tip clearance range, and the associated computational cost of additional simulations, the iterative procedure to find the optimal $\bar{C_P}$ was not carried out for the deformable surface cases.

To further investigate the performance, the time history of power and thrust are plotted over the time-averaging window in Figure 6.18. As an indication of the uncertainty in the time series data, a 95% confidence interval of $\pm 2\sigma^{\Phi}$ is plotted as a shaded region around each line. σ^{Φ} refers to the standard deviation of the data within 2° azimuthal bins, indicating the variability of the data at each azimuthal position between rotation cycles, while removing the regular oscillation due to boundary proximity.

The RL results have negligible uncertainty with stable and well-defined oscillations at the blade passing frequency. In the VOF results, regular periodicity at the blade passing frequency can be visually identified in the power and thrust signals at $s/D = 0.222$ and 0.063, however, there

is significantly more noise than in the RL cases resulting in larger confidence interval bands. A long period transient in the mid-depth power and thrust signals is observed, particularly from a simulation time of 44 s onwards. This contributes to the mid-depth case having a greater σ^{Φ} across the azimuthal cycle than the other tip clearances, to such a degree that the confidence interval is larger than the changes due to s/D in the stable region prior to the transient.

Given the large number of samples within the time-averaging window, the global standard errors of $\bar{C_P}$ and $\bar{C_T}$ are insignificant relative to the performance changes in Figure 6.17. However, the performance predictions are not stable and low frequency transients exist at periods of similar order to the length of the averaging window. To demonstrate the variability within the averaging period, the cycle-to-cycle residuals are examined.

In the VOF results, the cycle-to-cycle residuals over the last 10 rotor revolutions are less than 0.05% in power and 0.025% in thrust for tip clearances $s/D = 0.712$, 0.222 and 0.063. At mid-depth, the residuals of power and thrust only remain below 0.2% and 0.05% respectively due to the long period transient. In the RL simulations, the cycle-to-cycle residuals are consistent across the cases, and between 10 and 40 times lower than the VOF simulations. Although these convergence tolerances might not be considered excessive in other rotor simulation applications, the maximum cycle-to-cycle residuals in the VOF results at mid-depth are significant with respect to the magnitude of performance changes between tip-clearance cases.

6.4.3 Azimuthal blade loading variations

Figure 6.19 shows the phase-averaged RBMs from both modelling approaches, normalised by the azimuthal mean of the respective mid-depth case, with a confidence interval of $\pm 2SE^{\Phi}$ surrounding each line. Table 6.2 provides the magnitude and phase of maximum and minimum points, characterising the RBM distributions and enabling quantified comparison between the two modelling techniques.

The normalised RBM distributions obtained from the VOF model are less smooth than those of the RL simulations, particularly in the edgewise direction. Additionally, the confidence interval increases when moving from RL to VOF modelling, most prominently at mid-depth, indicating that the variability between cycles is greater. However, the size of the confidence interval is insignificant relative to the magnitude of the azimuthal variations.

The azimuthal distributions of normalised $\langle \mathrm{RBM}_{\theta} \rangle$ are similar in shape between the VOF and RL simulations. However, since the highest power in the VOF simulations is recorded at mid-depth, the curves from the VOF simulations at lower tip clearances are lower than their RL counterparts as the azimuthal mean of $\langle \mathrm{RBM}_{\theta,md} \rangle$, by which they are normalised, is larger. At

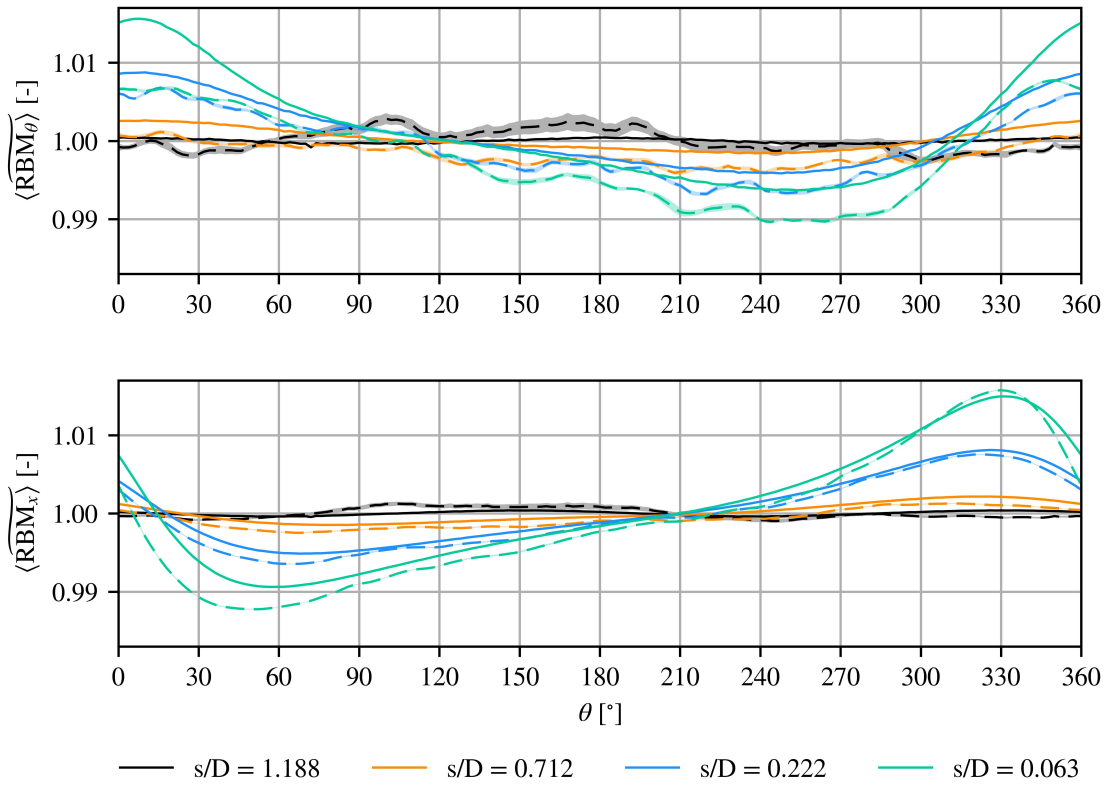


Figure 6.19: Comparing the normalised phase-averaged root bending moment of an individual blade in the edgewise (top) and flapwise (bottom) directions at $\lambda = 5.78$ predicted by the rigid lid (solid line) and deformable surface (dashed line) models. The point of closest proximity to the free surface is at $\theta = 0°$. The data are normalised by the azimuthal mean of the phase-averaged RBM at $s/D = 1.188$ (mid-depth), $\frac{1}{N_B}\sum_{b=1}^{N_B}\langle RBM_{md}\rangle$, for each of the rigid lid and deformable surface data respectively. This normalisation is denoted by $(\tilde{.})$. A shaded region of $\pm 2SE^{\Phi}$ is plotted around each line as a 95% confidence interval.

$s/D = 0.712$ and 0.222, the normalised $\langle \mathrm{RBM}_\theta \rangle$ ranges, and the phases of the maxima and minima, are similar between the two modelling techniques.

As in the RL results, the greatest normalised $\langle \mathrm{RBM}_\theta \rangle$ range is at the lowest tip clearance in the deformable surface simulations. However, the peak value is lower, differing less significantly from the peak value at $s/D = 0.222$ than in the RL results. At $s/D = 0.063$, the peak $\langle \mathrm{RBM}_\theta \rangle$ in the upper region ($\theta = 340° \rightarrow 50°$) is flatter and lower in magnitude in the VOF simulation than the RL. The position of maximum $\langle \mathrm{RBM}_\theta \rangle$ moves from $\theta = 8°$ to $\theta = 350°$, now a phase lead relative to TDC. This differs from the intermediate tip clearance cases, in which the maximum $\langle \mathrm{RBM}_\theta \rangle$ lags TDC in both modelling approaches.

The azimuthal distributions of normalised $\langle \mathrm{RBM}_x \rangle$ show very good agreement between the models. This can be observed qualitatively in Figure 6.19, while Table 6.2 confirms that the loading ranges and phases of the maxima and minima agree closely between the models. At $s/D = 0.063$, the minimum normalised $\langle \mathrm{RBM}_x \rangle$ is lower with the deformable surface model than the rigid lid,

Table 6.2: A comparison of the normalised phase-averaged RBM distribution characteristics in the edgewise and flapwise directions obtained from the rigid lid and deformable surface simulations at $\lambda = 5.78$ across the range of tip clearances. The loading patterns are characterised by the maximum value, minimum value, the phases at which these occur, and the range calculated as the difference between maximum and minimum values. All RBM values are normalised by the azimuthal mean of the phase-averaged RBM at $s/D = 1.188$ (mid-depth), $\frac{1}{N_B}\sum_{b=1}^{N_B}\langle RBM_{md}\rangle$, for each of the rigid lid and deformable surface data respectively. This normalisation is denoted by $(\tilde{\cdot})$.

	Rigid lid					**Deformable surface**				
s/D	max($\langle\widetilde{\mathrm{RBM}_\theta}\rangle$) [-]	Phase [°]	min($\langle\widetilde{\mathrm{RBM}_\theta}\rangle$) [-]	Phase [°]	range($\langle\widetilde{\mathrm{RBM}_\theta}\rangle$) [-]	max($\langle\widetilde{\mathrm{RBM}_\theta}\rangle$) [-]	Phase [°]	min($\langle\widetilde{\mathrm{RBM}_\theta}\rangle$) [-]	Phase [°]	range($\langle\widetilde{\mathrm{RBM}_\theta}\rangle$) [-]
0.063	1.0156	8	0.9937	254	0.0219	1.0078	350	0.9896	244	0.0181
0.222	1.0088	10	0.9959	248	0.0129	1.0068	16	0.9932	220	0.0136
0.712	1.0026	10	0.9984	238	0.0042	1.0012	16	0.9959	208	0.0052
1.188	1.0005	358	0.9992	72	0.0013	1.0028	100	0.9975	300	0.0053
s/D	max($\langle\widetilde{\mathrm{RBM}_x}\rangle$) [-]	Phase [°]	min($\langle\widetilde{\mathrm{RBM}_x}\rangle$) [-]	Phase [°]	range($\langle\widetilde{\mathrm{RBM}_x}\rangle$) [-]	max($\langle\widetilde{\mathrm{RBM}_x}\rangle$) [-]	Phase [°]	min($\langle\widetilde{\mathrm{RBM}_x}\rangle$) [-]	Phase [°]	range($\langle\widetilde{\mathrm{RBM}_x}\rangle$) [-]
0.063	1.0150	330	0.9906	58	0.0244	1.0157	330	0.9878	52	0.0280
0.222	1.008	326	0.9949	68	0.0132	1.0075	322	0.9935	64	0.0140
0.712	1.0022	320	0.9990	76	0.0036	1.0013	310	0.9975	68	0.0037
1.188	1.0003	326	0.9995	72	0.0008	1.0012	104	0.9990	246	0.0022

leading to a slightly larger loading range.

The characteristic shapes of the loading distributions analysed in Section 6.3.2 are also seen in the results of the deformable surface simulations. Although not presented for brevity, contours of the phase-averaged blade sectional forces generated from the deformable surface results were also analysed, yielding equivalent distributions to those seen in Figures 6.5 and 6.6.

6.4.4 Near-boundary flow effects

Figure 6.20 shows $\bar{U_\theta}$ extracted from the flow field of the VOF simulations. The findings are the same as those concluded from the rigid lid data (Figure 6.7). At mid-depth there is no tangential component to the incoming flow (tile (a)), so $\bar{U_\theta}$ at the rotor plane is azimuthally constant (tile (b)), and is purely in response to the rotor's torque. At $s/D = 0.063$, the imposition of the inflow $\bar{U_\theta}$ distribution (tile (d)), which is symmetric about a vertical axis on the domain's centreline, on the otherwise constant torque-induced tangential velocity leads to the azimuthal variations seen at the rotor plane (tile (e)). Although the differences are subtle, close comparison of Figures 6.7 and 6.20 finds that the $\bar{U_\theta}$ variations are slightly greater in the deformable surface simulation. This indicates that the lateral diversion effect is slightly stronger with the modelled free surface than the rigid lid, but most importantly, the flow phenomenon is consistent between the modelling approaches.

Figure 6.21 shows contours of the phase-averaged axial velocity sampled by the AL method in the deformable surface simulations at $\lambda = 5.78$. In agreement with Figure 6.9, operating the turbine in close proximity to the boundary increases the $\langle u_x\rangle$ experienced by the outboard section of the blade when it is close to the boundary, and decreases $\langle u_x\rangle$ on the opposite side of the rotation.

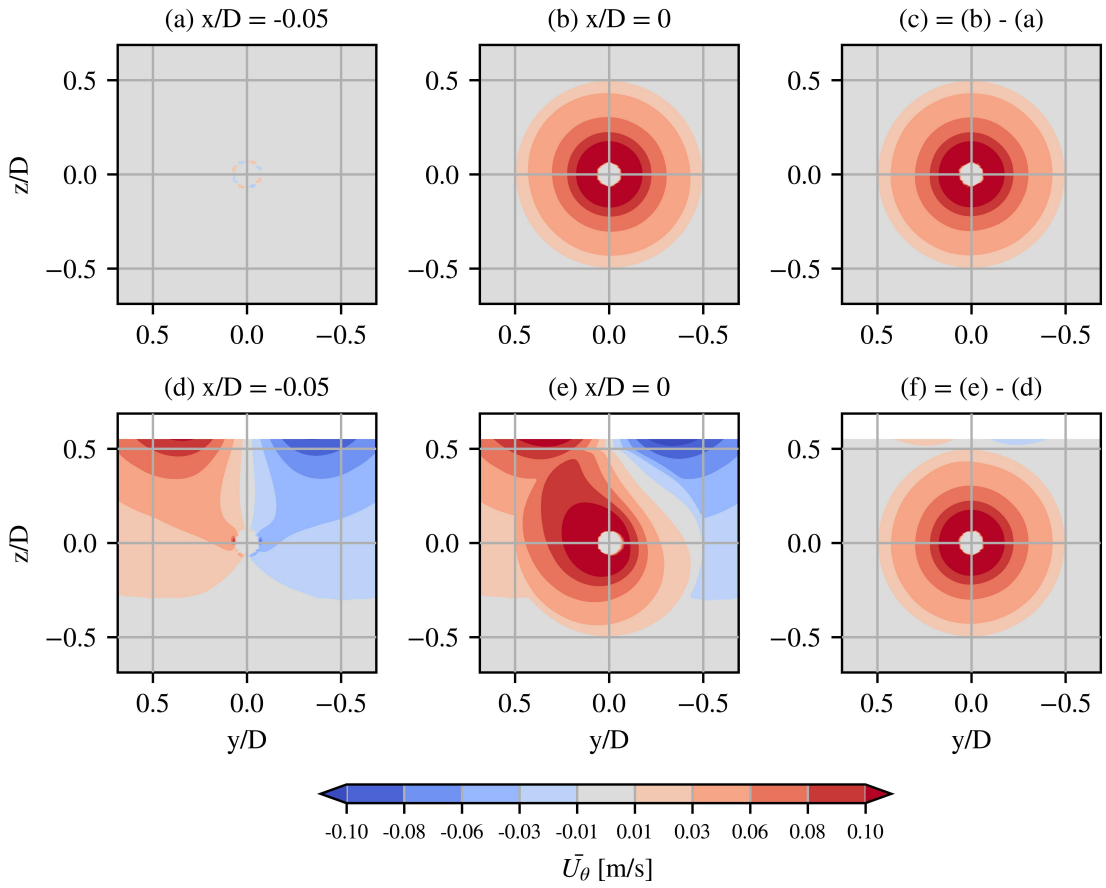


Figure 6.20: Deformable surface modelling: Contours of the time-averaged tangential velocity component in the y-z plane, extracted from the flow field at stations $0.05D$ upstream of the rotor plane ((a) and (d)), and at the rotor plane ((b) and (e)). Also shown is the subtraction of the upstream $\bar{U}_\theta$ field from that measured at the rotor plane ((c) and (f)). The first row ((a) to (c)) shows results of a turbine operating at mid-depth ($s/D = 1.188$), while the second row ((d) to (f)) shows results from a turbine near the boundary at $s/D = 0.063$. All plots are shown at $\lambda = 5.78$. $\bar{U}_\theta$ is defined to be positive in the anticlockwise direction and is displayed in units of m/s. White space at the top of the contours at $s/D = 0.063$ are added in post-processing, and indicate the region occupied by air in still water conditions.

Compared to those observed with a rigid lid (Figure 6.9), the regions of decelerated $\langle u_x \rangle$ are slightly more significant in the deformable surface simulations (Figure 6.21), spreading further along the blade span.

By contrast, the region of increased $\langle u_x \rangle$ affects less of the blade when the free surface deformations are modelled, implying that the rigid lid yields a greater acceleration of the bypass flow. Figure 6.15 shows how the free surface is locally elevated by the presence of the rotor, slightly increasing the effective tip clearance. Moreover, the peak $\langle u_x \rangle$ seen at the top of the rotation is lower in the VOF simulation at $s/D = 0.063$ than in the RL equivalent.

The phase-averaged angle of attack and relative velocity magnitude seen by the blade at $r/R = 0.8$ in the VOF simulations are shown in Figure 6.22. At this radius the blade is not subject to significant losses in blade loads from tip effects, but the radius is still large resulting in high

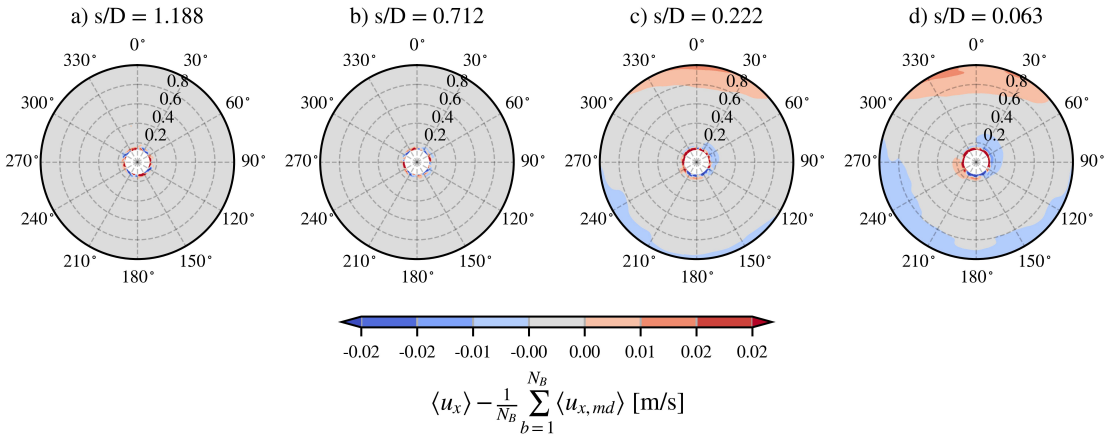


Figure 6.21: Deformable surface modelling: Contours showing the phase-averaged axial velocity component as sampled by the AL method at each position on the rotor plane at $\lambda = 5.78$. The velocity is shown relative to the azimuthal mean of the phase-averaged velocity at $s/D = 1.188$ (mid-depth), calculated individually for each radial position. The radial axis is $r/R \in [0, 1]$ while the angular coordinate is the azimuthal position.

relative flow speeds, hence, large blade forces. These forces are applied at a point of substantial radial distance from the hub connection, such that this location contributes significantly to the generation of root bending moments. Therefore, it offers a good representative from which to compare the sampled flow velocities between modelling techniques, and link to the previously analysed RBM distributions.

As the governing flow phenomena have been found to be consistent between RL and VOF models, the azimuthal distributions of $\langle \alpha \rangle$ and $\langle V \rangle$ are expectedly similar. The range of the azimuthal variations again increase as tip clearance is decreased.

The phase-averaged angle of attack is consistently higher in the deformable free surface modelling simulations, likely due to a higher axial flow velocity which would be compatible with the higher thrust and power seen in these cases. However, the nature of the azimuthal variations remain the same with $\langle \alpha \rangle$ reaching its maximum slightly after TDC and its minimum as TDC is approached.

The azimuthal variations of $\langle V \rangle$ also share the same distribution between modelling approaches, but the mean value predicted by the deformable surface model is slightly higher. The models agree closely in the range of variation, and the position at which maxima and minima occur. The most notable difference occurs at $s/D = 0.063$, at which point the VOF simulations predict a greater $\langle V \rangle$ variation due to the larger azimuthal variations in tangential velocity (Figure 6.20). As discussed previously, changes in $\langle \mathrm{RBM}_x \rangle$ are predominantly driven by changes in $\langle V \rangle$, hence the greater $\langle \mathrm{RBM}_x \rangle$ range noted in Figure 6.19 and Table 6.2.

The differences in $\langle \mathrm{RBM}_\theta \rangle$ distributions between the two modelling approaches can also be

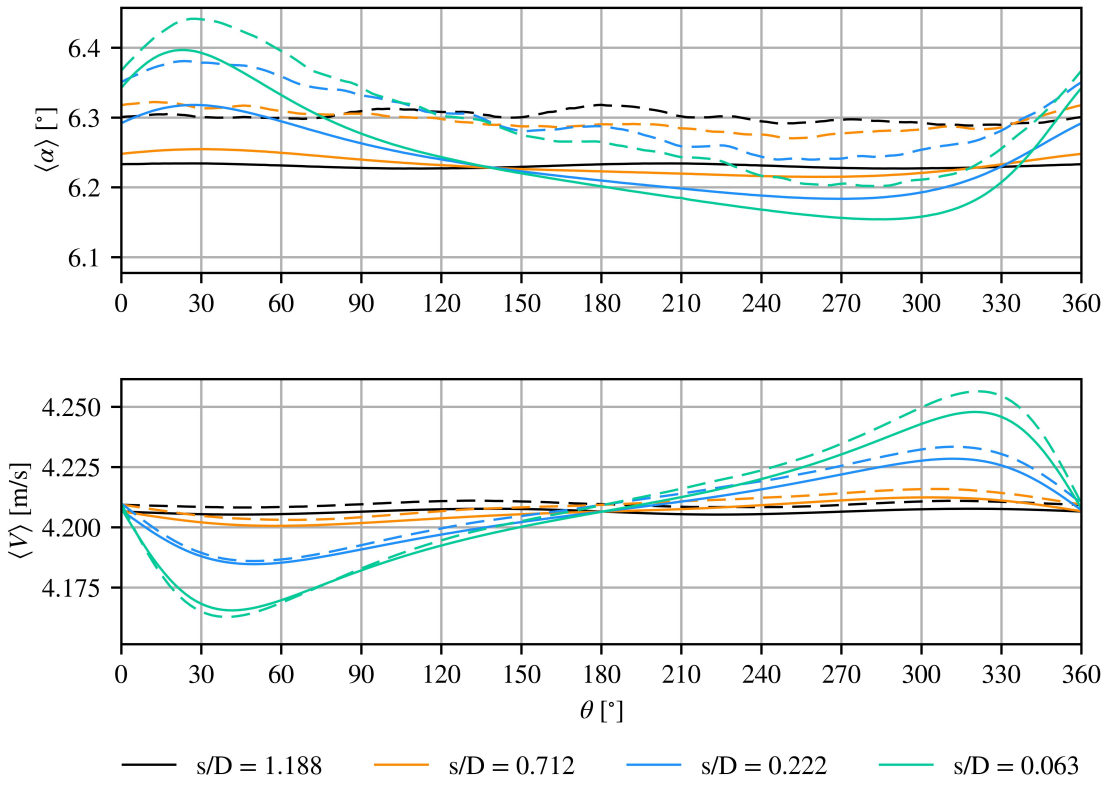


Figure 6.22: The phase-averaged relative velocity magnitude and angle of attack experienced by an individual blade at $r/R = 0.8$ and $\lambda = 5.78$. A comparison is drawn between the results of the rigid lid (solid line) and deformable surface (dashed line) models. The point of closest proximity to the free surface is at $\theta = 0^{\circ}$. A shaded region of $\pm 2SE^{\Phi}$ is plotted around each line as a 95% confidence interval.

attributed to the larger $\langle V \rangle$ range experienced with a deformable free surface. The flatter peak in $\langle \mathrm{RBM}_{\theta} \rangle$ observed in the VOF results at $s/D = 0.063$, along with the shift in the maximum from a phase lag to a phase lead, arises due to the increased influence of $\langle V \rangle$ in the opposing contributions of $\langle V \rangle$ and $\langle \alpha \rangle$ on $\langle \mathrm{RBM}_{\theta} \rangle$ either side of TDC. Ahead of TDC, the higher $\langle V \rangle$ contributes to increase $\langle \mathrm{RBM}_{\theta} \rangle$ but is offset by the reduction in $\langle \alpha \rangle$. After TDC, the decrease in $\langle V \rangle$ reduces $\langle \mathrm{RBM}_{\theta} \rangle$ while the increased $\langle \alpha \rangle$ acts to enhance it. In the lowest tip clearance RL simulation, the $\langle \alpha \rangle$ variation dominated resulting in a peak which lagged TDC. In the equivalent VOF case, the increased variation of $\langle V \rangle$ takes precedence, flattening the $\langle \mathrm{RBM}_{\theta} \rangle$ peak and shifting the maximum to lead TDC.

6.5 Discussion

It is noted that the rigid lid model is not fully representative of a tidal stream turbine in subcritical open channel flow as it assumes a negligible Froude number. The channel Froude number is calculated as $\mathrm{Fr} = U_{\infty}/\sqrt{gz_0}$, where z_0 is the water depth in the undisturbed channel and g is

the acceleration due to gravity. Prospective tidal energy sites typically have a Froude number between 0.1 and 0.2, so a drop in the free surface height is expected as energy is extracted by operating turbines [23]. The Froude number of the simulated tidal channel was 0.12, but the energy extracted by the experimental turbine was low relative to the energy in the flow, so the overall drop in surface height was expected to be small. Whilst this was found to be true, the deformation local to the turbine was larger (although only up to a maximum deviation of $0.022D$), perceptibly impacting the degree of axial flow acceleration through the adjacent region of the rotor plane at low tip clearances.

The rigid lid simulations were comparably simple to carry out, and produced stable results which achieved excellent convergence in the cycle-to-cycle mean rotor performance coefficients. Consequently, the precision of the measured performance coefficients was appropriate to capture the subtle changes experienced due to changes in tip clearance. Modelling the deformation of the free surface required significantly more input from the practitioner in set-up, and in managing the increased likelihood of numerical instability. To stabilise the simulations, automatic timestep adjustments were required as well as the application of an under-relaxation factor, the latter of which was found to impact the final rotor performance coefficients. Despite these treatments, the residuals in cycle-to-cycle performance coefficients could not be converged to the same degree as in the rigid lid simulations, particularly for the case at mid-depth. Additionally, the inlet-outlet boundary conditions used to simplify the modelling prescribed a non-physical energy balance across the domain. As a result, the deformable surface simulations cannot be said to validate the performance trends observed in the rigid lid results, leaving this part of the investigation inconclusive. Nevertheless, the mechanisms responsible for the azimuthally varying flow field were similarly captured by the two surface modelling approaches leading to significant agreement in the loading distributions.

The limitation of the AL method to capture unsteady load variations due to its use of the BE method is also noted. Using the definition of [56], the reduced frequency (k) of an assumed once-per-revolution flow perturbation was calculated *a posteriori* using the measured relative velocity magnitude. The quasi-steady assumption of the BE force calculation can be considered valid outboard of $r/R = 0.77$ where $k < 0.1$ [56]. However, an unsteady hydrofoil response is expected across much of the blade, and the ability of the AL method to capture such behaviour is not well understood. Despite the majority of the RBMs, and their variations, being generated by the outboard sections, the fidelity of the load calculation is a limitation of the approach on the inboard sections of the blade where the degree of unsteadiness is significant.

6.6 Conclusions

In the rigid lid results, decreasing the normalised tip clearance (s/D) from 1.188 to 0.063 increased the maximum power and thrust coefficients by 0.13%, and slightly increased the optimal tip-speed ratio. Over this range of s/D, the change in performance was monotonic with tip clearance. There was no clear trend in the deformable surface results, however, there was insufficient confidence in the precision of the performance prediction to substantiate or refute the conclusions drawn from the rigid lid results. Overall, the changes in performance due to boundary proximity are too small to be of practical significance to turbine operators.

Near-boundary operation also induced a once-per-revolution loading cycle to the root bending moments, the range of which increased as s/D was decreased. The flapwise root bending moment experienced a maximum range of 2.8%, recorded by the deformable surface model, and consistently peaked ahead of top dead centre. The edgewise root bending moment had lower range, a maximum of 2.2% came from the rigid lid results, and its peak generally lagged top dead centre. Flapwise root bending moments were insensitive to changes in the angle of attack, hence their distribution followed that of the relative velocity magnitude. Contrastingly, edgewise root bending moments showed greater dependence on the angle of attack, varying in response to changes in both the angle of attack and the relative velocity magnitude over the rotor plane. The trends in phase of the loading peaks are accordant with observations made in previous experimental work [30].

Modelling the free surface deformations only changed the root bending moment distributions at the lowest tip clearance and only in the edgewise direction. Subtle changes in the near-boundary flow field broadened the edgewise root bending moment peak, reducing its fluctuation range and shifting its position to lead top dead centre. The important conclusion for turbine designers and operators is that operating in close proximity to a boundary introduces a once-per-revolution loading cycle, contributing to increased fatigue damage. However, the maximum RBM fluctuations recorded in this study are unlikely to be of significant concern relative to effects of waves, shear or turbulence.

The same two flow mechanisms were observed with both surface modelling approaches. Flow constriction increased the streamwise velocity through the rotor plane adjacent to the boundary. Additionally, the radial component of the expanding flow upstream of the turbine was diverted by the boundary into the lateral directions, resulting in a non-uniform tangential flow velocity at the rotor plane. Consequently, the tangential flow velocity increased on the upstroke, but decreased on the downstroke. The deformable surface model resulted in subtly larger tangential velocity variations, but lesser axial flow acceleration at the lowest tip clearance. These flow mechanisms have been shown to be the cause of the azimuthally varying blade loads, and became more prominent as

the tip clearance was decreased.

The multi-phase simulations were successful in capturing the local surface deformations above the rotor, observing a maximum vertical range of 0.022 rotor diameters. However, modelling the deformation of the free surface increased the computational cost by an order of magnitude, and the cycle-to-cycle variations in performance at the end of the simulated period were 10-40 times larger than the rigid lid cases, indicating a lesser degree of convergence. Given the instability of the power and thrust signals, the uncertainty associated with the inlet-outlet boundary conditions, and the lack of a clear trend in the performance curves, the multi-phase simulations do not provide sufficient confidence to conclude that the changes in power and thrust observed when varying the proximity to the deformable free surface are significant. Hence, the multi-phase simulations cannot be used to support the performance changes observed in the rigid lid results, and no firm conclusions can be drawn from this study regarding the impact of free-surface proximity on turbine performance. Despite this, good agreement was observed between the two surface modelling approaches in the predicted azimuthal distributions of blade loads and blade-relative flow components, and the flow mechanisms from which they arise were consistent, providing confidence in the conclusions drawn regarding these aspects. The rigid lid model sufficiently captured the loading variations and driving flow mechanisms which were observed in the multi-phase simulations, and differences in the time-averaged rotor performance due to the modelling technique were insignificant. Therefore, the rigid lid approach is found to be suitable for modelling tidal stream turbines operating near the free surface in the absence of surface waves.

Part IV

Blade design methods for tidal stream turbine rotors

Chapter 7

Introduction

As the primary mechanism for interaction between a turbine and the energy resource, the rotor plays a key role in determining the efficiency with which energy can be removed from the flow and the resultant forces that are imparted on the structure in doing so. This balance of energy production in relation to the structural loading contributes to the evaluation of the cost of energy (COE), a key metric indicating the economic benefit of a renewable energy source.

Designing aerodynamic surfaces for rotating machinery has been studied for other applications, and experience can be drawn from previous work in the aerospace industry and the more mature wind energy industry. Given the relative infancy of the tidal stream energy industry, consensus surrounding optimising the hydrodynamic performance of the turbine blades does not yet match that of the more mature fields. Additionally, the specific flow environment in which tidal turbines operate, with high blockage ratios, dense fluid, and floating platforms being commonplace, offer a new challenge, so application-specific design methods and objectives should be considered. Hence, there is space for further refinement of the design practices, and the considered blade geometries, to specifically target the requirements of an efficient tidal rotor.

The classical approach to blade design uses the BEM method to derive analytical expressions of the optimal chord and twist distributions, based on a selected design TSR and distribution of hydrofoils along the span. The design philosophy is strongly tied to the optimal performance prediction of Lanchester, Betz and Joukowsky for a turbine in unbounded flow, aiming to maximise power production by specifying a geometry which achieves an axial induction factor of $a = 1/3$, and is reported in detail by Jamieson [70].

The selection of the design angle of attack (α_d) is central to the analytical BEM design approach as it specifies the lift coefficient at the design point ($C_{l,d}$). Considering that the drag force acts predominantly in opposition to the torque generated by a blade element (see Equation 7.1), which is driven by the hydrofoil's lift, the design angle of attack is commonly selected to be the point at which the C_l/C_d ratio is maximised [14, 70]. Jamieson comments that this may not always be the exact optimal α_d, but is a sufficient approximation [70].

$$\delta Q = \frac{1}{2}\rho V^2 c N_{Bl}(C_l \sin(\phi) - C_d \cos(\phi)) r \delta r \tag{7.1}$$

$$\delta T = \frac{1}{2}\rho V^2 c N_{Bl}(C_l \cos(\phi) + C_d \sin(\phi)) \delta r \tag{7.2}$$

From LMADT, the axial induction factor for optimal power production corresponds to an optimal thrust coefficient, $C_T = 8/9$. As the inflow angle (ϕ) is typically small across much of the blade (such that $\cos(\phi) \gg \sin(\phi)$), particularly on the outboard sections, and C_l is expected to be significantly larger than C_d at near-optimal hydrofoil operation, the axial force generated by a blade element (δT) is reasoned to be dominated by the lift contribution (see Equation 7.2). Therefore, the existence of an optimal thrust coefficient suggests that there is a corresponding optimal lift force for each blade element, specifying the product cC_l.

Equation 7.3 is an expression of the non-dimensional lift distribution (cC_l/R) in the absence of a tip correction factor, which varies with λ and r/R, and is derived by rearranging the BEM equation in the axial direction (Equation 4.12) while making use of the relationship in Equation 4.11.

$$\frac{cC_l}{R} = \left(\frac{8\pi a(1-a)}{N_{Bl}\lambda(1+a')\sqrt{(1-a)^2 + \lambda^2(\frac{r}{R})^2(1+a')^2}} \right) \left(\frac{1}{1 + \frac{1-a}{\frac{C_l r}{C_d R}\lambda(1+a')}} \right) \tag{7.3}$$

For the purposes of practical rotor design, the second term on the right hand side is often taken as 1.0, since the lift-to-drag ratio of modern hydrofoils is large, so the product $\lambda C_l/C_d$ is also large. Additionally, since the tangential induction factor is small in real operation, the $1 + a'$ term is also taken as 1.0. Finally, it is approximated that $(1-a)^2 \ll \lambda^2(r/R)^2$ to simplify Equation 7.3 to the form presented in Equation 7.4, which is similarly similarly quoted by [14], [70] and [107].

$$\frac{cC_l}{R} = \frac{8\pi a(1-a)}{N_{Bl}\lambda^2(\frac{r}{R})} \tag{7.4}$$

The optimal non-dimensional lift distribution is obtained by substituting $a = 1/3$, yielding Equation 7.5. Hence, the optimal chord distribution is analytically derived for specified $C_{l,d}$ and λ_d, neglecting drag, a' and tip loss effects.

$$\frac{cC_l}{R} = \frac{16\pi}{9N_{Bl}\lambda^2(\frac{r}{R})} \tag{7.5}$$

The corresponding optimal twist distribution, defined in Equation 7.6, is similarly derived by specifying $a = 1/3$ in Equation 4.11, assuming $a' \approx 0$ and using the small angle approximation $\tan^{-1}(x) \approx x$.

$$\beta = \frac{2}{3\lambda(\frac{r}{R})} - \alpha_d \tag{7.6}$$

This approach provides simple expressions which allow rapid generation of blade geometry distributions based on *a priori* selections of hydrofoil profile, rotor diameter and λ_d. Owing to the simplicity of its application, the BEM method is the most widely used theory in wind turbine rotor design [70], and has been used to design TST rotors [108, 109]. However, when operating in highly constrained flows, which is likely for TSTs, the assumptions of analytical BEM break down as it does not model the interaction of the turbine with its flow domain.

To address this, McIntosh et al. [32] developed an iterative design routine specifically for rotors operating in blocked flow conditions, integrated with a model which implements the blade element method on an actuator disc with flow components derived from RANS CFD, hence its name: RANS-BE. Adopting a similar strategy to the analytical BEM design approach, the RANS-BE design procedure aims to maximise the power coefficient by adjusting the geometric twist to achieve the α which corresponds to the hydrofoil's maximum C_l/C_d ratio. Simultaneously, the chord distribution is iterated to achieve an input target local thrust coefficient, which often corresponds to the Betz-optimal thrust coefficient, but can also be tuned to optimise the performance at a particular blockage ratio. McIntosh et al. validated the RANS-BE modelling strategy by comparison to BEM results in unconstrained flow, showing good agreement. Also, by designing a rotor specifically for its intended flow environment, the maximum power coefficient of a ducted TST was increased by 17% in comparison to the use of a rotor designed for unconstrained flow [32].

The method has since been used on numerous occasions to compare the performance and geometry characteristics of turbines designed for blocked conditions [31, 110, 111], and to design blades for scale turbines used in experimental testing [28, 68]. In particular, Schluntz and Willden [31] used the RANS-BE approach to design rotors optimised to operate in specific local blockage conditions generated by proximity to neighbouring turbines in a co-planar array fence. Rotors designed for the highest blockage achieved the highest power coefficient, requiring greater rotor solidity and lower blade twist than those designed for unconstrained flow. Despite its success in capturing the influence of blockage on the hydrodynamic design, discrete blade effects are not modelled as the rotor force is distributed around annular rings. Hence, the RANS-BE tool cannot be used to consider the implication of varying the number of blades on the rotor's hydrodynamic performance and design.

While the previously described methods provide useful tools for designing rotors for maximum power production, more thorough design strategies considering multiple objectives are most effectively realised by coupling rotor modelling with optimisation techniques [70]. Given its practicality as a low cost, easy to implement model, the BEM method is a common choice for evaluating the rotor performance in wind turbine blade geometry optimisations [112, 113, 114, 115, 116, 117]. The model's low cost allows the authors to include structural models and detailed cost evaluations in their optimisations. For example, Fuglsang and Madsen [112] utilised the BEM method alongside structural models to minimise the cost of energy of a 1.5 MW stall regulated wind turbine using deterministic optimisation techniques. A 3.5% reduction in COE was achieved by iteratively adjusting design variables controlling the rotor shape, aerofoil polars, tip-speed ratio and pitch angle according to gradients obtained by finite-difference evaluation. Similarly, Kenway and Martins

[113] simultaneously optimised the aerodynamic and structural geometry of wind turbine blades to maximise the annual energy production of a 5 kW wind turbine using a gradient-based optimisation algorithm. Blades were optimised to maximise the energy yield from site-specific wind speed probability distributions while constraining the maximum blade cost, stress and rotor power.

According to the scoping review carried out by Kumar et al. [118], studies related to the optimisation of wind turbines significantly outnumber those addressing tidal turbine optimisation. Of the studies available in the literature, tidal turbine blade design optimisations almost exclusively utilise the BEM method to evaluate the performance of the rotor, and stochastic evolutionary algorithms are a common choice [119, 120, 121, 122, 123, 124]. Sale et al. [119] optimised the radial distribution of chord, twist and hydrofoil thickness-to-chord ratio using a genetic algorithm with BEM performance evaluation. The optimiser aimed to maximise the power production of a 5 m diameter stall-regulated turbine across the operating range of flow speeds, avoiding solutions which are predicted to cavitate. The same optimisation algorithm and objective was later employed in the design of a 20 m diameter TST with variable speed and pitch control by both Bir et al. [120] and Lawson et al. [121], this time optimising only the chord and twist distributions. Tahani et al. [123] trialled multiple meta-heuristic algorithms, including a genetic algorithm, in their multi-objective optimisation of an existing experimental scale TST. The chord and twist distributions were optimised to simultaneously maximise the power coefficient and the start-up torque. Finally, Zhu et al. [124] employed the BEM method to evaluate rotor performance while optimising a 5.4 m diameter turbine to maximise its mean power coefficient while minimising the variance of C_P variance across a range of λ. A neural network model was coupled with a genetic algorithm to sequentially optimise the twist distribution, followed by the chord distribution.

Although the rapid objective function evaluations with the BEM method allow thorough optimisations of rotor geometry, the generated designs are intrinsically limited by the capabilities of the model, leading some authors to seek higher fidelity results through optimisation with CFD simulations. Although fewer iterations are possible due to time and resource constraints, each objective function evaluation is expected to capture more of the physics of a discrete rotor blade than with the BEM method. Prior to its application to wind or tidal turbines, the approach of combining numerical optimisation and CFD simulations for geometric design was studied in the aerospace industry. The design of aircraft lifting surfaces, in particular helicopter blades, share some common goals with designing horizontal axis turbines. Lyu et al. [125] used an adjoint method to inform a gradient-based optimiser with the objective of modifying the wing geometry to minimise drag. Meanwhile, numerous works in helicopter blade design have been published using similar methods, each combining a form of 3D CFD with gradient-based optimisation techniques

[126, 127, 128, 129, 130]. The gradient evaluation procedures were a choice between finite-difference and adjoint methods.

The cost associated with high-fidelity simulations and a large number of shape design variables are likely contributing factors to the limited application of this approach to turbine design [131]. It was first implemented by Economon et al. [132], who combined a RANS solver with a gradient-based optimisation algorithm informed by the adjoint method to increase the torque of the NREL Phase VI wind turbine by 4.0% after 3 design iterations. The optimisation was based on BR RANS simulations with geometry alterations allowed at 84 control points on both the pressure and suction surfaces. Dhert et al. [131] subsequently adopted this methodology, extending the degrees of freedom to include pitch, twist and aerofoil shape variables. Using their set of design variables and a larger number of design iterations, the torque coefficient of the NREL Phase VI turbine was increased by 22.4%.

To the best of the author's knowledge, all existing studies combining CFD simulations with optimisation techniques for TST rotor design utilise the CFD results to build surrogate models from which optimal geometries are obtained. The surrogate models approximate the relationship between the design variables and the objective function, so can be used to reduce the time and cost of optimisation by providing fast estimates of the objectives at new design points [118]. providing a Huang and Kanemoto [133] used a genetic algorithm to find the optimal twist distribution of the blades on the front rotor of an experimental scale counter-rotating tidal turbine from their surrogate model. The optimisation considered multiple objectives simultaneously, maximising C_P while minimising C_T, and the blades of the rear rotor were subsequently designed using the same method by [134]. Kumar et al. [118] used a deterministic optimisation algorithm to obtain their optimal design, testing multiple CFD-informed surrogate models. Blade thickness parameters, which control the hydrofoil profile, were adjusted along the span to maximising C_P, resulting in a 17.9% increase over the original design.

In this part of the thesis, the effect of modelling technique and design strategy choices on the obtained hydrodynamic shape of TST rotor blades is explored. The work first attempts to incorporate discrete blade effects in a more traditional design approach, attempting to adapt the design criteria of the RANS-BE method for implementation with AL simulations. In doing so, underlying drawbacks of the method are discovered, motivating the development of a new approach utilising numerical optimisation techniques to offer greater flexibility in the design objectives. The methodology of a multi-start deterministic approach to multi-objective optimisation is described, intended to be coupled with AL simulations. The method is then tested, utilising both BEM modelling and AL simulations to evaluate the objective function, to explore the effect of tip

corrections, rotational speed, cavitation and geometry constraints, and objective function weighting ratio on the derived hydrodynamic shape of the blades.

Chapter 8

Iterative rotor design with thrust-based design criteria

8.1 Methodology of the existing RANS-BE design routine

Extending the RANS-BE modelling approach described in Section 4.3, and given a pre-defined distribution of hydrofoil profiles, the method can be used in conjunction with a design routine to iterate the blade chord and twist distributions with the objective of maximising power.

The twist angle is chosen to maintain the design angle of attack at each blade section. The design angle of attack is defined to be the angle at which the hydrofoil section produces the maximum C_l/C_d ratio, as is typical in the analytical BEM design approach. The chord distribution is modelled through the local solidity of the annuli, as per Equation 4.14. It is this solidity which predominantly controls the turbine thrust when the rotational speed is fixed. Hence, the optimal solidity of each annulus is obtained by iterating towards a target local thrust coefficient, often chosen by considering LMADT. With the objective of maximising power, the optimal global thrust coefficient in unconstrained flow is $C_T = 8/9$, which corresponds to an axial flow induction factor of $a = 1/3$ [135, 136]. Given the definition in Equation 8.1, and noting the relationship $u_x = (1-a)U_\infty$, an optimal C_T of 8/9 is equivalent to an average local thrust coefficient (c_x) of 2.

$$c_x = \frac{\delta T}{\frac{1}{2}\rho {u_x}^2 \delta A} \tag{8.1}$$

In the global thrust coefficient definition, outlined previously in Equation 2.2, T and A refer to the total thrust and disc area respectively. Meanwhile, in the local equation, δT and δA refer to the annulus thrust and area respectively. The local thrust coefficient is generally taken to be constant across the disc, an assumption found to be reasonable by Belloni [110].

The drawback of this method is that it is analytically derived for turbines in unconstrained flow. Hence, targetting a local thrust coefficient of $c_x = 2$ is unlikely to generate a chord distribution which maximises the power production in constrained flow conditions, so the optimal c_x should be determined specifically for the intended blockage ratio. In previous studies, this was achieved by carrying out a simulation sweep across a range of candidate c_x values [32, 110]. However, this could also be derived analytically using the optimal global thrust coefficient and induction factor for blocked turbines presented by Garrett and Cummins [20].

During the RANS simulation, the design tool makes an adjustment to the rotor geometry after each timestep. The local thrust coefficient and angle of attack are measured at the beginning of each iteration, and compared against the target values. The required geometry adjustment is calculated from this error and subsequently multiplied by a small gain factor to ensure incremental changes towards the optimal solution for improved stability and convergence.

The method is effective in converging towards its design criteria; however, there are some limitations associated with the turbine representation as the actuator disc model does not capture discrete blade effects or generate tip vortices. Discrete blades experience a higher local induction factor than the azimuthal average, while the tip vortex and associated tip loss effect induce downwash and modify the surface pressure distribution. Consequently, the spanwise distributions of blade forces and relative flow velocity modelled by an actuator disc, which are important to many design processes, can differ from those of a discrete-bladed rotor.

8.2 Adaptation of design criteria to actuator line modelling

8.2.1 Design tool adaptation

This section aims to address the limitations of the existing RANS-BE design tool by implementing an equivalent design routine in the AL framework. Hence, the rotor is modelled as a set of discrete blades, while maintaining the ability to adjust the rotor geometry without the need for mesh deformation.

The revised tool has the flexibility to design specifically for a chosen blade number, capturing some discrete blade effects. Additionally, the discrete blade representation better resolves the tip vortices than the RANS-BE approach. The AL method also has the benefit of modelling the impact of the rotor on the flow directly through the blade forces. The tangential force on the flow in response to the rotor's torque is inherently captured by the model, negating the need for any assumption of the induced whirl velocity. Although it is noted that the AL method also employs the blade element method, this revised design tool is henceforth referred to as the Reynolds-averaged Navier-Stokes - actuator line (RANS-AL) design tool.

The adapted RANS-AL method uses the same design criteria as described in Section 8.1. Implementing the twist criteria requires no adaptation, however, the expression of the local thrust coefficient in Equation 8.2 is more convenient for implementation in the AL model, separating the annulus thrust force into the individual blade element contributions.

$$c_x = (C_l \cos(\phi) + C_d \sin(\phi)) \left(\frac{N_{Bl} c}{2\pi r} \right) \left(\frac{V}{u_x} \right)^2 \tag{8.2}$$

8.2.2 Comparison of the RANS-AL and RANS-BE design tool outputs

The new RANS-AL tool is tested by carrying out a design simulation with the SOUTTBP rotor as the starting blade geometry [64]. Since the SOUTTBP rotor was originally designed using the RANS-BE method, this exercise aimed to identify differences in the output of the two methods.

The SOUTTBP rotor was originally designed using the RANS-BE method without a tip correction factor applied to the actuator disc modelling. A target local thrust coefficient of $c_x = 2$ was prescribed across the majority of the span, however, this was gradually relaxed from $c_x = 2 \rightarrow 1$ in the region $r = 0.3 \rightarrow R_{\text{hub}}$ to prevent the solidity becoming excessively large at the root [67]. The raw output of the RANS-BE design tool is shown in Figure 8.1, labelled and hereafter referred to as the RANS-BE unprocessed design. Some post-processing adjustments were made to the raw output to derive the SOUTTBP rotor geometry; the outermost sections of the chord and twist distributions were linearly extrapolated, yielding what is referred to as the RANS-BE refined design.[1]

The RANS-AL design simulation used a cylindrical domain of 3.05% blockage, equivalent to the original design work, with spatial and temporal resolutions sufficient to achieve the AL criteria of $N_\epsilon \geq 2$ and $\Delta s/\Delta x \leq 1$ discussed in Chapter 5. The nacelle geometry was resolved in the mesh with the boundary flow modelled using wall functions. The Wimshurst-Willden tip correction [91] was used to account for 3D flow effects. The starting point of the RANS-AL design iteration was the RANS-BE refined design, and the design criteria matched those of the RANS-BE design simulation from which it was originally developed.

The resultant chord and twist distributions are shown in Figure 8.1, and demonstrate the key limitations of this approach. The two methods show good agreement through the mid-span, with the RANS-AL approach converging on a blade with slightly lower chord lengths and twist angles than the RANS-BE result. As the root is approached, the chord distribution from the RANS-BE method decreases smoothly as a result of the c_x relaxation, however, the RANS-AL counterpart is less smooth with an inflection point at $r/R \approx 0.2$ before a sudden reduction below $r/R = 0.14$. Despite the relaxation of the c_x target, the chord length of the RANS-AL design increases between these two radial locations. The RANS-AL derived geometry is more strongly affected by the near-nacelle flow, indicating that the discrete blade representation may be sensitive to, and lead to, a more complex root flow environment.

The key limitation of the RANS-AL approach is highlighted in the outermost most 10% of the blade span. Whereas the chord and twist both monotonically decrease throughout the mid-span,

[1] The RANS-BE unprocessed and RANS-BE refined designs were generated and kindly provided by Dr Xiaosheng Chen of the University of Oxford.

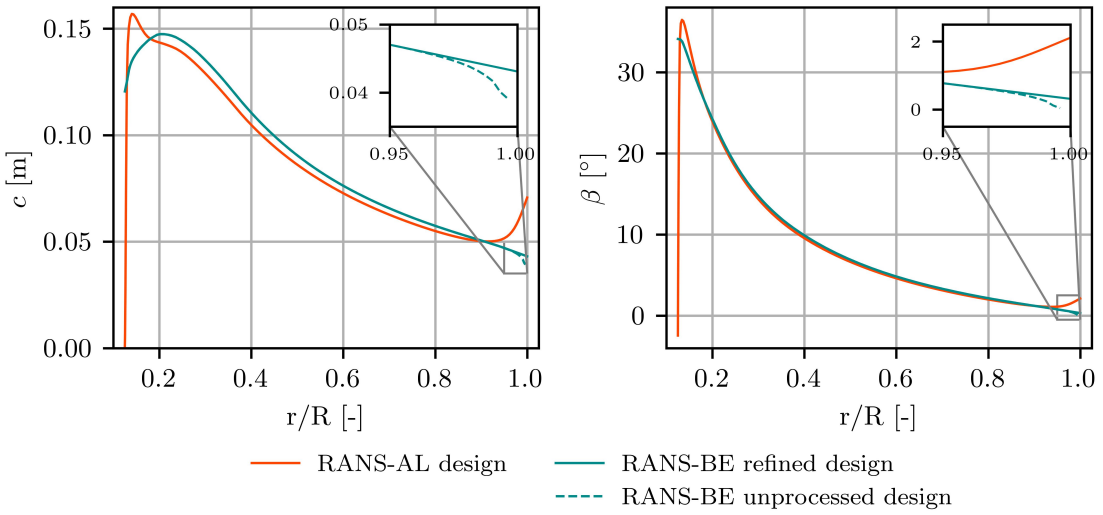


Figure 8.1: Comparing the chord and twist distributions output from the RANS-AL design tool to the input design generated from the RANS-BE tool (RANS-BE refined design). The raw output from the RANS-BE method is also plotted to highlight the refinements made near the tip in post processing. The nacelle geometry is resolved in both simulation methods, and has a normalised radius of $r/R = 0.125$.

they begin to increase towards the tip. Conventionally, loading the tip with additional chord in this way should be avoided as it in contradiction to the elliptic lift distribution predicted for minimum induced drag by lifting line theory [137]. The strength of the trailing vortices which generate induced drag are proportional to the spanwise gradient of the lift distribution, hence, since the lift force of a blade element is proportional to its chord length, sudden changes in the chord distribution should be avoided [70].

8.2.3 Comparing actuator line, RANS-BE and blade resolved simulations without design iteration

To investigate the underlying cause of this behaviour, AL simulations of the SOUTTBP rotor without geometry iteration were performed with and without the use of the Wimshurst-Willden tip loss correction. The same geometry was also evaluated using the RANS-BE method with and without the Glauert tip correction to demonstrate the rationale for opting against using the tip correction in the original design of the SOUTTBP rotor. The results are compared against those of a blade resolved RANS CFD simulation, initially performed to validate the SOUTTBP rotor design [67] and later submitted to the blind prediction exercise [66], which is taken as the ground truth for this investigation.[2] The BR simulation inherently captures the 3D flow structures at the tip, and their impact on the surface pressure distribution, without the need for tip correction, and the

[2]The blade resolved simulation data were generated and kindly provided by Dr Xiaosheng Chen of the University of Oxford.

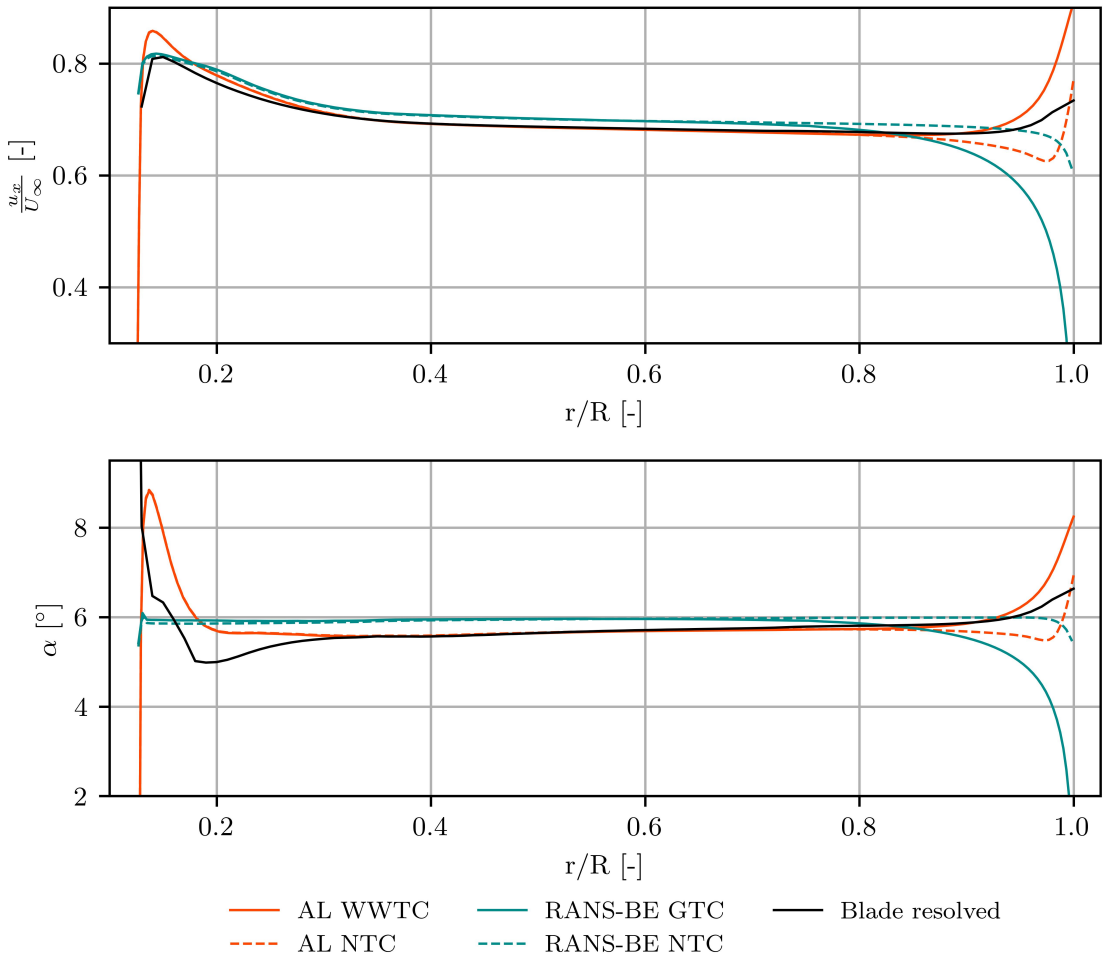


Figure 8.2: A comparison of the spanwise distribution of cycle-averaged normalised axial flow velocity (top) and angle of attack (bottom) for the AL and RANS-BE simulation methods with and without tip correction relative to the results of a blade resolved RANS simulation. Cases labelled NTC are modelled without tip correction, while those labelled WWTC and GTC use the Wimshurst-Willden and Glauert tip corrections, respectively.

flow components are extracted using the same line-average sampling method employed in the AL model. All simulations use the same inflow and operating conditions in domains of 3.05% blockage.

Figure 8.2 shows the spanwise distributions of the normalised axial flow velocity and angle of attack obtained from each of the modelling approaches. The normalised u_x distribution obtained from the BR simulation is approximately constant between $r/R = 0.3$ and $r/R = 0.95$, beyond which u_x rises gradually towards the tip. The angle of attack follows a similar distribution shape, slightly below the target of $\alpha_d = 6^\circ$ through the midspan.

The u_x and α predicted by the AL model across the midspan are in close agreement with the BR results, regardless of the tip correction. The trend in α at the tip matches the BR simulations, however, the rate of increase is not accurately reproduced. Applying the Wimshurst-Willden tip correction decreases the axial force as the tip is approached, curtailing the resistance to axial flow

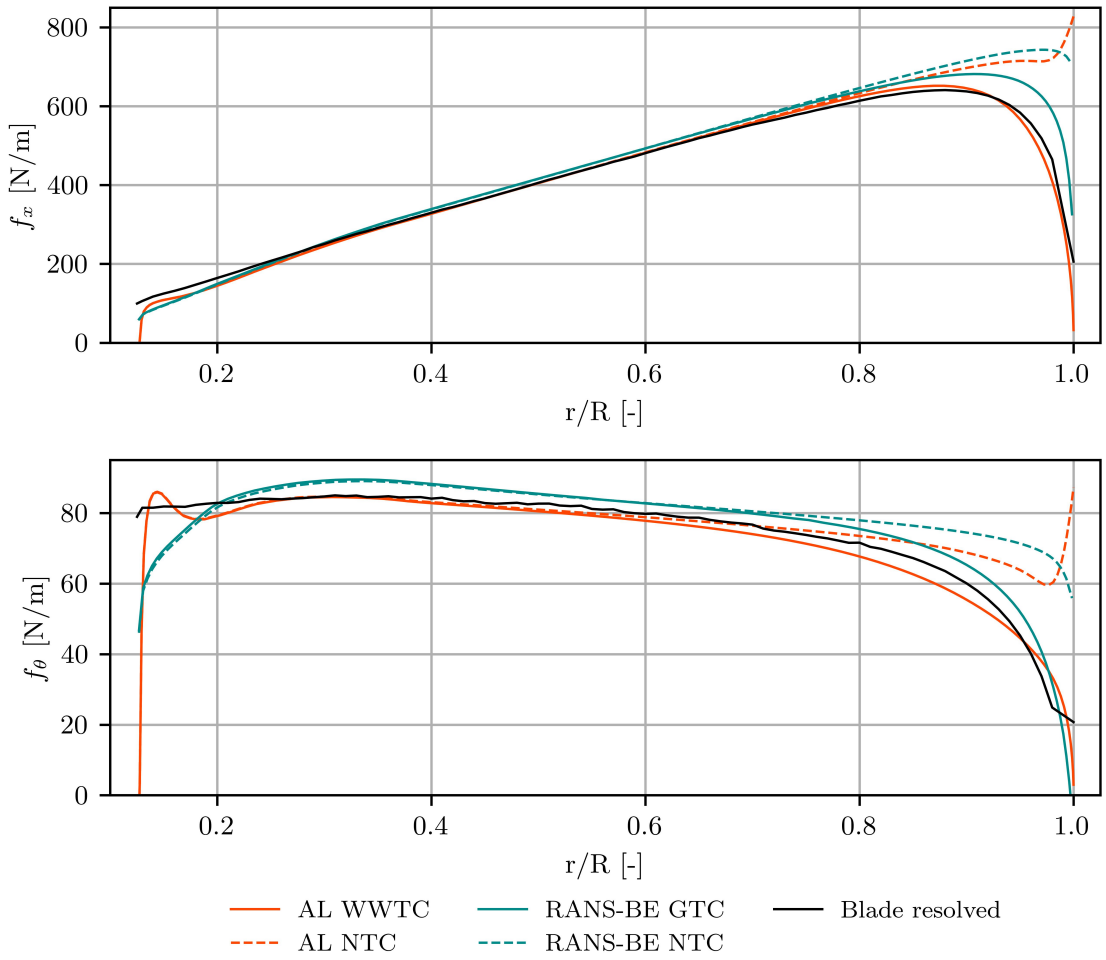


Figure 8.3: A comparison of the spanwise distribution of cycle-averaged force per unit span in the axial (top) and tangential (bottom) directions for the AL and RANS-BE simulation methods with and without tip correction relative to the results of a blade resolved RANS simulation. Cases labelled NTC are modelled without tip correction, while those labelled WWTC and GTC use the Wimshurst-Willden and Glauert tip corrections, respectively.

such that u_x increases more quickly than in the BR simulation. Without tip correction, u_x begins to gently decrease until $r/R = 0.98$, after which it increases sharply.

In both implementations of the RANS-BE method, u_x is slightly higher than the other models across the midspan, and the design angle of attack, $\alpha_d = 6^\circ$, is achieved. However, u_x decreases as the tip is approached, particularly when the Glauert tip correction is applied. The tip correction increases the axial induction factor as the tip is approached, leading to a reduction of the axial flow velocity. Consequently, both u_x and α are significantly underpredicted relative to the BR result when the Glauert tip correction is applied in the RANS-BE model. Without tip correction, the change in u_x and α are notably less substantial, showing just a slight reduction between $r/R = 0.95$ and the tip.

Figure 8.3 compares the spanwise distributions of the blade sectional forces in the axial and

tangential directions. The tip loss effect is observed in both force distributions of the BR simulation, with the forces decreasing progressively over the last 10% of the blade span. Good agreement is seen in the mid-span f_x predictions of all models, while there is greater discrepancy in f_θ. The tangential forces generated by the RANS-BE model with and without tip correction are greater than those from the BR simulation as the larger u_x and α increases the lift generated by the blade elements. The Glauert tip correction improves both force predictions, however, the rate of f_x reduction is lower than that of the BR result. The forces in the tip region are overpredicted in the uncorrected RANS-BE results, although a minor decrease is observed immediately before the tip.

The forces are also overpredicted by the AL model without tip correction, increasing significantly outboard of $r/R = 0.98$, particularly in the axial direction. Applying the Wimshurst-Willden tip correction improves the forces predicted by the AL method, and the corrected f_x is in very close agreement with the BR simulation. The reduction of f_θ in the tip region is captured, although the rate of reduction differs from the BR force distribution.

For the purposes of rotor design with the prescribed c_x and α design criteria, applying the Glauert tip correction to the RANS-BE model is less suitable as the twist distribution follows the angle of attack, which is increasingly underpredicted towards the tip ($r/R \in [0.85, 1]$). A minor reduction in u_x, f_x and α are observed without tip correction, leading to the non-linearities at the tip which were addressed to produce the RANS-BE refined design. As illustrated in Figure 8.1, implementing the RANS-AL design approach with the Wimshurst-Willden tip correction leads to increasing chord and twist distributions in the tip vicinity. Although the BR simulations also display an increase in u_x close to the tip, this behaviour is overpredicted by the AL model, leading to an increased α. With reference to Equation 8.2, the combined effects of a f_x reduction and an increase in u_x lead to a reduction in c_x, so the chord must increase towards the tip to maintain the target local thrust coefficient. Although the excessive increase in u_x affects less of the tip region when the AL model is used without tip correction, the sudden rate of change in chord close to the tip remains, which is likely to produce strong spanwise gradients in the lift distribution.

8.3 Summary

The methodology of the existing RANS-BE design approach was described, and adapted to iterate the blade chord and twist distributions within AL simulations. The resultant blade design showed rapidly increasing chord and twist distributions in the tip vicinity when the new RANS-AL design tool was implemented with the Wimshurst-Willden tip correction, prompting further analysis of the modelling techniques. The spanwise distributions of blade sectional forces and the sampled flow components predicted by AL and RANS-BE were compared against the results of a blade resolved

CFD simulation. The differences between modelling approaches, and the effect of tip corrections, were investigated through analysis of the spanwise force and flow distributions, inferring the impact on the generated rotor design.

This analysis demonstrated the inherent limitation of implementing the design criteria of the RANS-BE method in an AL-based design tool. There is uncertainty in the modelling of the tip flow velocity, and the use of a tip correction enhanced the disparity between AL and BR predictions. Nonetheless, blade resolved simulation of the SOUTTBP blade geometry also showed a non-linear increase in the axial flow velocity and angle of attack at the tip. Therefore, the c_x and α criteria are unlikely to return smooth, continuously decreasing geometry distributions in the RANS-AL design approach, even with improved flow modelling. The assumptions of the BE method necessitate the use of a tip loss model to capture the reduction of blade loads in the tip vicinity, however, their inclusion negatively impacts the modelled flow velocity which can be detrimental to the design process.

Chapter 9

Methodology of a deterministic blade design optimisation tool

[REDACTED]

This content has been withheld from the public version of the thesis.

Chapter 10

Blade design optimisation with the blade element-momentum method

[REDACTED]

This content has been withheld from the public version of the thesis.

Chapter 11

Blade design optimisation with the actuator line method

[REDACTED]

This content has been withheld from the public version of the thesis.

Part V

Conclusions

Chapter 12

Conclusions and future work

Tidal stream turbines are expected to be subject to significant loads when operating in the marine environment, some of which are inherent to the energy extraction process. This thesis explored the relationship between these two factors, seeking efficient design and operation by considering the trade-off between rotor performance and the hydrodynamic loads which are imposed on the structure. The work leveraged techniques from the fields of computational fluid dynamics and numerical optimisation to investigate the flow physics and geometric design of tidal stream turbine rotors.

12.1 Conclusions

12.1.1 Free surface proximity effects

The coupling between unsteady loading and performance was evaluated for rotors operating in close proximity to the free surface through a numerical study. The appropriateness of the commonly-used rigid lid assumption was scrutinised by comparing the results to those which model the free surface deformation. Decreasing the normalised tip clearance (s/D) from 1.188 to 0.063 increased the power and thrust coefficients by 0.13% in the rigid lid simulations, however, the deformable surface results showed no clear trend in performance. Meanwhile, decreasing the tip clearance introduced a once-per-revolution loading cycle to the root bending moments, with the range of fluctuation increasing as s/D decreased. The fluctuation range of the normalised root bending moment in the flapwise direction slightly exceeded that in the edgewise direction, with maximum recorded values of 2.8% and 2.2%, respectively, relative to their azimuthal mean. Flapwise root bending moment peaks occurred ahead of the blade top dead centre position, while edgewise root bending moment peaks slightly lagged blade top dead centre.

The physical relationships which drive this behaviour were explained, linking the blade sectional forces to the azimuthally varying flow field observed at the rotor plane. The streamwise velocity incident on the outboard sections of the blades increased as they passed the nearby boundary due to flow constriction effects. Meanwhile, the boundary diverted the radial component of the expanding flow approaching the turbine into the lateral direction, adding to the whirl velocity on the upstroke, but opposing it on the downstroke. Changes in the flapwise root bending moment

were governed by variations in the relative velocity magnitude, while the edgewise root bending moment was sensitive to both the relative velocity magnitude and the angle of attack.

These flow mechanisms, and the corresponding unsteady loads, were equally captured by the rigid lid and deformable surface models. Hence, the rigid lid approach is found to be suitable for modelling free surface proximity effects in the absence of incoming surface waves.

12.1.2 Blade design methods for tidal stream turbine rotors

[REDACTED]

This content has been withheld from the public version of the thesis.

12.2 Future work

12.2.1 Design validation and structural feasibility

A number of promising blade shapes were obtained through the design exercises in this thesis. However, their performance was only evaluated through low and medium order rotor modelling techniques. Future work should focus on validating the hydrodynamic performance of the optimised rotors through blade resolved simulations or experimental testing. Additionally, the structural feasibility of the obtained blades has not been determined, and constraints on the hydrofoil section thickness are likely to be required to design structurally realisable blades at full scale. These constraints could be computed and enforced during the design process by incorporating a reduced-order structural model. However, further development is required to allow the optimiser to adjust the thickness-to-chord ratio of the hydrofoil sections.

12.2.2 Objective functions

The aggregated objective function, consisting of the competing thrust and power metrics, enabled the trade-off between performance and loading to be investigated in the design process. However, ascertaining the exact relationship between these cost-proxy objectives and the cost of energy generated over a turbine's lifetime was not within the scope of this work. The simplicity of this cost approximation is recognised, and the use of a better-informed cost model may improve the designs, or at least aid in selection from the Pareto set. Despite this limitation, the research highlights some of the competing objectives which should be considered to produce cost-efficient rotor designs, and demonstrates the shortcomings of the mono-objective power maximisation approach.

12.2.3 Developments in rotor modelling techniques

The rotors obtained from each of the design processes, using the optimisation method and the thrust coefficient criteria, all showed geometric features which were strongly dependent on the choice of rotor modelling technique. At present, the state-of-the-art tip correction methods focus on reproducing the correct force distributions, with comparatively limited consideration given to the accuracy of the modelled flow components. Given the sensitivity of the optimal blade geometry to the flow velocity at the rotor plane, advancements in the modelling of the tip region are required to reduce the uncertainty in designs obtained using reduced-order models.

Despite this, the blade element-momentum model proved to be a useful tool for rotor optimisation exercises, while the significant time and resource requirements of the actuator line method limit its practicability. Future work should explore the use of blockage corrections for the blade element-momentum model to capture flow constriction effects in the design process without excessive computational demands.

Appendix A

Rotor geometry coefficients

[REDACTED]

This content has been withheld from the public version of the thesis.

Appendix B

Optimisation conditions

[REDACTED]

This content has been withheld from the public version of the thesis.

Bibliography

[1] Department for Energy Security and Net Zero, "UK energy in brief 2025," tech. rep., July 2025. https://www.gov.uk/government/statistics/uk-energy-in-brief-2025. Accessed online: 24-02-2026.

[2] Climate Change Committee, "The Sixth Carbon Budget: The UK's Path to Net Zero," tech. rep., December 2020. https://www.theccc.org.uk/publication/sixth-carbon-budget/. Accessed online: 24-02-2026.

[3] United Nations Framework Convention on Climate Change, "The Paris Agreement," 2015. https://unfccc.int/sites/default/files/resource/english_paris_agreement.pdf. Accessed online: 24-02-2026.

[4] Department for Energy Security and Net Zero, "UK's 2035 Nationally Determined Contribution (NDC) emissions reduction target under the Paris Agreement," Tech. Rep. E03287819 01/25, January 2025. Accessed online: 24-02-2026.

[5] National Energy System Operator, "2025 Annual Balancing Costs Report," tech. rep., June 2025. https://www.neso.energy/document/362561/download. Accessed online: 24-02-2026.

[6] K. Grattan, S. Olsson, D. R. Noble, and H. Jeffrey, "2025 UK Ocean Energy Review," tech. rep., Policy and Innovation Group, The University of Edinburgh, February 2026. https://www.policyandinnovationedinburgh.org/2025-uk-ocean-energy-review.html. Accessed online: 24-02-2026.

[7] D. Coles, A. Angeloudis, D. Greaves, G. Hastie, M. Lewis, L. MacKie, J. McNaughton, J. Miles, S. Neill, M. Piggott, D. Risch, B. Scott, C. Sparling, T. Stallard, P. Thies, S. Walker, D. White, R. Willden, and B. Williamson, *A review of the UK and British Channel Islands practical tidal stream energy resource*, vol. 477. Proceedings of the Royal Society A: Mathematical, Physical and Engineering Sciences, 2021.

[8] Department for Energy Security and Net Zero, "Electricity generation costs 2025," tech. rep., January 2026. https://www.gov.uk/government/publications/electricity-generation-costs-2025. Accessed online: 24-02-2026.

[9] Offshore Renewable Energy Catapult, "Tidal stream technology roadmap," tech. rep., March 2024. https://ore.catapult.org.uk/resource-hub/analysis-reports/tidal-stream-technology-roadmap. Accessed online: 24-02-2026.

[10] D. Coles, B. Wray, R. Stevens, S. Crawford, S. Pennock, and J. Miles, "Impacts of tidal stream power on energy system security: An Isle of Wight case study," *Applied Energy*, vol. 334, p. 120686, 2023.

[11] D. S. Coles, T. A. A. Adcock, A. Cornett, K. Haas, C. H. Jo, H. Liu, J. Miles, P. G. Novo, and J. Thiébot, "A review of global tidal stream energy resources," *Proceedings of the Royal Society A: Mathematical, Physical and Engineering Sciences*, vol. 481, no. 2328, p. 20240841, 2025.

[12] UK Marine Energy Council, "6 tidal stream projects successful in the UK's latest renewable auction," 2024. https://www.marineenergycouncil.co.uk/news/6-tidal-stream-projects-successful-in-the-uk-s-latest-renewable-auction. Accessed online: 25-02-2026.

[13] Department for Energy Security and Net Zero, "Contracts for Difference (CfD) Allocation Round 7: results," tech. rep., January 2026. https://www.gov.uk/government/publications/contracts-for-difference-cfd-allocation-round-7-results. Accessed online: 25-02-2026.

[14] T. Burton, D. Sharpe, N. Jenkins, and E. Bossanyi, *Wind energy handbook*. John Wiley and Sons, 2001.

[15] C. R. Vogel, *Theoretical limits to tidal stream energy extraction*. DPhil thesis, University of Oxford, Oxford, United Kingdom, 2014.

[16] G. A. Van Kuik, "The Lanchester-Betz-Joukowsky limit," *Wind Energy*, vol. 10, no. 3, pp. 289–291, 2007.

[17] I. G. Bryden, S. J. Couch, A. Owen, and G. Melville, "Tidal current resource assessment," *Proceedings of the Institution of Mechanical Engineers, Part A: Journal of Power and Energy*, vol. 221, pp. 125–135, 2007.

[18] G. T. Houlsby, S. Draper, and M. L. G. Oldfield, "Application of linear momentum actuator disc theory to open channel flow," Tech. Rep. OUEL 2297/08, 2008.

[19] C. R. Vogel and R. H. J. Willden, "Multi-rotor tidal stream turbine fence performance and operation," *International Journal of Marine Energy*, vol. 19, pp. 198–206, 2017.

[20] C. Garrett and P. Cummins, "The efficiency of a turbine in a tidal channel," *Journal of Fluid Mechanics*, vol. 588, pp. 243–251, 2007.

[21] J. I. Whelan, J. M. Graham, and J. Peiró, "A free-surface and blockage correction for tidal turbines," *Journal of Fluid Mechanics*, vol. 624, pp. 281–291, 2009.

[22] T. Nishino and R. H. J. Willden, "Effects of 3-D channel blockage and turbulent wake mixing on the limit of power extraction by tidal turbines," *International Journal of Heat and Fluid Flow*, vol. 37, pp. 123–135, 2012.

[23] C. R. Vogel, G. T. Houlsby, and R. H. J. Willden, "Effect of free surface deformation on the extractable power of a finite width turbine array," *Renewable Energy*, vol. 88, pp. 317–324, 2016.

[24] T. Nishino and R. H. J. Willden, "The efficiency of an array of tidal turbines partially blocking a wide channel," *Journal of Fluid Mechanics*, vol. 708, pp. 596–606, 2012.

[25] T. Nishino and R. H. J. Willden, "Two-scale dynamics of flow past a partial cross-stream array of tidal turbines," *Journal of Fluid Mechanics*, vol. 730, pp. 220–244, 2013.

[26] J. Schluntz, *Tidal turbine array modelling*. DPhil thesis, University of Oxford, Oxford, United Kingdom, 2014.

[27] S. C. Cooke, R. H. J. Willden, B. W. Byrne, T. Stallard, and A. Olczak, "Experimental investigation of thrust and power on a partial fence array of tidal turbines," in *Proceedings of the 11th European Wave and Tidal Energy Conference*, 2015.

[28] J. McNaughton, B. Cao, C. R. Vogel, and R. H. J. Willden, "Model scale testing of multi-rotor arrays designed to exploit constructive interference effects," in *Proceedings of the 13th European Wave and Tidal Energy Conference*, 2019.

[29] J. McNaughton, B. Cao, A. Nambiar, T. Davey, C. R. Vogel, and R. H. J. Willden, "Constructive interference effects for tidal turbine arrays," *Journal of Fluid Mechanics*, vol. 943, p. A38, 2022.

[30] J. McNaughton, S. Ettema, F. Zilic de Arcos, C. R. Vogel, and R. H. J. Willden, "An experimental investigation of the influence of inter-turbine spacing on the loads and performance of a co-planar tidal turbine fence," *Journal of Fluids and Structures*, vol. 118, p. 103844, 2023.

[31] J. Schluntz and R. H. J. Willden, "The effect of blockage on tidal turbine rotor design and performance," *Renewable Energy*, vol. 81, pp. 432–441, 2015.

[32] S. C. McIntosh, C. F. Fleming, and R. H. J. Willden, "Embedded RANS-BEM tidal turbine design," in *Proceedings of the 9th European Wave and Tidal Energy Conference*, 2011.

[33] A. Wimshurst and R. H. J. Willden, "Computational analysis of blockage designed tidal turbine rotors," in *Progress in Renewable Energies Offshore - Proceedings of 2nd International Conference on Renewable Energies Offshore*, 2016.

[34] A. Wimshurst and R. H. J. Willden, "Analysis of a tip correction factor for horizontal axis turbines," *Wind Energy*, vol. 20, no. 9, pp. 1515–1528, 2017.

[35] A. Wimshurst and R. H. J. Willden, "Computational observations of the tip loss mechanism experienced by horizontal axis rotors," *Wind Energy*, vol. 21, pp. 544–557, 2018.

[36] A. Wimshurst, *Tip flow corrections for horizontal axis wind and tidal turbine rotors*. DPhil thesis, University of Oxford, Oxford, United Kingdom, 2018.

[37] T. A. A. Adcock, S. Draper, R. H. J. Willden, and C. R. Vogel, "The fluid mechanics of tidal stream energy conversion," *Annual Review of Fluid Mechanics*, vol. 53, pp. 287–310, 2021.

[38] H. A. Edwards, X. Chen, C. R. Vogel, and R. H. J. Willden, "Modelling the effects of boundary proximity on a tidal rotor using the actuator line method," in *Proceedings of the 15th European Wave and Tidal Energy Conference*, 2023.

[39] I. Afgan, J. McNaughton, S. Rolfo, D. D. Apsley, T. Stallard, and P. Stansby, "Turbulent flow and loading on a tidal stream turbine by LES and RANS," *International Journal of Heat and Fluid Flow*, vol. 43, pp. 96–108, 2013.

[40] M. Slama, G. Pinon, C. El Hadi, M. Togneri, B. Gaurier, G. Germain, J.-V. Facq, J. Nuño, P. Mansilla, E. Nicolas, J. Marcille, and A. Pacheco, "Turbine design dependency to turbulence: An experimental study of three scaled tidal turbines," *Ocean Engineering*, vol. 234, p. 109035, 2021.

[41] U. Ahmed, D. D. Apsley, I. Afgan, T. Stallard, and P. K. Stansby, "Fluctuating loads on a tidal turbine due to velocity shear and turbulence: Comparison of CFD with field data," *Renewable Energy*, vol. 112, pp. 235–246, 2017.

[42] G. T. Scarlett and I. M. Viola, "Unsteady hydrodynamics of tidal turbine blades," *Renewable Energy*, vol. 146, pp. 843–855, 2020.

[43] G. T. Scarlett, B. Sellar, T. van den Bremer, and I. M. Viola, "Unsteady hydrodynamics of a full-scale tidal turbine operating in large wave conditions," *Renewable Energy*, vol. 143, pp. 199–213, 2019.

[44] P. W. Galloway, L. E. Myers, and A. S. Bahaj, "Quantifying wave and yaw effects on a scale tidal stream turbine," *Renewable Energy*, vol. 63, pp. 297–307, 2014.

[45] M. A. Holst, O. G. Dahlhaug, and C. Faudot, "CFD analysis of wave-induced loads on tidal turbine blades," *IEEE Journal of Oceanic Engineering*, vol. 40, no. 3, pp. 506–521, 2015.

[46] S. Draycott, G. Payne, J. Steynor, A. Nambiar, B. Sellar, and V. Venugopal, "An experimental investigation into non-linear wave loading on horizontal axis tidal turbines," *Journal of Fluids and Structures*, vol. 84, pp. 199–217, 2019.

[47] F. Zilic de Arcos, J. McNaughton, C. R. Vogel, and G. Pinon, "A study on a tidal rotor under the combined effects of currents and regular waves using Actuator-Line CFD simulations," in *Proceedings of the 15th European Wave and Tidal Energy Conference*, 2023.

[48] J. McNaughton, F. Zilic de Arcos, C. R. Vogel, and R. H. J. Willden, "Dynamic loading of two side-by-side tidal stream turbines in regular waves," *Journal of Fluids and Structures*, vol. 133, p. 104259, 2025.

[49] L. Zhang, S. Q. Wang, Q. H. Sheng, F. M. Jing, and Y. Ma, "The effects of surge motion of the floating platform on hydrodynamics performance of horizontal-axis tidal current turbine," *Renewable Energy*, vol. 74, pp. 796–802, 2015.

[50] M. H. B. Osman, R. H. J. Willden, and C. R. Vogel, "The effects of surge motion on floating horizontal axis tidal turbines," *International Marine Energy Journal*, vol. 3, no. 2, pp. 45–54, 2020.

[51] M. H. B. Osman, *Unsteady loading on floating horizontal axis tidal turbine*. DPhil thesis, University of Oxford, Oxford, United Kingdom, 2022.

[52] L. Wang, T. Wang, J. Wu, and G. Chen, "Multi-objective differential evolution optimization based on uniform decomposition for wind turbine blade design," *Energy*, vol. 120, pp. 346–361, 2017.

[53] J. G. Leishmann, *Principles of Helicopter Aerodynamics*, ch. Unsteady Aerodynamics, pp. 302–377. Cambridge University Press, 2006.

[54] A. S. Smyth, *Three-dimensional unsteady hydrodynamics of tidal turbines*. PhD thesis, University of Cambridge, Cambridge, United Kingdom, 2019.

[55] J. Katz and A. Plotkin, *Low-Speed Aerodynamics*, ch. Fundamentals of Inviscid, Incompressible Flow, pp. 21–43. Cambridge University Press, 2001.

[56] C. L. Sequeira and R. J. Miller, "Unsteady gust response of tidal stream turbines," in *Proceedings of the IEEE/MTS OCEANS*, 2014.

[57] I. A. Milne, A. H. Day, R. N. Sharma, and R. G. J. Flay, "Blade loads on tidal turbines in planar oscillatory flow," *Ocean Engineering*, vol. 60, pp. 163–174, 2013.

[58] I. A. Milne, A. H. Day, R. N. Sharma, and R. G. J. Flay, "Blade loading on tidal turbines for uniform unsteady flow," *Renewable Energy*, vol. 77, pp. 338–350, 2015.

[59] I. A. Milne, A. H. Day, R. N. Sharma, and R. G. J. Flay, "The characterisation of the hydrodynamic loads on tidal turbines due to turbulence," *Renewable and Sustainable Energy Reviews*, vol. 56, pp. 851–864, 2016.

[60] J. G. Leishman and T. S. Beddoes, "A semi-empirical model for dynamic stall," *Journal of the American Helicopter Society*, vol. 34, no. 3, pp. 3 – 17, 1989.

[61] A. S. M. Smyth, F. Zilic de Arcos, and A. M. Young, "Modelling unsteady hydrodynamic gust loading on tidal turbine blades," *Journal of Fluids and Structures*, vol. 137, p. 104381, 2025.

[62] A. S. M. Smyth, A. M. Young, and L. Di Mare, "The effect of 3D geometry on unsteady gust response, using a vortex lattice model," 2019.

[63] L. A. Martínez-Tossas, M. J. Churchfield, and S. Leonardi, "Large eddy simulations of the flow past wind turbines: Actuator line and disk modeling," *Wind Energy*, vol. 18, pp. 1047–1060, 2015.

[64] "Unsteady loading tidal turbine benchmarking study." `https://supergen-ore.net/projects/tidal-turbine-benchmarking`. Accessed online: 25-01-2023.

[65] S. W. Tucker Harvey, X. Chen, K. Bhavsar, T. Allsop, I. Benson, H. Mullings, T. Stallard, A. Young, J. Gilbert, C. R. Vogel, and R. H. J. Willden, "Tidal Benchmarking Project Dataset: R001_2," 2022. `https://n2t.net/ark:/29072/ora_8c96a4c001f5497eb5ca28a70c64d415`.

[66] R. H. J. Willden, X. Chen, S. W. Tucker Harvey, H. A. Edwards, C. R. Vogel, K. Bhavsar, T. Allsop, J. Gilbert, H. Mullings, M. Ghobrial, P. Ouro, D. Apsley, T. Stallard, I. Benson, A. Young, P. Schmitt, F. Zilic de Arcos, M.-A. Dufour, C. Choma Bex, G. Pinon, A. I. Evans, M. Togneri, I. Masters, L. H. da Silva Ignacio, C. A. R. Duarte, F. J. Souza, S. Gambuzza, Y. Liu, I. M. Viola, M. Rentschler, T. Gomes, G. Vaz, R. Azcueta, H. Ward, F. Salvatore, Z. Sarichloo, D. Calcagni, T. T. Tran, H. Ross, M. Oliveira, R. Puraca, and B. S. Carmo, "Tidal turbine benchmarking project: Stage I - steady flow blind predictions," in *Proceedings of the 15th European Wave and Tidal Energy Conference*, 2023.

[67] S. W. Tucker Harvey, X. Chen, D. T. Rowe, J. McNaughton, C. R. Vogel, K. Bhavsar, T. Allsop, J. Gilbert, H. Mullings, T. Stallard, I. Benson, A. Young, and R. H. J. Willden, "Tidal turbine benchmarking project: Stage I - steady flow experiments," in *Proceedings of the 15th European Wave and Tidal Energy Conference*, 2023.

[68] S. W. Tucker Harvey, X. Chen, D. Rowe, K. Bhavsar, T. Allsop, J. Gilbert, T. Stallard, C. R. Vogel, and R. H. J. Willden, "Tidal turbine benchmarking exercise: Geometry specification and environmental characterisation," in *Proceedings of the 14th European Wave and Tidal Energy Conference*, 2021.

[69] W. Froude, "On the relation between pitch, slip, and propuslive efficiency," *Institution of Naval Architects*, 1878.

[70] P. Jamieson, *Innovation in wind turbine design*. John Wiley and Sons, 2018.

[71] L. Prandtl and A. Betz, "Vier abhandlungen zur hydrodynamik und aerodynamik," tech. rep., Göttinger Kaiser-Wilhelm-Institut für Strömungsforschung, 1927.

[72] W. Z. Shen, R. Mikkelsen, J. N. Sørensen, and C. Bak, "Tip loss corrections for wind turbine computations," *Wind Energy*, vol. 8, no. 4, pp. 457–475, 2005.

[73] H. Glauert, *Aerodynamic Theory*, ch. Airplane Propellers, pp. 169–360. Julius Springer: Berlin, 1935.

[74] E. Branlard, *Wind Turbine Aerodynamics and Vorticity-Based Methods: Fundamentals and recent applications*, ch. The Blade Element Momentum (BEM) Method, pp. 181–214. Springer, 2017.

[75] A. Ning, "A simple solution method for the blade element momentum equations with guaranteed convergence," *Wind Energy*, no. 17, p. 1327–1345, 2014.

[76] R. P. Brent, "An algorithm with guaranteed convergence for finding a zero of a function," *The Computer Journal*, vol. 14, no. 4, pp. 422–425, 1971.

[77] M. L. Buhl, "A new empirical relationship between thrust coefficient and induction factor for the turbulent windmill state," Tech. Rep. NREL/TP-500-36834, NREL, August 2005.

[78] J. N. Sørensen and C. W. Kock, "A model for unsteady rotor aerodynamics," *Journal of Wind Engineering and Industrial Aerodynamics*, vol. 58, pp. 259–275, 1995.

[79] C. Masson, I. Ammara, and I. Paraschivoiu, "An aerodynamic method for the analysis of isolated horizontal-axis wind turbines," *International Journal of Rotating Machinery*, vol. 3, no. 1, pp. 21–32, 1997.

[80] A. Hallanger and I. Ø. Sand, "CFD wake modelling with a BEM wind turbine sub-model," *Modeling, Identification and Control*, vol. 34, no. 1, pp. 19–33, 2013.

[81] M. E. Harrison, W. M. J. Batten, and A. S. Bahaj, "A blade element actuator disc approach applied to tidal stream turbines," in *OCEANS 2010 MTS/IEEE SEATTLE*, pp. 1–8, 2010.

[82] R. Malki, A. J. Williams, T. N. Croft, M. Togneri, and I. Masters, "A coupled blade element momentum – Computational fluid dynamics model for evaluating tidal stream turbine performance," *Applied Mathematical Modelling Journal*, vol. 37, pp. 3006–3020, 2013.

[83] J. N. Sørensen and W. Z. Shen, "Numerical modeling of wind turbine wakes," *Journal of Fluids Engineering*, vol. 124, pp. 393–399, 2002.

[84] S. Kang, X. Yang, and F. Sotiropoulos, "On the onset of wake meandering for an axial flow turbine in a turbulent open channel flow," *Journal of Fluid Mechanics*, vol. 744, pp. 376–403, 2014.

[85] D. D. Apsley, T. Stallard, and P. K. Stansby, "Actuator-line CFD modelling of tidal-stream turbines in arrays," *Journal of Ocean Engineering and Marine Energy*, vol. 4, pp. 259–271, 2018.

[86] T. Stallard, H. Mullings, S. Draycott, and P. Ouro, "Large-eddy simulations of interaction between surface waves and a tidal turbine wake in a turbulent channel," in *Proceedings of the 15th European Wave and Tidal Energy Conference*, 2023.

[87] H. Mullings, L. Amos, C. Miller, P. Ouro, and T. Stallard, "Efficient prediction of tidal turbine fatigue loading using turbulent onset flow from Large Eddy Simulations," *Journal of Ocean Engineering and Marine Energy*, vol. 10, pp. 537–554, 2024.

[88] B. Msutwana, X. Chen, and R. H. J. Willden, "Effects of synthetic sheared flow on a utility-scale rotor in an open channel," in *Proceedings of the 16th European Wave and Tidal Energy Conference*, 2025.

[89] C. Li, Y. Zhang, Y. Zheng, Y. Qian, E. Fernandez-Rodriguez, and E. Benini, "Research on the effect of yawing motion on tidal turbine performance based on actuator-line method," *Ocean Engineering*, vol. 279, p. 114345, 2023.

[90] C. Li, Y. Zhang, W. Zang, C. Feng, Y. Zheng, and E. Fernandez-Rodriguez, "Analysis on heave motion of floating tidal stream turbine using actuator line method," in *Innovations in Renewable Energies Offshore - Proceedings of 6th International Conference on Renewable Energies Offshore*, 2024.

[91] A. Wimshurst and R. H. J. Willden, "Spanwise flow corrections for tidal turbines," *International Marine Energy Journal*, vol. 1, no. 2, pp. 111–121, 2018.

[92] N. Troldborg, *Actuator line modeling of wind turbine wakes*. PhD thesis, Technical University of Denmark, Kongens Lyngby, Denmark, 2008.

[93] M. Shives and C. Crawford, "Mesh and load distribution requirements for actuator line CFD simulations," *Wind Energy*, no. 16, pp. 1183–1196, 2013.

[94] M. Zormpa, F. Zilic de Arcos, X. Chen, C. R. Vogel, and R. H. J. Willden, "The effect of flow sampling on the robustness of the actuator line method," *Wind Energy*, vol. 28, p. e2965, 2025.

[95] J. Schluntz and R. H. J. Willden, "An actuator line method with novel blade flow field coupling based on potential flow equivalence," *Wind Energy*, vol. 18, pp. 1469–1485, 2015.

[96] E. Jost, L. Klein, H. Leipprand, T. Lutz, and E. Krämer, "Extracting the angle of attack on rotor blades from CFD simulations," *Wind Energy*, vol. 21, pp. 807–822, 2018.

[97] F. Zilic de Arcos, C. R. Vogel, and R. H. J. Willden, "Extracting angles of attack from blade-resolved rotor CFD simulations," *Wind Energy*, vol. 23, pp. 1868–1885, 2020.

[98] M. J. Churchfield, S. Schreck, L. A. Martínez-Tossas, C. Meneveau, and P. R. Spalart, "An advanced actuator line method for wind energy applications and beyond," in *35th Wind Energy Symposium*, 2017.

[99] M. Zormpa, C. R. Vogel, and R. H. J. Willden, "Support structure modelling in actuator line method large eddy simulations of wind turbine wakes," *Wind Energy*, vol. 29, no. 1, 2026.

[100] B. Keogh, *Performance quantification of marine current energy converters in constrained flow fields*. PhD thesis, University of Southampton, Southampton, United Kingdom, 2016.

[101] E. Mascrier, F. Zilic de Arcos, and G. Pinon, "Effects of non-isotropic blockage on a tidal turbine modeled with the Actuator-Line method," in *Proceedings of the 15th European Wave and Tidal Energy Conference*, 2023.

[102] A. S. Bahaj, A. F. Molland, J. R. Chaplin, and W. M. Batten, "Power and thrust measurements of marine current turbines under various hydrodynamic flow conditions in a cavitation tunnel and a towing tank," *Renewable Energy*, vol. 32, no. 3, pp. 407–426, 2007.

[103] H. Wang, X. Wang, X. Gao, Y. Cen, F. Yu, and X. Liu, "Effect of immersion depth on hydrodynamic characteristics of a horizontal-axis tidal turbine," *Energy Conversion and Management*, vol. 348, p. 120590, 2026.

[104] N. Kolekar, A. Vinod, and A. Banerjee, "On blockage effects for a tidal turbine in free surface proximity," *Energies*, vol. 12, no. 17, 2019.

[105] N. Kolekar and A. Banerjee, "Performance characterization and placement of a marine hydrokinetic turbine in a tidal channel under boundary proximity and blockage effects," *Applied Energy*, vol. 148, pp. 121–133, 2015.

[106] S. Ettema, *Novel turbine fence optimisation using lateral flow constraint.* DPhil thesis, University of Oxford, Oxford, United Kingdom, 2022.

[107] C. G. Anderson, *Wind Turbines: Theory and Practice.* Cambridge University Press, 2024.

[108] L. Myers and A. S. Bahaj, "Power output performance characteristics of a horizontal axis marine current turbine," *Renewable Energy*, vol. 31, pp. 197–208, 2006.

[109] C. Faudot and O. G. Dahlhaug, "Tidal turbine blades: Design and dynamic loads estimation using CFD and blade element momentum theory," in *Proceedings of the International Conference on Offshore Mechanics and Arctic Engineering*, 2011.

[110] C. Belloni, *Hydrodynamics of ducted and open-centre tidal turbines.* DPhil thesis, University of Oxford, Oxford, United Kingdom, 2013.

[111] B. Cao, R. H. J. Willden, and C. R. Vogel, "Effects of blockage and freestream turbulence intensity on tidal rotor design and performance," in *3rd International Conference on Renewable Energies Offshore*, 2018.

[112] P. Fuglsang and H. A. Madsen, "Optimization method for wind turbine rotors," *Journal of Wind Engineering and Industrial Aerodynamics*, vol. 80, pp. 191–206, 1999.

[113] G. Kenway and J. R. R. A. Martins, "Aerostructural shape optimization of wind turbine blades considering site-specific winds," in *Proceedings of the 12th AIAA/ISSMO Multidisciplinary Analysis and Optimization Conference*, 2008.

[114] W. Xudong, W. Z. Shen, W. J. Zhu, J. N. Sørensen, and C. Jin, "Shape optimization of wind turbine blades," *Wind Energy*, vol. 12, pp. 781–803, 2009.

[115] E. Benini and A. Toffolo, "Optimal design of horizontal-axis wind turbines using blade-element theory and evolutionary computation," *Journal of Solar Energy Engineering*, vol. 124, no. 4, pp. 357–363, 2002.

[116] G. R. Fischer, T. Kipouros, and A. M. Savill, "Multi-objective shape optimisation for horizontal-axis wind turbine blades," in *53rd AIAA/ASME/ASCE/AHS/ASC Structures, Structural Dynamics and Materials Conference*, 2012.

[117] M. S. Selig and V. L. Coverstone-Carroll, "Application of a genetic algorithm to wind turbine design," *Journal of Energy Resources Technology*, vol. 118, no. 1, pp. 22–28, 1996.

[118] P. M. Kumar, J. Seo, W. Seok, S. H. Rhee, and A. Samad, "Multi-fidelity optimization of blade thickness parameters for a horizontal axis tidal stream turbine," *Renewable Energy*, vol. 135, pp. 277–287, 2019.

[119] D. Sale, J. Jonkman, and W. Musial, "Hydrodynamic optimization method and design code for stall-regulated hydrokinetic turbine rotors," in *ASME 28th International Conference on Ocean, Offshore, and Arctic Engineering*, 2009.

[120] G. S. Bir, M. J. Lawson, and Y. Li, "Structural design of a horizontal-axis tidal current turbine composite blade," in *Proceedings of the International Conference on Offshore Mechanics and Arctic Engineering*, 2011.

[121] M. J. Lawson, Y. Li, and D. C. Sale, "Development and verification of a computational fluid dynamics model of a horizontal-axis tidal current turbine," in *Proceedings of the International Conference on Offshore Mechanics and Arctic Engineering*, 2011.

[122] N. Kolekar, S. S. Mukherji, and A. Banerjee, "Numerical modeling and optimization of hydrokinetic turbine," in *Proceedings of the ASME 2011 5th International Conference on Energy Sustainability*, pp. 1211–1218, 2011.

[123] M. Tahani, N. Babayan, F. R. Astaraei, and A. Moghadam, "Multi objective optimization of horizontal axis tidal current turbines, using Meta heuristics algorithms," *Energy Conversion and Management*, vol. 103, pp. 487–498, 2015.

[124] F.-w. Zhu, L. Ding, B. Huang, M. Bao, and J.-T. Liu, "Blade design and optimization of a horizontal axis tidal turbine," *Ocean Engineering*, vol. 195, p. 106652, 2020.

[125] Z. Lyu, G. K. W. Kenway, and J. R. R. A. Martins, "Aerodynamic shape optimization investigations of the common research model wing benchmark," *AIAA Journal*, vol. 53, no. 4, pp. 968–985, 2015.

[126] A. Le Pape and P. Beaumier, "Numerical optimization of helicopter rotor aerodynamic performance in hover," *Aerospace Science and Technology*, vol. 9, pp. 191–201, 2005.

[127] E. J. Nielsen, E. M. Lee-Rausch, and W. T. Jones, "Adjoint-based design of rotors in a noninertial reference frame," *Journal of Aircraft*, vol. 47, no. 2, pp. 638–646, 2010.

[128] A. Dumont, A. Le Pape, J. Peter, and S. Huberson, "Aerodynamic shape optimization of hovering rotors using a discrete adjoint of the Reynolds-Averaged Navier-Stokes equations," *Journal of the American Helicopter Society*, vol. 56, pp. 1–11, 2011.

[129] S. Choi, K. Lee, M. M. Potsdam, and J. J. Alonso, "Helicopter rotor design using a time-spectral and adjoint-based method," *Journal of Aircraft*, vol. 51, no. 2, pp. 412–423, 2014.

[130] C. B. Allen and T. C. S. Rendall, "CFD-based optimization of hovering rotors using radial basis functions for shape parameterization and mesh deformation," *Optimization and Engineering*, vol. 14, no. 1, pp. 97–118, 2013.

[131] T. Dhert, T. Ashuri, and J. R. R. A. Martins, "Aerodynamic shape optimization of wind turbine blades using a Reynolds-averaged Navier-Stokes model and an adjoint method," *Wind Energy*, vol. 20, pp. 909–926, 2017.

[132] T. D. Economon, F. Palacios, and J. J. Alonso, "A viscous continuous adjoint approach for the design of rotating engineering applications," in *Proceedings of the 21st AIAA Computational Fluid Dynamics Conference*, 2013.

[133] B. Huang and T. Kanemoto, "Multi-objective numerical optimization of the front blade pitch angle distribution in a counter-rotating type horizontal-axis tidal turbine," *Renewable Energy*, vol. 81, pp. 837–844, 2015.

[134] B. Huang, Y. Usui, K. Takaki, and T. Kanemoto, "Optimization of blade setting angles of a counter-rotating type horizontal-axis tidal turbine using response surface methodology and experimental validation," *International Journal of Energy Research*, vol. 40, pp. 610–617, 2016.

[135] F. W. Lanchester, "A contribution to the theory of propulsion and the screw propeller," in *Transactions of the Institution of Naval Architects*, vol. 57, pp. 98–116, 1915.

[136] A. Betz, "Das maximum der theoretisch möglichen ausnützung des windes durch windmotoren," *Zeitschrift für das gesamte Turbinenwesen*, vol. 26, pp. 307–309, 1920.

[137] J. Katz and A. Plotkin, *Low-Speed Aerodynamics*, ch. Three-Dimensional Small-Disturbance Solutions, p. 167–205. Cambridge University Press, 2001.